NAVAL POSTGRADUATE SCHOOL

MONTEREY, CALIFORNIA

THESIS

STALL CHARACTERISTIC PREDICTION IN A SINGLE PASSAGE OF A TRANSONIC AXIAL COMPRESSOR ROTOR

by

Benjamin L. Meinster

June 2021

Thesis Advisor:	Walter Smith
Co-Advisor:	Garth V. Hobson
Second Reader:	Anthony J. Gannon

THIS PAGE INTENTIONALLY LEFT BLANK

REPORT DOCUMENTATION PAGE			*Form Approved OMB No. 0704-0188*

1. AGENCY USE ONLY *(Leave blank)*	**2. REPORT DATE** June 2021	**3. REPORT TYPE AND DATES COVERED** Master's thesis

4. TITLE AND SUBTITLE
STALL CHARACTERISTIC PREDICTION IN A SINGLE PASSAGE OF A TRANSONIC AXIAL COMPRESSOR ROTOR

5. FUNDING NUMBERS

6. AUTHOR(S) Benjamin L. Meinster

7. PERFORMING ORGANIZATION NAME(S) AND ADDRESS(ES)
Naval Postgraduate School
Monterey, CA 93943-5000

8. PERFORMING ORGANIZATION REPORT NUMBER

9. SPONSORING / MONITORING AGENCY NAME(S) AND ADDRESS(ES)
N/A

10. SPONSORING / MONITORING AGENCY REPORT NUMBER

11. SUPPLEMENTARY NOTES The views expressed in this thesis are those of the author and do not reflect the official policy or position of the Department of Defense or the U.S. Government.

12a. DISTRIBUTION / AVAILABILITY STATEMENT
Approved for public release. Distribution is unlimited.

12b. DISTRIBUTION CODE
A

13. ABSTRACT (maximum 200 words)

This study expands on previous work related to computational fluid dynamics (CFD) modeling of a single blade passage of the NPS Military Fan (NPSMF) with a particular focus on improving numerical predictions of rotor performance and resolving flow features near stall. A previous CFD model of the NPSMF is examined through a mesh sensitivity study in order to better resolve flow through the device in the near-stall region. Additionally, the existing gas path geometry is reconstructed to provide a higher-quality periodic boundary for simulations of a single blade passage and to introduce a method for rapid implementation of casing treatments in support of concurrent and future studies to improve the NPSMF's stall margin. The improved mesh and gas path geometry are then simulated for three tip-clearance cases (zero, narrow, and wide) using ANSYS CFX and compared to previous numerical predictions and experimental data from the narrow tip-clearance case to highlight improvements to the CFD model. The updated CFD model under-predicts the stall point compared to the experimental data but shows significant improvement over previous work. Flow visualizations from the three tip-clearance cases are compared to each other to highlight tip-clearance effects within the NPSMF flow field, and a stalled case from the wide tip-gap is used to illustrate the tip-blockage mechanism responsible for stall.

14. SUBJECT TERMS CFD, computational fluid dynamics, compressor, transonic, stall, tip vortex, tip clearance	**15. NUMBER OF PAGES** 117
	16. PRICE CODE

17. SECURITY CLASSIFICATION OF REPORT	**18. SECURITY CLASSIFICATION OF THIS PAGE**	**19. SECURITY CLASSIFICATION OF ABSTRACT**	**20. LIMITATION OF ABSTRACT**
Unclassified	Unclassified	Unclassified	UU

NSN 7540-01-280-5500

Standard Form 298 (Rev. 2-89)
Prescribed by ANSI Std. 239-18

THIS PAGE INTENTIONALLY LEFT BLANK

Approved for public release. Distribution is unlimited.

STALL CHARACTERISTIC PREDICTION IN A SINGLE PASSAGE OF A TRANSONIC AXIAL COMPRESSOR ROTOR

Benjamin L. Meinster
Ensign, United States Navy
BSME, United States Naval Academy, 2020

Submitted in partial fulfillment of the
requirements for the degree of

MASTER OF SCIENCE IN ENGINEERING SCIENCE
(AEROSPACE ENGINEERING)

from the

NAVAL POSTGRADUATE SCHOOL
June 2021

Approved by: Walter Smith
Advisor

Garth V. Hobson
Co-Advisor

Anthony J. Gannon
Second Reader

Garth V. Hobson
Chair, Department of Mechanical and Aerospace Engineering

THIS PAGE INTENTIONALLY LEFT BLANK

ABSTRACT

This study expands on previous work related to computational fluid dynamics (CFD) modeling of a single blade passage of the NPS Military Fan (NPSMF) with a particular focus on improving numerical predictions of rotor performance and resolving flow features near stall. A previous CFD model of the NPSMF is examined through a mesh sensitivity study in order to better resolve flow through the device in the near-stall region. Additionally, the existing gas path geometry is reconstructed to provide a higher-quality periodic boundary for simulations of a single blade passage and to introduce a method for rapid implementation of casing treatments in support of concurrent and future studies to improve the NPSMF's stall margin. The improved mesh and gas path geometry are then simulated for three tip-clearance cases (zero, narrow, and wide) using ANSYS CFX and compared to previous numerical predictions and experimental data from the narrow tip-clearance case to highlight improvements to the CFD model. The updated CFD model under-predicts the stall point compared to the experimental data but shows significant improvement over previous work. Flow visualizations from the three tip-clearance cases are compared to each other to highlight tip-clearance effects within the NPSMF flow field, and a stalled case from the wide tip-gap is used to illustrate the tip-blockage mechanism responsible for stall.

THIS PAGE INTENTIONALLY LEFT BLANK

TABLE OF CONTENTS

LIST OF FIGURES

LIST OF TABLES

THIS PAGE INTENTIONALLY LEFT BLANK

LIST OF ACRONYMS AND ABBREVIATIONS

Blisk	Bladed Disk
CFD	Computational Fluid Dynamics
FSI	Fluid-Structure Interaction
LES	Large Eddy Simulation
NPSMF	NPS Military Fan
RMS	Root-Mean-Squared
SST	Shear Stress Transport
TCR	Transonic Compressor Rig
TG	Tip-Gap
TPL	Turbopropulsion Lab
URANS	Unsteady Reynolds-Averaged Naiver-Stokes

THIS PAGE INTENTIONALLY LEFT BLANK

I. INTRODUCTION

A. MOTIVATION

The Naval Postgraduate School Military Fan (NPSMF) is a transonic axial compressor rotor used for research at the Naval Postgraduate School's Turbopropulsion laboratory. Research using the NPSMF consists of both experimentation and computational fluid dynamics (CFD) studies. Experiments using the NPSMF are costly, so CFD studies are used where possible to minimize the number of experiments required. Previous CFD studies have focused on characterizing the compressor's performance across its operating envelope and increasing the fidelity of CFD models to match experimental performance under normal operating conditions. This study aims to continue on the previous work by modelling flow through the NPSMF at the onset of stall and identifying the modes by which the fan stalls.

Previous CFD studies of the NPSMF have developed models with sufficient fidelity to identify flow features within the fan. However, the previous work has yet to simulate flow through the fan in a stalled condition and to examine the flow features which characterize the stall. Understanding how the fan stalls is crucial to developing treatments which will increase the stall margin. Treatments to improve the stall margin involve modifying the casing which shrouds the compressor rotor and are the subject of a related study.

B. PREVIOUS WORK

1. External Literature Review

Improvements to rotating turbomachinery has been directed towards extracting more power from smaller devices for several decades. In practice, this improvement is achieved by maximizing the aerodynamic loading placed on each blade. Currently, the highest-performing axial compressors operate with supersonic relative inlet Mach numbers at the blade tip, making them transonic devices. Operating in the transonic regime introduces a host of complex flow phenomena which makes designing and analyzing these machines challenging, especially as the machine approaches and enters stall. However,

much has been done in recent years to understand the complex flow physics which characterize stall in transonic axial compressors. Recent work in this field includes computational and experimental studies to predict performance, examine the flow field across speed lines, and study potential casing treatments for stall margin improvement. The particular subjects of these works trend towards three, roughly chronological, categories:

- Studies which examine flow through test cases (such as NASA Rotor-37) to study specific flow features general to transonic axial compressors,
- Studies which implement new computational techniques for modeling flow through transonic axial compressors test cases (such as NASA rotor-37) with validation against experimental data, and
- Studies which evaluate casing treatments or other techniques to improve a compressor's stall margin.

One important commonality shared by many of the recent works regarding transonic axial compressors is the use of NASA rotor 37 for computational studies. NASA rotor 37 is a single-stage transonic axial compressor designed at the NASA Lewis Research Center to experimentally study the performance of transonic axial compressors [1]. Experimental data for the NASA rotor 37 test case is widely available, and many studies use it to validate new computational approaches to modeling flow through transonic axial compressors.

The first class of relevant works includes those which examine particular flow features present in transonic axial compressors. One important such work (though not an entirely recent work) is that of Hofmann and Ballmann [2], who in 2002 performed a steady-state computational study on a single passage of NASA rotor 37 geometry to visualize the formation of tip-leakage vortices and characterize their effects on rotor performance. A similar study by Hah, Rabe, and Wadia examined tip-leakage vortices in a forward-swept transonic axial compressor geometry, and characterized the development of these vortices as the rotor approaches stall [3]. Both of these studies point to passage blockage caused by excessive growth of the tip-leakage vortices as the primary mechanism

for a tip-blockage stalling rotor. One especially important driver of this tip-leakage vortex growth is the vortex-passage shock interaction which causes rapid deceleration of the tip [2]. Another such area of research is the study of heat transfer between the fluid and casing downstream of the rotor. Current CFD models (including the one presented in this study) treat the casing as an adiabatic wall, whereas Turner et al. have shown experimentally that heat transfer to the casing in the downstream ducting of a rotor-only rig can occur with a magnitude equal to 0.64% the overall work of the compressor [4]. In fact, one study which stands out for nearly resolving the normalized temperature near the casing is that of Ameri, whose NASA Glenn-HT code incorporated heat transfer into the casing [5]. Studies in this category have happened less frequently in recent years than studies in the following two categories.

The second category of recent studies seek to advance the techniques used to computationally model flow through transonic axial compressors, with validation against experimental data. The current state-of-the-art in this regard involves various combinations of large eddy simulation (LES) modelling, transient modelling, and multi-passage simulations. The most current models utilize unsteady Reynolds-Averaged Naiver-Stokes (URANS)/LES models, such as that utilized by Kelly et al. to examine the Notre Dame academic compressor stage [6]. However, the computational expense of transient and LES simulations still limits many studies to steady-state simulations utilizing turbulence models such as Wilcox k-omega and Reynolds' Shear-Stress Transport (SST). For example, Ameri validated simulations of NASA rotor 37 using the Glenn-HT code with single-passage, steady-state simulations with k-omega turbulence, and achieved good agreement with experimental data [5]. More recently, a 2019 study by Nel examined flow through two test cases (Darmstadt R-1/S-1 and NASA rotor 37), comparing a variety of turbulence models with and without laminar-to-turbulent boundary layer transition, and comparing steady-state and transient simulations for single and multi-stage compressors [7]. Results from this study indicated that steady-state modelling is appropriate for single-stage simulations, but breaks down when multiple stages are implemented. Additionally, Nel showed that utilizing a boundary layer turbulence transition model (specifically, the gamma-theta

model utilized in ANSYS CFX) adds significant fidelity to simulations for both test cases [7].

Finally, the most recent works regarding transonic axial compressors have been directed towards simulating the effects of various casing treatments to improve stall margin. The casing treatment applied to a given compressor should be designed based on the existing stall characteristics, which in turn should come from an existing computational model. However, current casing treatment designs are generally incorporations of either circumferential grooves or axial slots. Implementations of circumferential and axial treatments have recently been achieved by Kuang et al. [8] and Mustaffa and Kanjirakkad [9], respectively. Kuang et al. implemented a series of axial slot casing treatments onto NASA rotor 67 (another test case rotor, found to stall by tip blockage) to examine the flow mechanisms which improve rotor performance [8]. The results from this study indicated that the axial slots successfully delay the blockage responsible for stall, and that their effectiveness is highly dependent on their placement along the axial direction. More recently Mustaffa and Kanjirakkad implemented circumferential casing grooves at various axial locations along a steady-state RANS NASA rotor 37 model, showing that this treatment also improves stall margin without sacrificing compressor efficiency [9]. Other work, such as that by Zhu and Yang [10] combines the circumferential and axial treatment approaches into a coupled casing treatment, and shows significant potential for stall margin improvement given future optimization studies.

2. Internal Literature Review

The NPSMF project is an ongoing effort which has significantly improved modeling fidelity of the facility's transonic axial rotor. Earlier works on the NPSMF which are relevant to this study include those of McNab [11], DeSousa [12], Londono [13], and Descovich [14]. McNab conducted the first comparison of experimental data to CFD predictions for steady-state operation of the NPSMF at various speeds, with particular attention paid to the stall margin. DeSousa developed advanced casing treatments and improved on CFD modelling of the rotor to reflect changes to the TCR made since McNab's study. Londono conducted an experimental analysis of non-periodic flow

disturbances in the tip-gap region, which examined the mechanisms for stall in the NPSMF and experimentally identified tip-leakage vortices in the fan. Recommendations from these studies included the application of multiphase flow and fluid-structure interaction (FSI) to future CFD models, as well as further study of the effect of tip-gap clearance and advanced casing treatments.

The most recent effort to improve CFD modelling of the NPSMF includes the work of Thornton [15], who addressed some previous recommendations by utilizing a two-way FSI model and simulating rotor operations with tip-gap clearances representative of those found in the real rotor. Thornton's study produced CFD predictions of rotor performance which were closer to experimental data than those obtained in previous studies, and recommended that future work find ways to improve mesh quality in the gas path.

C. CURRENT STUDY

The NPSMF geometry is significantly more complex than the test case geometries commonly used in the existing body of work. As such, modelling flow through the NPSMF poses some challenges which previous studies have not addressed. The complex geometry lends itself to an equally complex flow field, whose features have yet to be studied in sufficient detail by previous NPSMF works. This shortcoming stems primarily from difficulties in generating a uniform structured grid around the blade surface, namely due to its highly three-dimensional contours. Results from previous NPSMF works have also been affected by a non-conformal periodic boundary surface, which may distort important flow features, especially in the near-stall region. Whereas the previous NPSMF work has accepted the limitations on flow modelling fidelity in order to pursue other lines of inquiry, this study addresses the important shortcomings of previous work to create a foundational NPSMF model which will be the basis of future work.

The current study continues from the previous work by refining the existing NPSMF model for more accurate predictions of rotor performance near stall. This goal was accomplished by first conducting a mesh sensitivity study on the previous CFD model to determine where improvements to the mesh would result in the greatest improvement; then by improving on the gas path geometries from those developed by McNab [11], and finally

by simulating operation of the rotor using the improved mesh and geometry to obtain performance predictions for the rotor along the 90% speed line.

The mesh sensitivity study improved on the previous work by systematically changing mesh parameters to determine their respective effects on the quality of performance predictions. The gas path redesign was accomplished using a high-resolution model of the NPSMF rotor in SolidWorks, and focused on improving the quality of the periodic boundary geometry developed in the previous work. Additionally, improvements to the gas path geometry deliberately included a framework for rapid implementation of future advanced casing treatments in SolidWorks. This change is intended to hasten the development of new casing treatments by allowing for quick integration with the existing CFD model.

II. EXPERIMENTAL FACILITY AND PROCEDURES

The numerical performance predictions obtained in this study were evaluated for fidelity by comparison to experimental data. All of the CFD predictions in this study were obtained by simulating operation of the NPSMF rotor at 90% of its design speed, 27,000 RPM (design speed 30,000 RPM). Experimentation is limited to 90% of the fan's design speed due to the high power required to drive the NPSMF. Discussion of the experimental facility and procedures found in this study is necessarily limited, as the relevant data are used only for comparison to the numerical predictions which are the subject of the current study. A complete description of the NPSMF rotor, the transonic compressor rig (TCR), and the procedures used to collect and reduce the experimental data collected therefrom can be found in the works of McNab [11] and DeSousa [12], whose studies were experimental in nature.

A. THE TRANSONIC COMPRESSOR RIG

The TCR is the test bed within which the NPSMF is mounted for experimentation. A profile view of the TCR is provided in Figure 1.

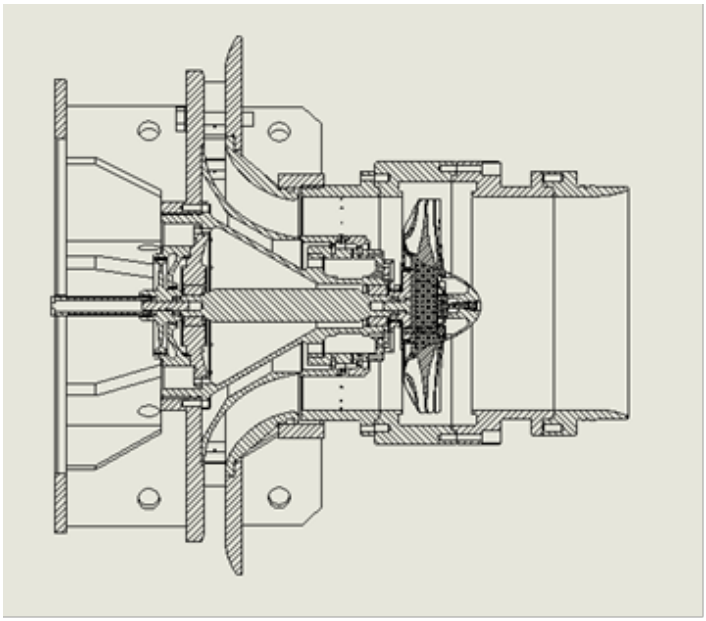

Figure 1. Profile view of the TCR. Source: [12].

The TCR utilizes a compressed air-driven turbine to drive the test article (in this study, the NPSMF). Upstream of the test article are a bell-mouth inlet, a throttle, and a flow-straightening plenum. Downstream of the test article are axial then radial discharge ducts which send compressed air from the test article and from the drive turbine to the atmosphere. Instrumentation is mounted upstream and downstream of the test article to measure flow conditions including static and total pressure and temperature and mass flow rate. The TCR is operated by driving the NPSMF at a constant speed and throttling the inlet. This method of operation requires less power than increasing the static back pressure. The accuracy of the mass flow nozzle is particularly relevant to the present study, and was addressed by Thornton [15]. Further improvements to experimental measurements of mass flow are the subject of concurrent studies.

Two configuration features of the TCR which are relevant to the present study are the half-stage configuration and the rotor casing. Both of these features are depicted in Figure 1. The half-stage configuration refers to the use of only the rotor (the NPSMF) without a corresponding stator. While implementation of a complete stage will be accomplished in future work, the current study only desires to examine the rotor's performance. Additionally, the rotor casing configuration is of particular importance to this study. Though not shown in Figure 1, the TCR configuration used in this study included a smooth, traditionally-machined casing which can be interchanged to study the effects of tip-gap clearance and casing treatments on rotor performance. Two tip-gaps are considered in the present study. One casing implemented a smaller cold tip clearance measuring 0.381 mm (0.015 in, 0.42% mean blade height), which decreased to 0.165 mm (0.007 in) at the rear of the rotor during operation. Another casing implemented a larger cold tip clearance of 1.27 mm (0.050 in, 1.41% mean blade height). Additional details regarding characteristics of the rotor casing can be found in DeSousa [12].

B. THE NPS MILITARY FAN

This study examines in detail the performance characteristics of the NPS Military Fan (NPSMF). Figure 2 provides a front view of the NPSMF. A prominent feature of the

NPSMF's advanced geometry is the forward sweep of its blades, which can be observed in Figure 2.

Figure 2. Front view of the NPS Military Fan. Source: [11].

The NPSMF is a 20-blade transonic axial compressor rotor constructed from titanium alloy as a single-piece blisk (bladed disk). It has been used at the TPL for numerous studies to examine the performance of transonic axial compressors with respect to operating conditions and requirements unique to naval applications. Chief among these applications in recent studies have been characterizing and preventing steam-induced compressor stall and improving stall margin through advanced casing treatments. A selection of design characteristics of the NPSMF as obtained by McNab [11] are provided in Table 1.

Table 1. Characteristics of the NPSMF. Source: [11].

Design Speed	30,000 RPM
Rotor Diameter	287.02 mm (11.3 in)
Tip Speed	406 m/sec (1332 ft/sec)
Maximum Mass Flow Rate	10.14 kg/sec (22.35 lbm/sec)
Specific Mass Flux	156.75 kg/sec-m^2 (32 lbm/sec-ft^2)
Tip Inlet Relative Mach Number	1.52
Maximum Pressure Ratio	1.70

C. EXPERIMENTAL DATA COLLECTION AND REDUCTION

Relevant experimental data for the present study include measured mass flow through the test article, measured pressure ratio across the test article, and measured isentropic efficiency of the test article. Actual measurements obtained from the TCR include atmospheric conditions, static temperatures and pressures, and total temperatures and pressures at various locations within the rig. Reduction of these measurements to obtain the desired performance parameters is discussed in McNab [11].

To obtain the required performance metrics along a given speed line, the rotor was first spun up to the desired speed using the compressed air drive turbine, with the TCR throttle in the fully open position. The rotor is then held at constant speed while the TCR throttle is incrementally closed to reduce the mass flow rate. At each increment the test article is allowed to reach steady-state, and the required measurements are recorded for that operating point. This process is repeated from the wide-open throttle condition until the compressor reaches the stall point for the present operating speed. Uncertainty in the measured values and reduced performance parameters was addressed by Thornton [15], who generated the error bars bounding the experimental data featured in this study.

The experimental data for the 90% speed line used in this study are provided in Figures 3 and 4. Data were collected using a smooth casing which implemented the smaller cold tip clearance (0.381 mm, 0.015 in).

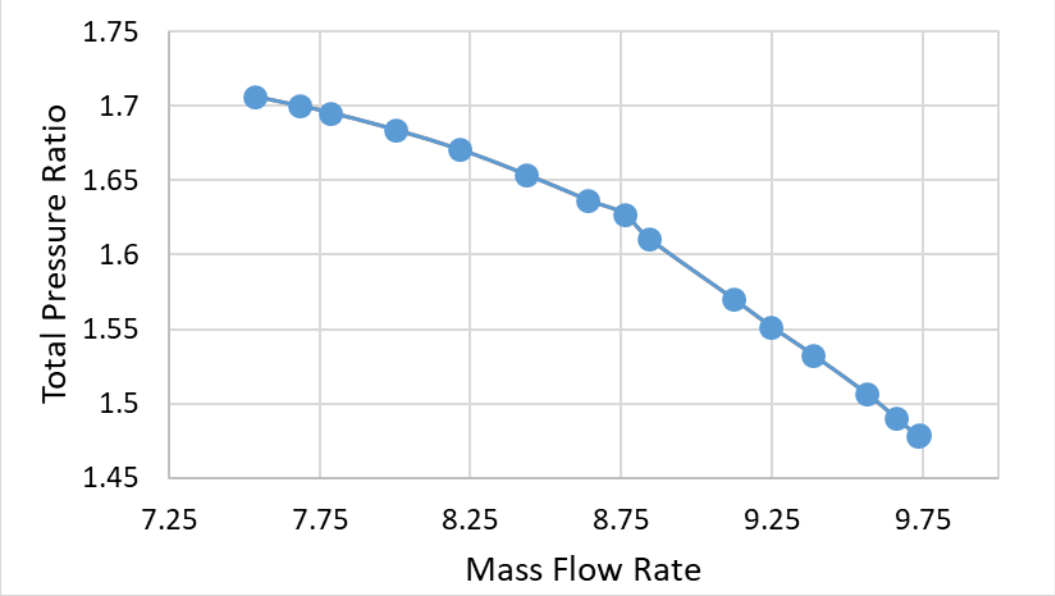

Figure 3. Experimental pressure ratio for the 90% speed line.

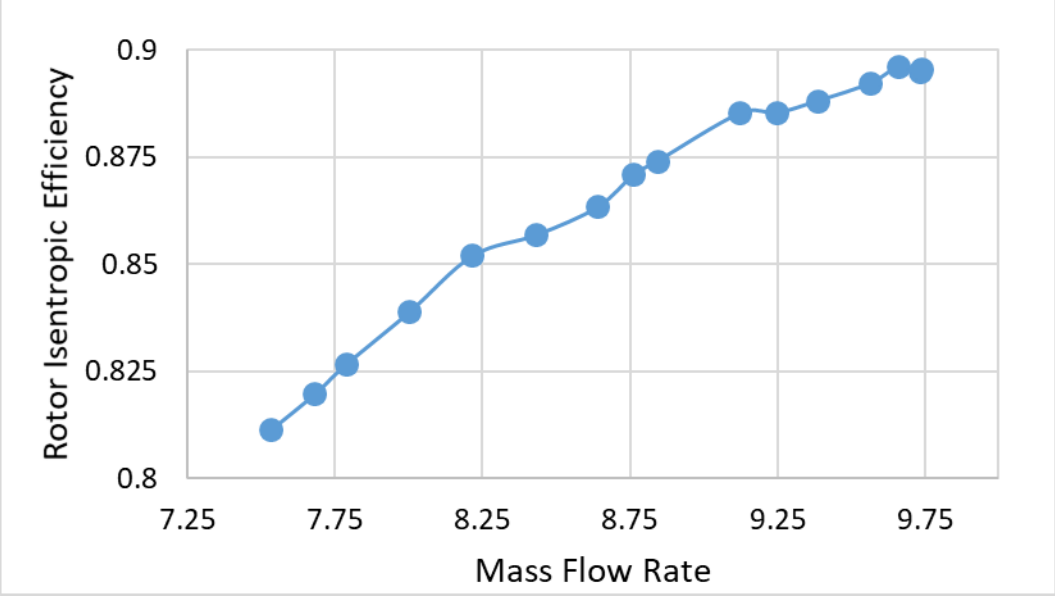

Figure 4. Experimental isentropic efficiency for the 90% speed line.

THIS PAGE INTENTIONALLY LEFT BLANK

III. COMPUTATIONAL SETUP

Numerical predictions of NPSMF rotor performance were obtained using gas path geometries developed in SolidWorks and fluid model using ANSYS CFX. Refinement of both the gas path geometry and fluid model are the subject of the present study. This chapter provides an overview of the methodology applied to the existing CFD structure and introduces the areas which were designated for improvement.

A. GAS PATH GEOMETRY

1. Rotor Geometry

The rotor geometry used to represent the NPSMF is shown in Figure 5. The dimensions of the fan geometry in SolidWorks match the dimensions of the fan listed in Table 1. This geometry is unchanged from the previous numerical studies of NPSMF performance.

Figures 6 and 7 illustrate the NPSMF integrated with its corresponding TCR components, namely the nose cone, rotor casing, inlet and outlet passages, spacers, and stator ring. Figure 6 provides an isometric view of this assembly, and Figure 7 provides a section view of the assembly. Integration of casing treatments into the CFD model is accomplished by substituting the casing included in Figures 6 and 7 with a SolidWorks model of the test article casing which incorporates the treatment under study.

An example of the possible casing treatments used to improve the NPSMF's stall margin is the circumferential groove which can be seen within the casing in Figure 7.

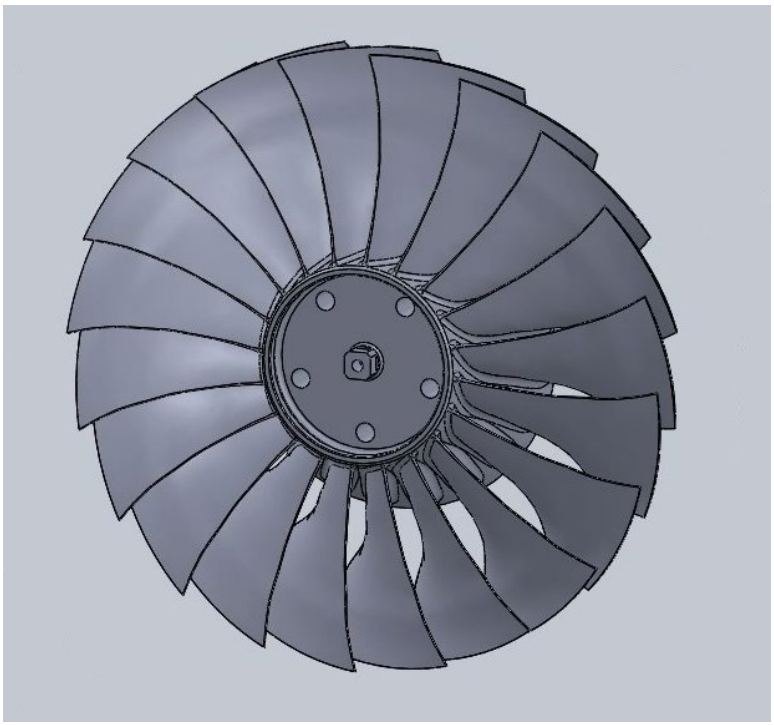

Figure 5. SolidWorks geometry used to represent the NPSMF.

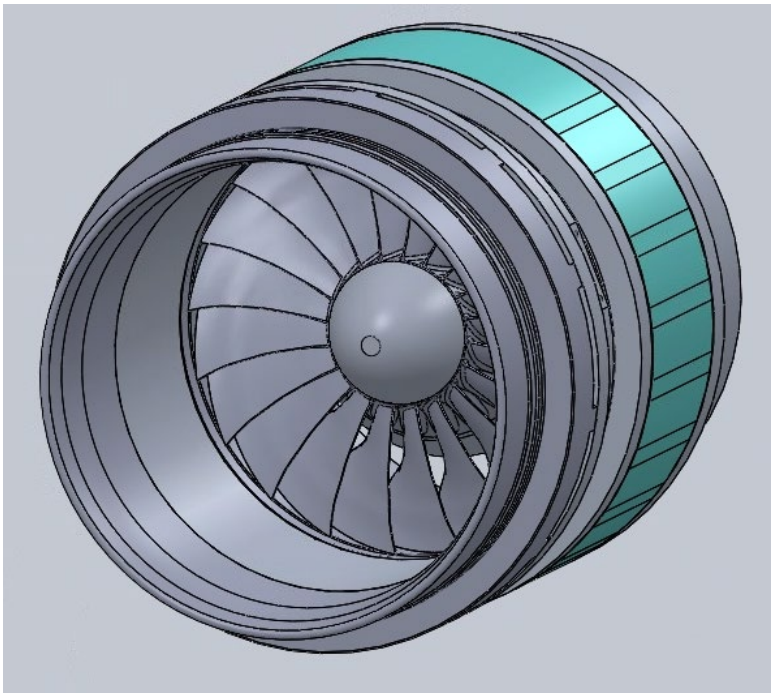

Figure 6. SolidWorks assembly of TCR geometry, isometric view.

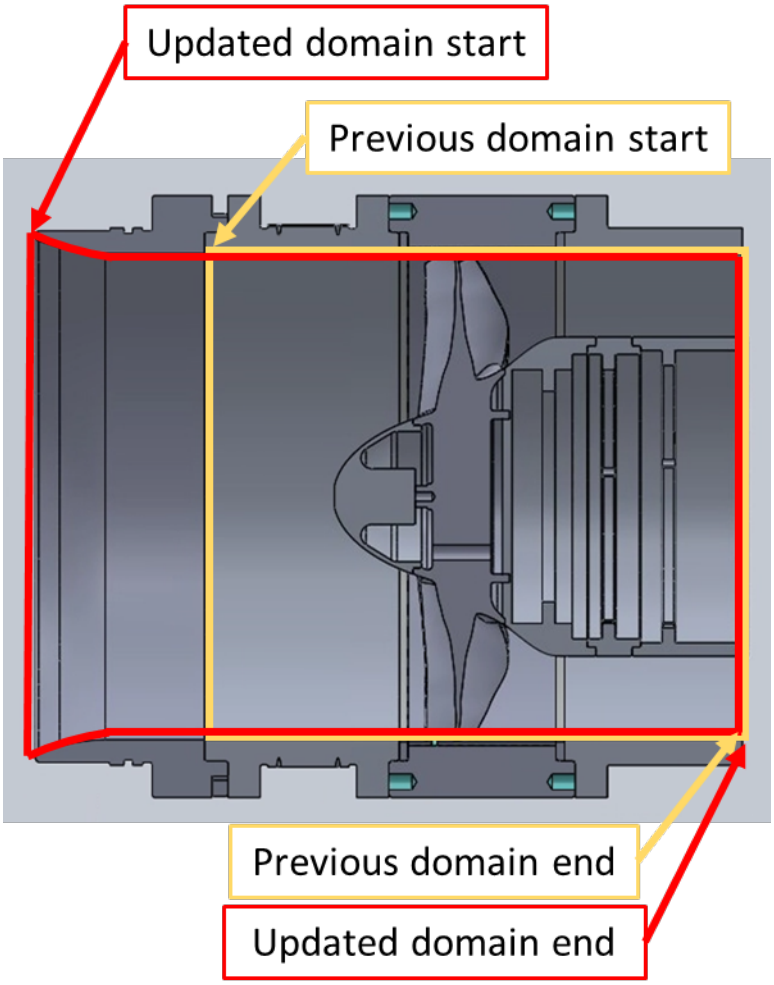

Figure 7. SolidWorks assembly of TCR geometry, section view.

2. Gas Path Construction

Studies up to and including the present one have been limited in scope to simulations of steady-state flow through a single blade passage of the NPSMF. The gas path geometry used in the previous works [11], [12], [15] is shown in Figure 8. Simulating a single blade passage rather than the entire blade row enables high-resolution modelling at a fraction of the computational expense. However, such a limitation necessarily hinders the ability to completely model stall, which is well-understood to be unsteady and to typically occur in cells spanning multiple blades.

The geometry pictured in Figure 8 was constructed by drawing splines midway between two neighboring blades at the tip and hub, then lofting a surface between the two

profiles. The leading edge and trailing edge were then extended directly upstream and downstream of the blade, and the combined upstream, blade, and downstream surfaces copied over to the next passage to encapsulate the blade of interest. The two passage boundaries were then used to loft a solid volume through the blade passage, which was then added to the assembly shown in Figure 6. The neighboring TCR components (nose cone, stator ring, etc.) and the blade were subtracted from the passage geometry, and the desired tip gap obtained by cutting material from the upper surface, resulting in the gas path pictured in Figure 8.

Using this process, the gas path geometry is then imported into ANSYS as a parasolid for meshing and simulation of fluid flow.

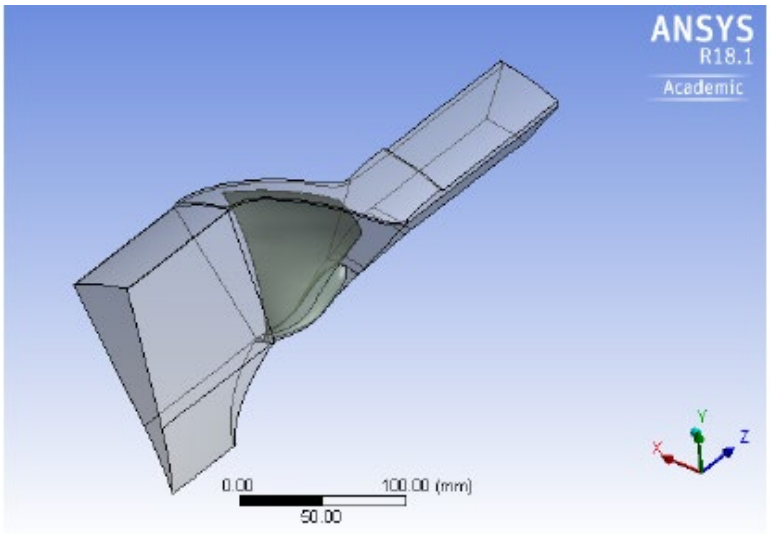

Figure 8. Gas path geometry used in previous studies and for the present mesh sensitivity study. Source: [15].

3. Areas for Improvement

While the existing geometry pictured in Figure 8 has provided sufficiently accurate results in previous studies, one focus of the present study is improving on the periodic boundary which encapsulates the blade. The NPSMF is an advanced-geometry rotor with complex contours, and the construction of the previous gas path using lofted surfaces between the tip and hub mid-passage contours results in a non-uniform distribution of

spacing between the blade surface and the periodic boundary. This treatment made the boundary of the previous geometry not perfectly periodic, which potentially altered the flow physics of previous simulations. An objective of the present study is thus to improve on the previous geometry by reconstructing the periodic boundary to uniformly follow the blade contours. By reconstructing the geometry in this manner, the present study sought to make the boundary perfectly periodic in order to enable more realistic flow modelling.

B. FLUID MODEL

1. Mesh Construction

Meshing for this study was accomplished using the built-in ANSYS meshing tool which accompanies CFX in Workbench. A patch-conforming method was used in conjunction with select application of inflation layers and face-sizing restrictions to construct a hybrid mesh with unstructured elements in the passage and structured elements near the blade, hub, and casing surfaces. One such mesh used in the present mesh sensitivity study is pictured in Figure 9.

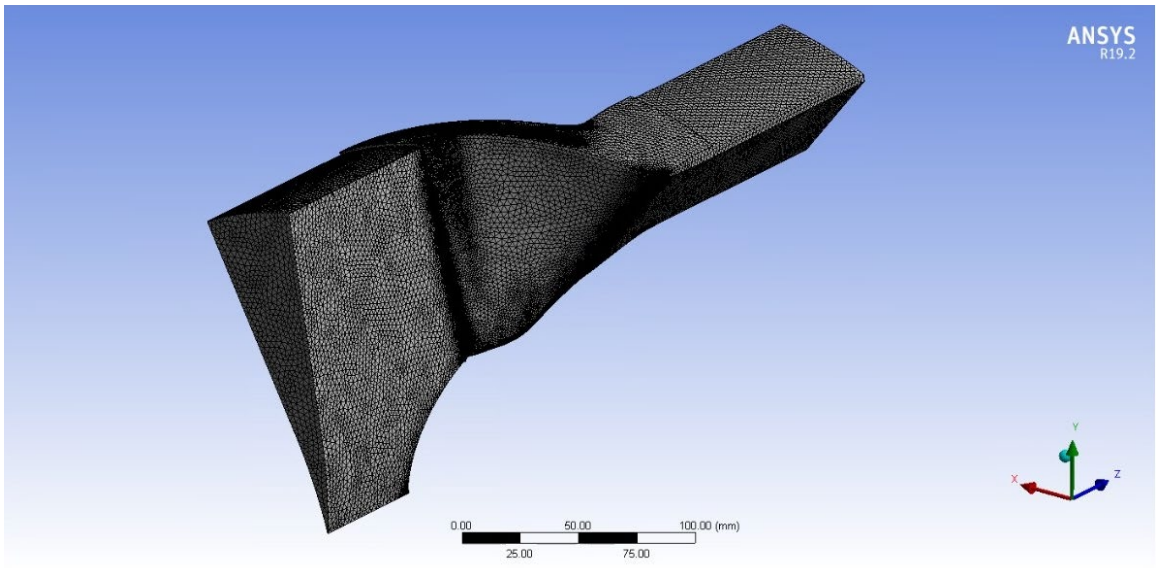

Figure 9. Example of meshed gas path geometry from mesh sensitivity study.

2. Flow Physics Selections (CFX-Pre)

Simulations of flow through the NPSMF were conducted using ANSYS CFX R19.2. Simulations were conducted for steady-state flow of compressible air using the shear stress transport (SST) turbulence model and the gamma-theta laminar-to-turbulent boundary layer transition model. Alternative configurations were also used for the mesh sensitivity study, including fully turbulent flow and k-epsilon turbulence with gamma-theta transition. These alternative configurations were implemented during the mesh sensitivity study to briefly probe for turbulence model dependence of the mesh sensitivity study results. The SST/gamma-theta configuration was the primary configuration used to predict performance and compare with experimental data.

Boundary conditions for this study included relative pressures at the inlet and outlet faces. Variation of operating condition along a speed line was accomplished by increasing the relative back pressure boundary condition as in the previous study [15], as well as decreasing the relative stagnation pressure at the inlet to better simulate operation of the TCR. Implementation of the throttled inlet boundary condition required the additional step of scaling the resulting mass flow rates, which was accomplished using ANSYS CFX-post.

IV. MESH SENSITIVITY STUDY

The present mesh sensitivity study sought to improve on the existing CFD model by refining the existing mesh until mesh convergence was achieved. The initial mesh used in this study was that used in the two-way FSI analysis of the previous work [15]. This mesh was fairly coarse in support of the high computational cost of FSI analysis, and consequently obscured flow features, especially in the near-stall region. Areas of emphasis during the mesh refinement process included y^+ on the blade surface, mesh skewness, bulk element size, and inflation layers on the blade surface.

A. OBJECTIVES

The objective of the mesh refinement process was to achieve mesh convergence by reducing the blade average y^+ value and generating uniform inflation layers around the blade surface.

The y^+ value is a non-dimensional distance from a surface based on turbulent friction velocity. Simulating flow with laminar-to-turbulent boundary layer transition requires a small y^+ compared to completely turbulent flows, as resolving boundary layer development is essential to accurately predicting the transition. The ANSYS CFX modelling guide recommends a y^+ between 0.1 and 1 when using the gamma-theta boundary layer turbulence transition model. Compliance with this requirement was assessed by evaluating the blade area average y^+ and by determining the maximum y^+ value on the blade in CFX-Post.

Uniformity of inflation layers was selected as a target for improvement because of the advanced geometry implemented in the NPSMF. Unlike more traditional blade designs, the NPSMF features highly three-dimensional and non-uniform twist, sweep, and taper, designed programmatically using CFD to maximize blade loading. As a consequence, grid generation for the NPSMF has proved challenging in previous studies. An objective of this study was thus to improve the mesh quality by manually identifying meshing parameters in ANSYS which resulted in adequate inflation layers around the entire NPSMF blade. The adequacy of inflation layers was assessed by visual inspection

of the mesh and of contour plots for flow properties along constant-radius surfaces. Adequate inflation layers extended uniformly outwards from the blade surface, extended sufficiently far into the bulk mesh, and were sufficiently fine such that flow features (namely normal shocks, separation bubbles, and viscous sublayers) were not smeared in contour plots.

Additionally, two tangential objectives of the present mesh sensitivity study were selected. These included implementing rotor operation using a depressed inlet stagnation pressure vice the boosted relative back pressure used in previous studies, as well as simulating the rotor using alternative turbulence and transition models to validate the use of SST/gamma-theta.

B. APPROACH

The mesh sensitivity study first addressed flow feature resolution, then addressed blade y^+ reduction. Flow feature resolution was achieved primarily through improvements to the inflation layer generation, but also by manipulating several other bulk mesh settings. The following mesh parameters were used to improve the mesh quality. The quality of a given mesh was assessed using the criteria described in the previous section.

- Bulk mesh size
- Inflation first layer thickness
- Inflation max layers
- Face sizing on the leading & trailing edges
- Edge sizing on the leading and trailing edges

Throughout the mesh refinement process, the capability of ANSYS to mesh the NPSMF geometry was found to be exceptionally sensitive to the above-listed refinement parameters. In many cases, an attempted mesh refinement resulted in a failed mesh. Mesh failures resulted most often from failed inflation layers, small element volume, or

excessively skewed mesh elements. The following parameters were thus used to complement the above-listed mesh improvement parameters. These parameters did not directly improve the mesh, but add necessary constraints which enforce the desired mesh improvement or prevent the meshing program from failing.

- Target skewness
- Mesh smoothing
- Capture curvature
- Capture proximity
- Defeature size
- Face sizing on the hub, leading edge, and trailing edge

Table 2 summarizes the mesh features used, their respective locations within the flow domain, and their relative importance to the quality of the mesh as measured by the previously-defined metrics.

Table 2. Mesh features with their locations and relative importance.

Location(s)	Mesh Feature	Effect(s)	Relative Importance Low (1)-->High (5)
N/A	Bulk mesh size	Mesher/Solver time	3
		Overall flow resolution	4
		Shock resolution	5
		Solver stability	2
Blade surface	Inflation Settings*	Blade Yplus	5
Blade LE/TE		Shock resolution	2
Hub surface		Mesher/Solver time	4
Casing wall		Inflation uniformity	5
Inner wall		Meshing Success**	4
Blade surface	Face Sizing	LE/TE faceting	5
Blade LE/TE		Inflation aspect ratio	4
Hub Surface		Mesher/Solver time	5
		Overall flow resolution	3
		Inflation uniformity	4
		Overall mesh quality**	3
Periodic surfaces	Match Control	Overall flow resolution	3
		Shock resolution	2
		Solver time	4
N/A	Global mesh quality & sizing settings***	Overall mesh quality**	2
Small faces/edges	Pinch Controls	Overall mesh quality**	1
		Inflation layer uniformity	1
N/A	Virtual Topology (Automatic)	Overall mesh quality**	1
Small faces/edges	Virtual Topology (Manual)	Overall mesh quality**	1
* Refers to Inflation first layer thickness, selection of surfaces to inflate, maximum number of inflation layers, inflation growth rate, and inflation algorithm			
** Refers to the ability of Ansys meshing module to successfully generate a mesh using the given settings			
*** Includes automatic mesh defeaturing, curvature capture, proximity capture, target metrics (skewness, orthoganality, aspect ratio, etc.)			

Using the above-listed parameters the initial mesh was iteratively refined by first selecting a desired improvement area (for example, inflation layer uniformity on the suction side of the blade surface), applying the mesh improvement parameters to achieve the desired improvement (by separating the suction and pressure side inflation layers into two separate entities, increasing max inflation layers, or decreasing bulk mesh size). If the mesh failed or resulted in solver errors, the additional parameters were then manipulated to improve the refined mesh (decreasing target skewness, increasing mesh smoothing, or decreasing curvature normal angle). The improved mesh was then simulated along a partial speed line, and the results were used to inform the next iteration of mesh refinement. This process was repeated until a refined mesh achieved a similar level of model fidelity to the previous study's cold-shape coarse mesh results.

Each mesh was simulated along a partial 90% speed line for comparison to the existing CFD performance predictions and to the experimental data. During the course of the mesh sensitivity study, it was observed that the refined meshes often failed to converge past 10^{-4} on RMS residuals of U, W, and V-momentum and mass conservation. The stopping criterion for each simulation was set to 10^{-6} RMS U, V, and W-momentum and mass conservation residuals. To mitigate the numerical instability inherent to this study, the boundary conditions listed below were chosen for the initial runs of each partial speed line construction.

- 0kPa Relative inlet stagnation pressure
- [-10kPa, 0 kPa, +10 kPa] Relative back pressure

These boundary conditions were selected for the initial runs of each mesh because they correspond to the highest-efficiency and most stable operation of the fan. This limitation resulted in a high concentration of CFD predictions on the right-hand side of the compressor map, thus offering no insight into the performance of each mesh in the near-stall region. However, this limitation was deemed acceptable, as the objective of the mesh sensitivity study was to achieve mesh convergence and not to predict a complete speed line using each mesh iteration.

The introduction of the depressed inlet pressure condition was performed during simulation of the third mesh iteration. Initial results using this configuration closely followed results from the boosted relative back pressure configuration, so all subsequent simulations were thus conducted using the depressed inlet pressure condition. This modification increases CFD fidelity to the real rotor by accounting for Reynold's number effects through the inlet, which are especially prominent in the near-stall region. Simulations using the throttled inlet boundary condition applied the following boundary conditions in order to maximize stability for the first runs of each mesh.

- [+10 kPa, 0 kPa, -10 kPa] Relative inlet stagnation pressure
- 0 kPa Relative back pressure

Beyond these starter boundary conditions, the inlet stagnation pressure (or relative back pressure) were varied fairly widely in order to simulate the largest portion of speed line in the fewest number of runs possible. For this reason, the CFD predictions presented for each mesh's respective partial speed line vary in their uniformity and placement along the speed line.

In addition to the throttled inlet boundary condition, alternative turbulence models and transition models were implemented to validate the use of SST/gamma-theta. These selections were made in order to probe for better numerical stability and to compare the results with SST/gamma-theta, previous CFD, and experimental data. Speed lines which implemented these alternative configurations are indicated as such in the following section.

C. RESULTS

Using the process described in the previous section, four iterations of mesh refinement were completed and simulated under various conditions for comparison to previous CFD results and to experimental data. A summary of the starting mesh, intermediate meshes, and final mesh is provided in Table 3. While the final mesh (mesh 4) has a y^+ value below the recommended range of 0.1 to 1 for the gamma-theta turbulence transition model, the results obtained using that mesh were satisfactory and stable for the partial speed line.

Table 3. Summary of meshes from mesh sensitivity study

Mesh	Nodes	Elements	Blade average y^+
0	1,173,670	3,595,317	208.399
1	3,977,379	10,113,366	4.975
2	3,735,985	8,299,061	8.374
3	3,800,067	8,618,960	2.891
4	6,785,278	16,529,255	0.0515

The performance maps of total pressure ratio and isentropic efficiency for the rotor are provided in Figures 10 and 11. The data show that initial mesh refinement pushed the CFD predicted performance further from the experimental data, but then rejoined the initial CFD prediction upon further refinement. This behavior reflects numerical instabilities found within the flow during initial refinement which were then resolved with further refinement. In this case, instabilities most likely resulted from flow features bouncing back and forth between neighboring mesh elements. Whereas the initial coarse mesh blurred flow features (namely, normal shocks and bow shocks) into single mesh elements, initial refinement split these features into neighboring elements, and further refinement adequately resolved these features into their correct steady-state locations.

Concluding the present mesh sensitivity study, performance predictions after further refinement showed little change from those obtained using the final mesh. This result indicates that mesh convergence has been achieved for the NPSMF cold-shape geometry, and no further refinement was required.

In the next chapter, a process is described in which the previous fluid domain geometry (the domain used in the mesh sensitivity study) is reconstructed to provide better flow modelling in the near-stall region. This improved geometry was then meshed using parameters derived from the final grid in this sensitivity study, making the final mesh of this sensitivity study and the mesh used for stall characteristic prediction two separate but similar grids.

The resulting improvement from previous CFD predictions observed in Chapter VI of this study is thus a combination of improvements due to grid refinement and geometry reconstruction. The grid refinement process improved on previous results by more accurately representing the laminar-to-turbulent boundary layer transition and resolving flow features in the passage, as described earlier in this chapter. Improvements to previous results due to geometry reconstruction are explained in the following chapter

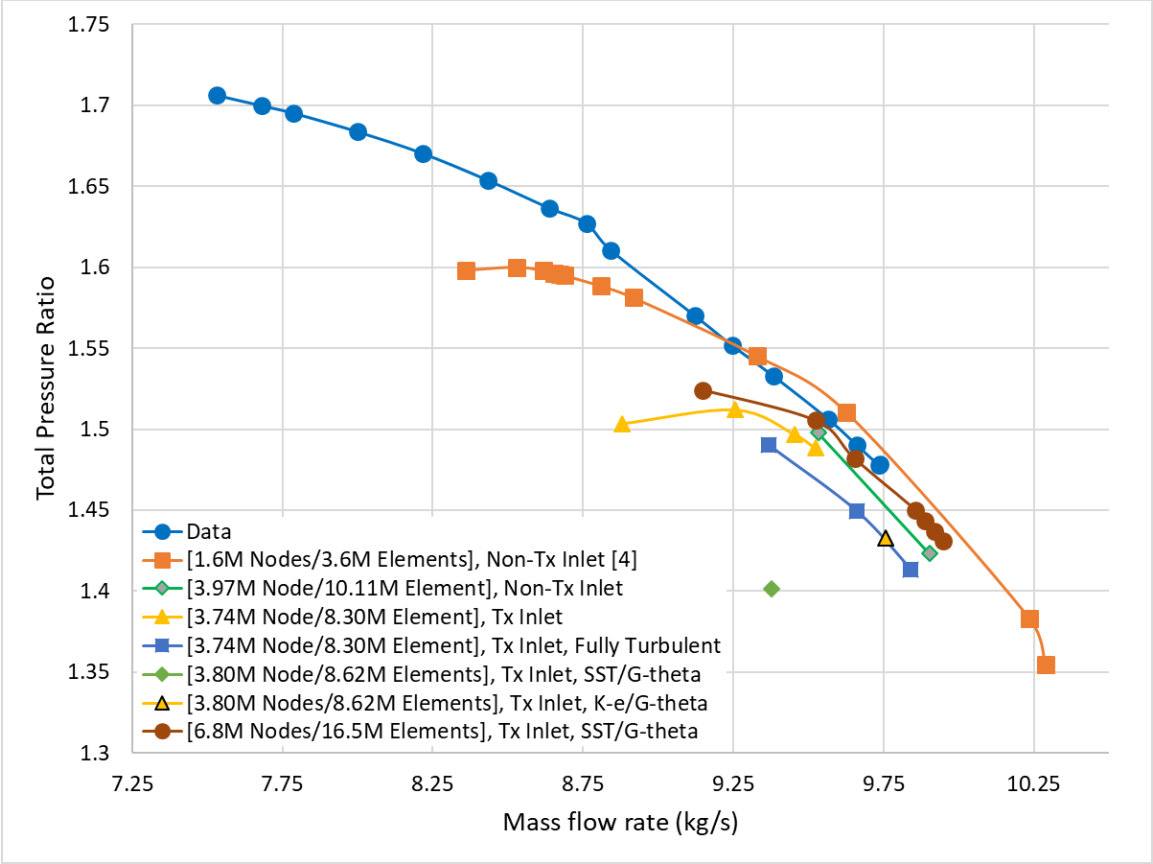

Figure 10. Total pressure ratio map for the mesh sensitivity study.

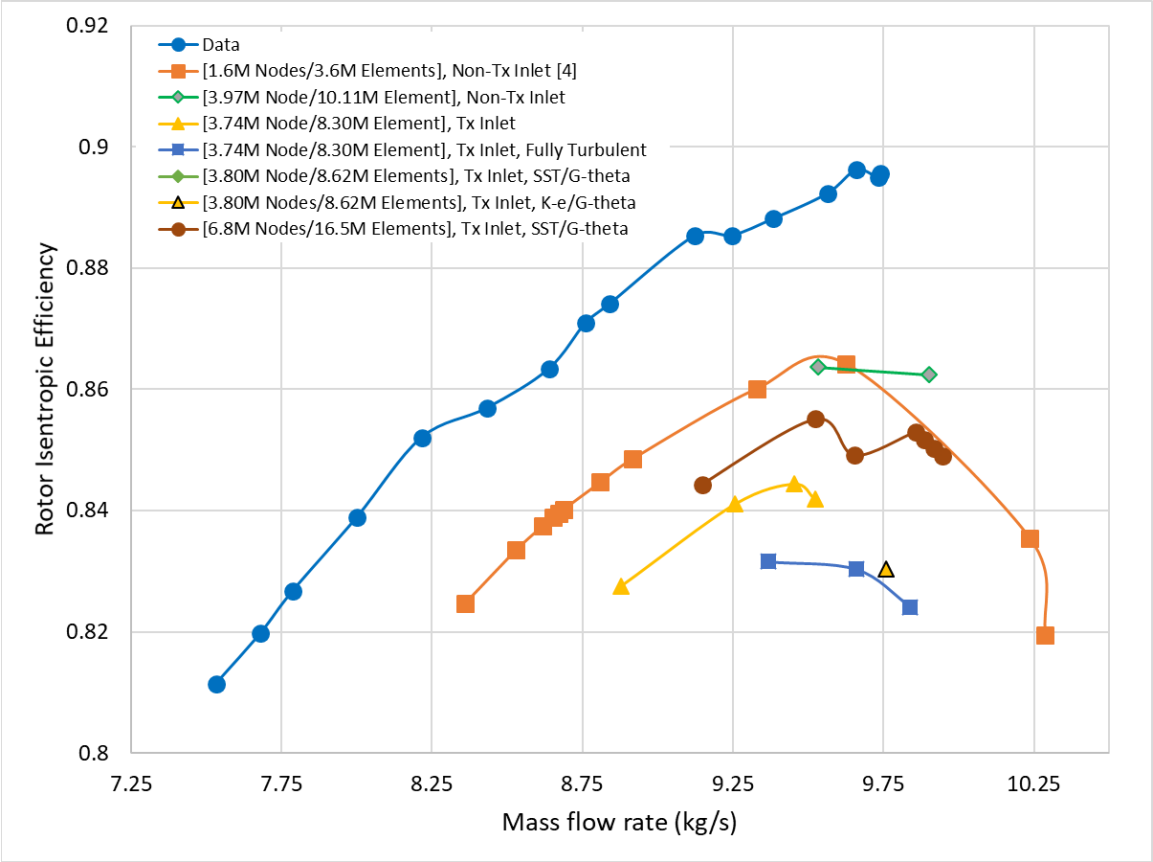

Figure 11. Isentropic efficiency map for the mesh sensitivity study.

THIS PAGE INTENTIONALLY LEFT BLANK

V. GEOMETRY REFINEMENT

A. OBJECTIVES

The present section describes a process in which the SolidWorks geometry passed to ANSYS for meshing and CFD simulation was reconstructed from first principles in order to provide a more realistic periodic boundary for single-blade passage flow simulations, and to accomplish additional objectives which support other TCR research.

The primary objective of the present geometry improvement process was to develop a single-blade passage geometry which conforms perfectly to the blade surface and minimizes surface area differential between the two periodic boundary surfaces. These features are significant improvements from the previous geometry because they enable the use of the match control feature in the ANSYS meshing module. *Match control* is a feature which instructs the ANSYS meshing module to create 1:1 matches between mesh elements on a periodic boundary for rotational flows such as those found in the NPSMF. Without match control enabled, the CFX Solver must interpolate between the upstream periodic boundary interface and the downstream periodic interface, using an algorithm known as general gird interface (GGI). This interpolation requires additional computation time and introduces errors when features such as shocks or separated flow regions span across the periodic boundary. With match control enabled, no such interpolation is necessary and the CFX Solver obtains a better solution at less computational expense. In the previous work, match control was not used because the previous geometry's periodic surfaces were slightly dissimilar, which prevented the ANSYS meshing module from generating 1:1 element pairs. The present study took great care to ensure that the improved geometry would meet the requirements necessary to enable match control.

An additional goal of the present geometry improvement process was to include a framework for the implementation of future advanced casing treatments. This was accomplished by accounting for the TCR components surrounding the NPSMF in a single step, rather than by compounding several steps. This solution is advantageous to future work because implementation of additional casings may be accomplished by first mating

the new casing to the TCR assembly in SolidWorks, then by repeating the same operation described in this section without any further modification required.

Finally, a tangential objective of the present geometry improvement process was to allow for implementation of multiple blade passage simulations for future work. The present study does not attempt to address multi-blade passage simulations, however such simulations are a recommendation for future work in order to validate the use of single-blade simulations.

B. APPROACH

1. Background

Initial development of the previous NPSMF single-blade passage geometry is detailed in McNab [11], and later refinement is described in DeSousa [12]. The region of interest for the present geometry refinement process is the periodic boundary directly adjacent to the blade. This region is highlighted in Figure 12. The previous studies constructed this boundary by drawing conformal splines adjacent to the blade tip and hub which bisected the passage adjacent to the blade. A surface was then lofted between these two splines which became the periodic boundary adjacent to the blade, and the rest of the fluid domain was constructed from this surface. The resulting loft-based geometry did not conform to the blade surface and included features on the periodic surface which were not identical from side to side, and was thus not a true periodic boundary (and thus incapable of using match control). While the previous geometry yielded suitable results for previous studies, a true periodic boundary is necessary to accurately model flow through the rotor in the near-stall region and in the stalled condition.

The present geometry is based upon a blade-conforming surface which forms a true periodic boundary. The fundamental difference between construction of the conformal surface and the non-conformal surface is subtle, but important. The remainder of this section explains the design principals implemented to obtain a true periodic boundary capable of match control.

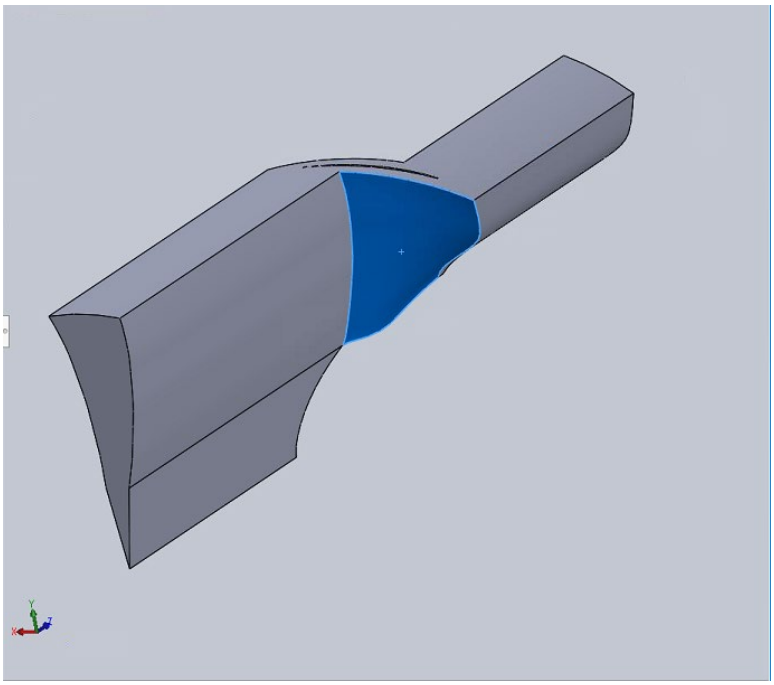

Figure 12. Periodic boundary adjacent to the blade.

2. Blade-Conforming Spline Construction

The improved geometry began by considering the SolidWorks model of the NPSMF itself, pictured in Figure 13. The process described in this section details the steps used in order to construct the four conformal splines, pictured in Figure 14, which form the basis of the improved fluid domain geometry.

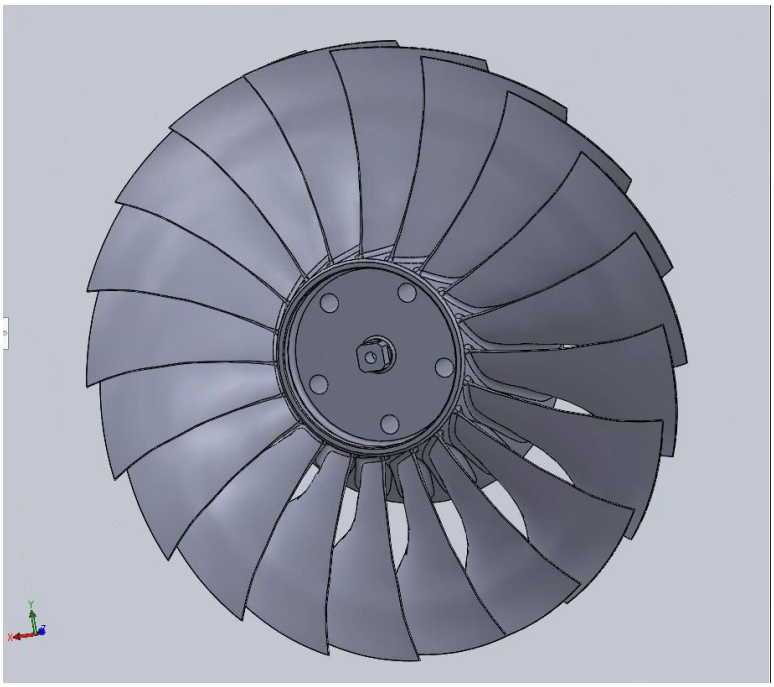

Figure 13. SolidWorks model of the NPSMF, starting point for fluid domain construction.

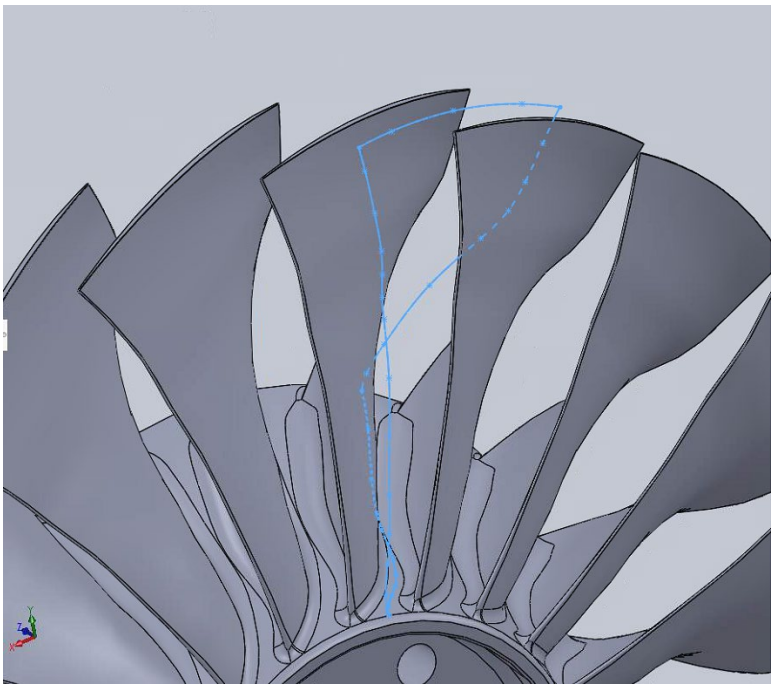

Figure 14. Four blade-conforming splines used in the improved geometry.

a. Hub Surface Spline

The first spline addressed is that which tracks bisects the passage along the surface of the blisk hub. Implementation of the design principles used to construct this spline is pictured in Figure 15, and the completed spline is pictured in Figure 16. The hub spline was constructed by defining reference planes at several locations along the length of the blade passage, each being perpendicular to the hub-blade fillet intersection edge. For each reference plane, the *intersection curves* sketch feature was used to draw a line along the hub surface where the hub intersected the reference plane. The midpoint of this line was then found, and its location marked with a 3-D sketch point. With a sufficient number of passage midpoints marked, a 3-D spline was drawn which connected all of the midpoints, thus bisecting the passage along the hub surface.

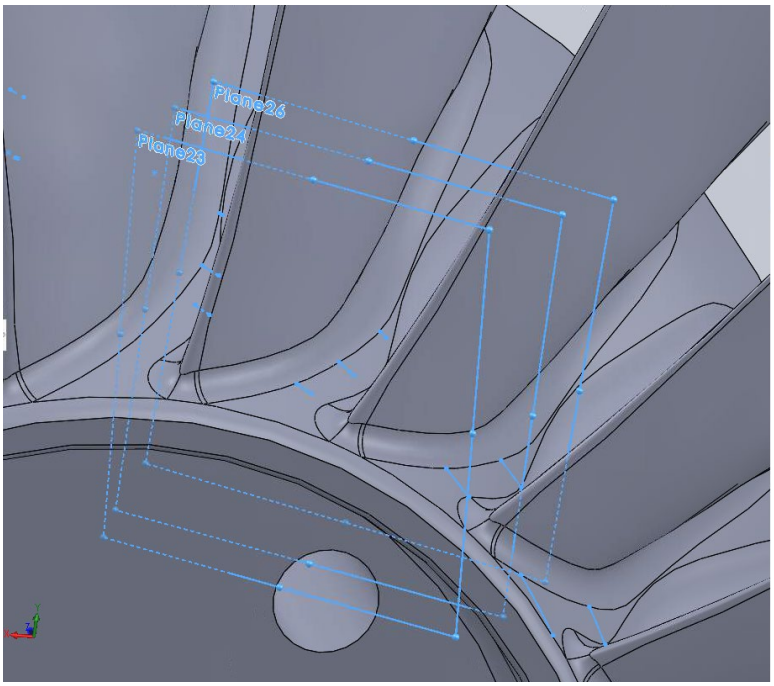

Figure 15. Construction technique used to draw the hub surface spline.

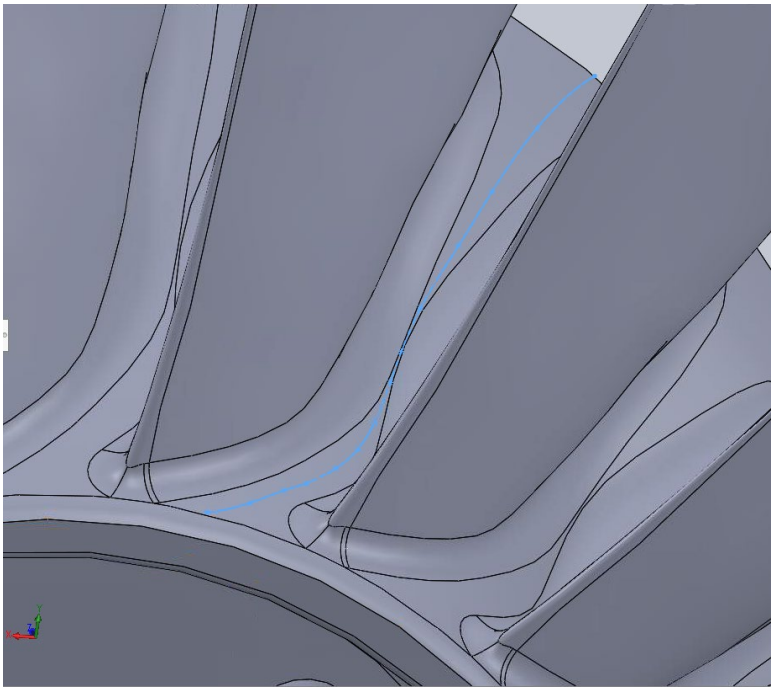

Figure 16. Completed hub surface spline.

b. Trailing edge spline

The technique developed to construct the trailing edge-conforming spline is depicted in Figures 17, 18, 19, and 20, and the completed spline is depicted in Figure 21. The technique used to construct this spline began by creating 3D sketch points at several locations along the trailing edge of the blade of interest. These points were then projected onto a reference plane parallel to the front plane. A projection of the adjacent blade's trailing edge was then added to the same sketch, and concentric arcs were drawn to create a rotationally symmetric set of points on the adjacent blade. The result of these steps is the SolidWorks construction geometry pictured in Figure 17.

Using 3D sketches to directly map points from one blade to another using concentric arcs was attempted, but found to be unsuccessful. SolidWorks 2018 does not allow users to snap sketch features to midpoints of 3D sketch lines, which precluded the technique of splining together midpoints of sketch entities spanning the blade passage. Because of this limitation, the present technique describes a process by which a series of 2D arcs were used to span the blade passage along the trailing edge

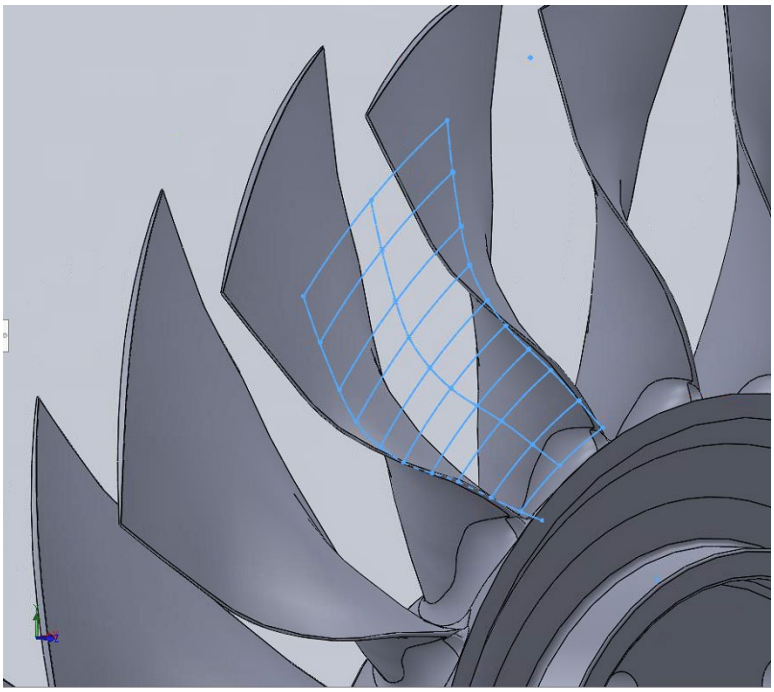

Figure 17. Technique used to construct trailing edge spline (1 of 4).

The new set of mirrored points was then mapped onto the surface of the adjacent blade by drawing reference planes coincident to each mirror point and parallel to the top plane. Intersection curves were then drawn to mark the line along which each reference plane intersected the adjacent blade. The intersection of these lines with the adjacent blade trailing edge were thus the mirror points mapped onto the surface of the adjacent blade trailing edge. This mapping technique is depicted in Figure 18.

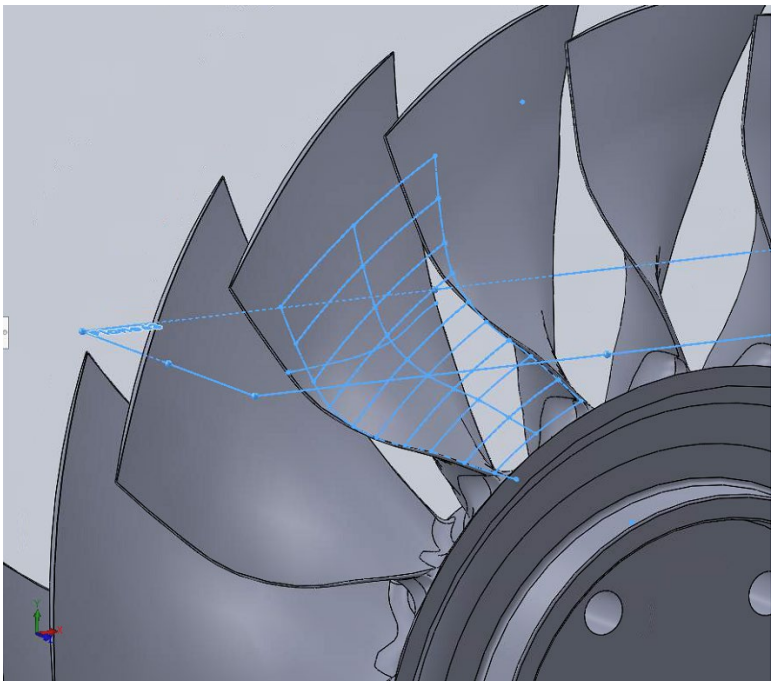

Figure 18. Technique used to construct trailing edge spline (2 of 4).

With symmetric points mapped to each blade trailing edge surface, a series of concentric 2D arcs could be drawn by sketching along reference planes coincident to each pair of points and perpendicular to the top plane. This process is depicted in Figure 19. Because the resulting sketches were 2D, their midpoints could be used as points for a 3D spline. Using this technique accounted for the non-planar curvature of the trailing edge, which is easily observed in Figure 20.

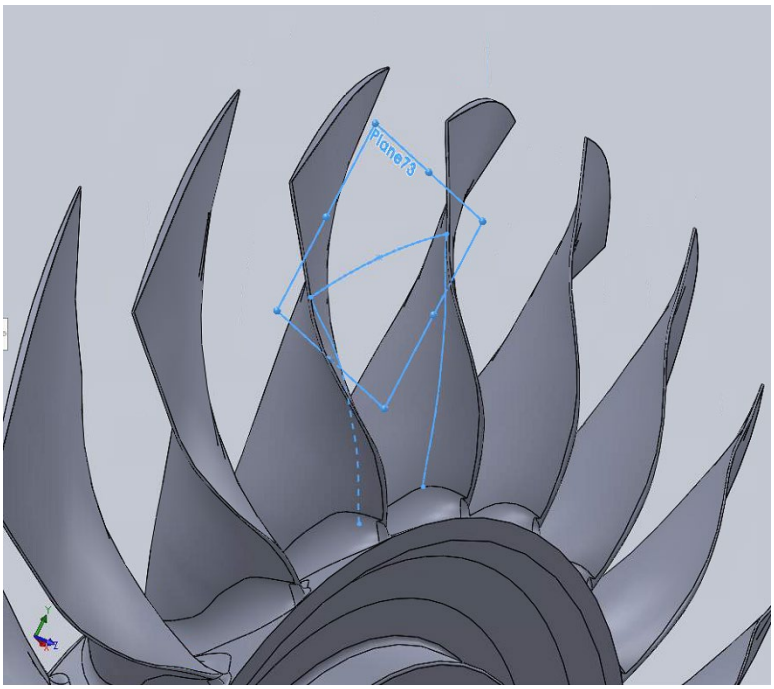

Figure 19. Technique used to construct trailing edge spline (3 of 4).

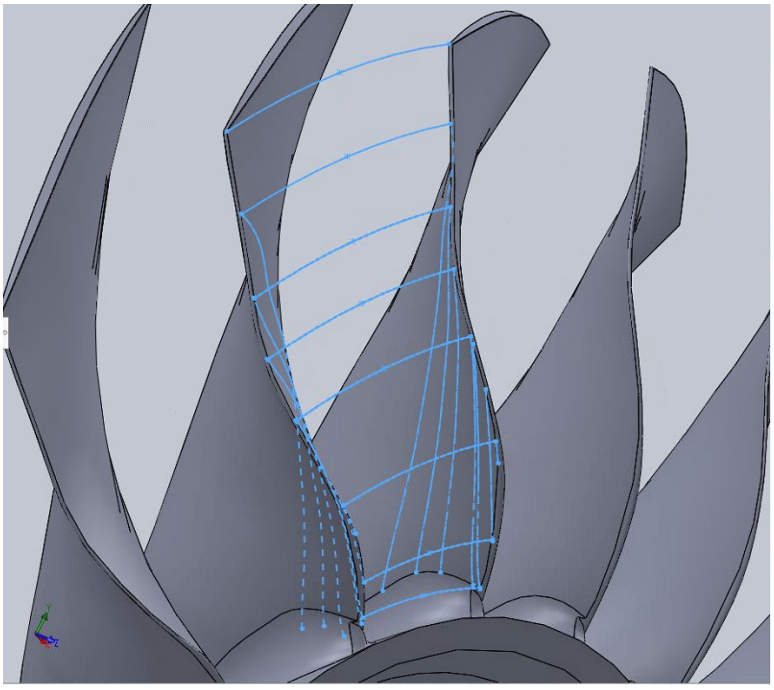

Figure 20. Technique used to construct trailing edge spline (4 of 4).

The resulting conformal trailing edge spline was drawn by connecting the midpoints of the concentric 2D arcs spanning the blade passage. This spline is pictured in Figure 21.

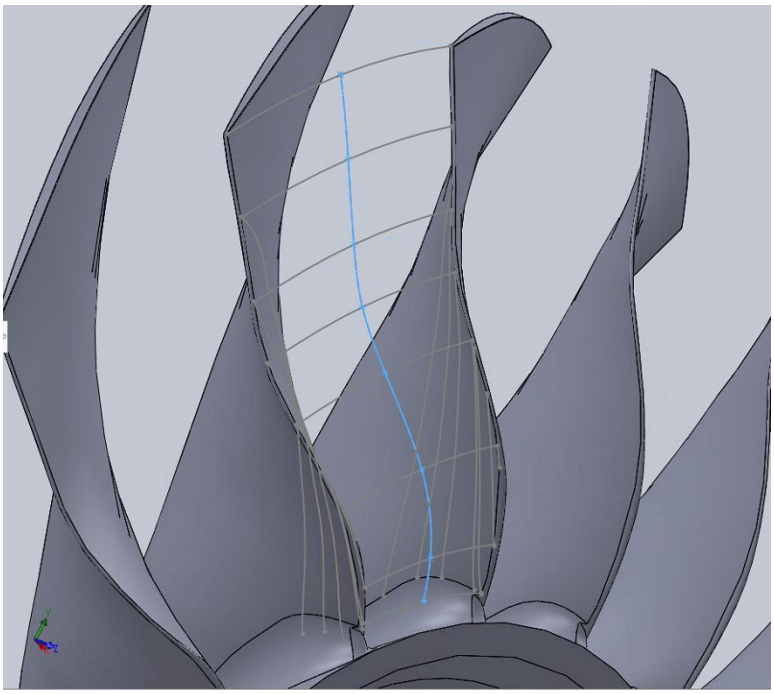

Figure 21. Completed trailing edge spline.

c. Leading Edge Spline

The leading edge spline was constructed using a technique similar to that used for the trailing edge spline. However, rather than mapping planes away from the first blade, over to the adjacent blade, then forward onto the second blade, the present technique used a projection of the second blade onto a 2D sketch referenced to the first blade in order to simplify the process. Figure 22 depicts the simplified technique, and Figure 23 depicts the completed leading edge-conforming spline.

The technique depicted in Figure 22 utilized a set of 3D sketch points placed along the leading edge of the blade of interest. For each point, a reference plane was defined with inputs coincident to the point and parallel to the front plane. The blade of interest and the adjacent blade were then projected onto the sketch plane using either the convert entities

or intersection curves features in SolidWorks. The projection feature was interchanged along the length of the leading edge because of the leading edge sweep incorporated into the NPSMF's design. A concentric arc was then drawn on each 2D sketch plane connecting the two leading edges. Being 2D sketches, the midpoint of each arc was available for snapping additional sketch features. Using several such arcs along the leading edge of the blade, the complete spline was drawn by connecting midpoints as depicted in Figure 23.

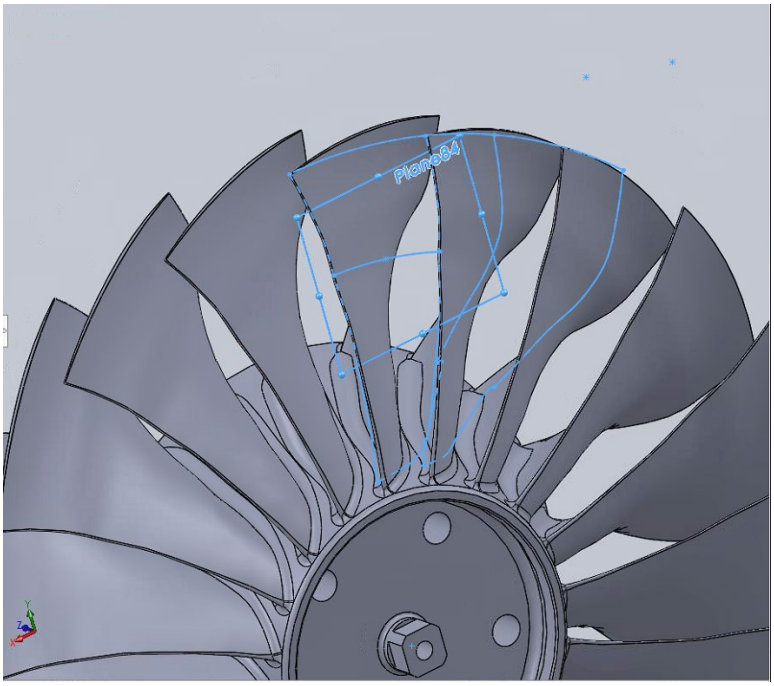

Figure 22. Technique used to construct the leading edge spline.

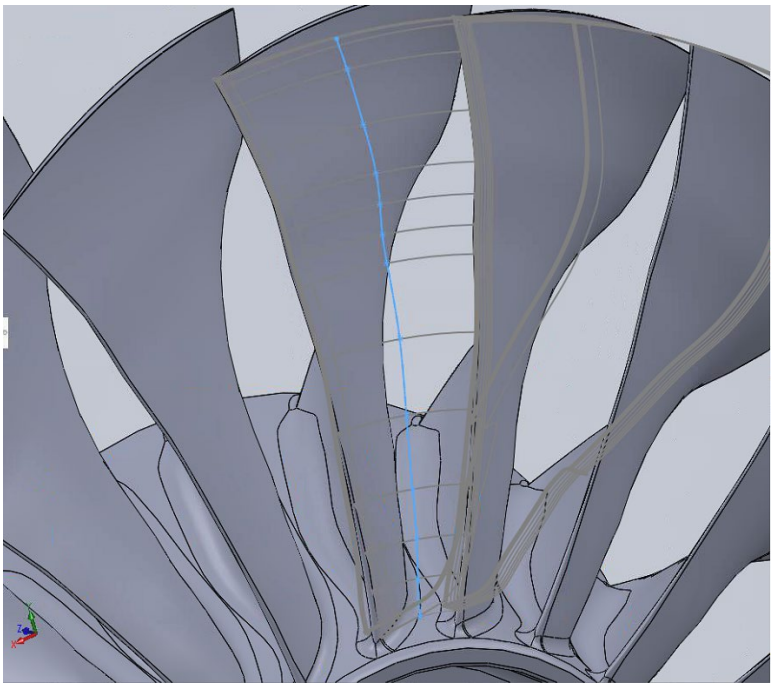

Figure 23. Completed leading edge spline.

d. Blade Tip Spine

The blade tip spline was constructed in similar fashion to the hub surface spline, except that the reference planes used here were defined as parallel to the front plane rather than normal to the hub-blade intersection edge. Construction of the tip spline began with a selection of 3D sketch points was placed along the tip of the blade of interest, and at each point a reference plane defined coincident to the point and parallel to the front plane. Using a 2D sketch placed on each reference plane, the intersection curves feature was used to map the location of a corresponding point along the tip of the adjacent blade. On the same 2D sketch, an arc was then drawn connecting the two points. With several such arcs constructed along the axial length of the passage, a 3D spline could then be used to connect the midpoints of each arc, thus forming a conformal spline bisecting the tip of the passage. This process is depicted in Figure 24, and the complete tip spline is depicted in Figure 25.

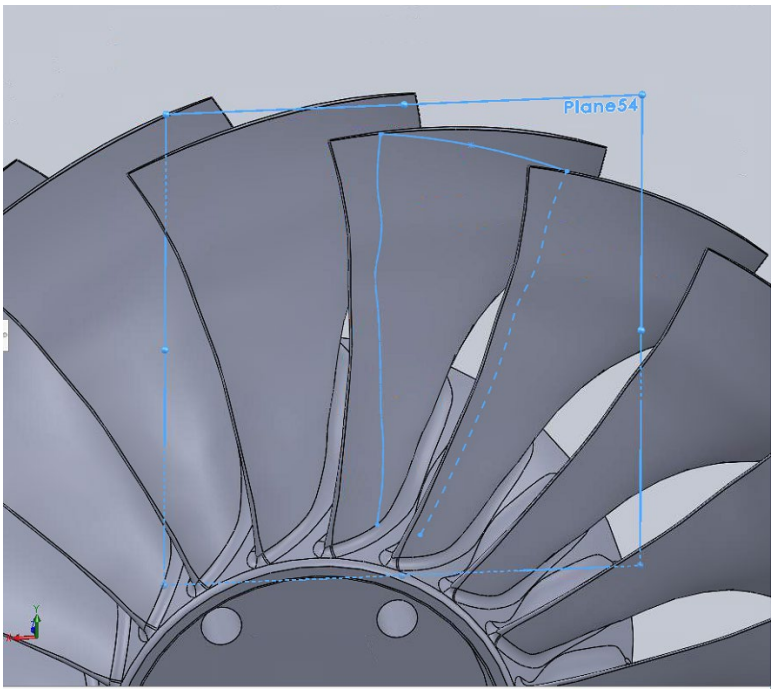

Figure 24. Technique used to construct tip spline.

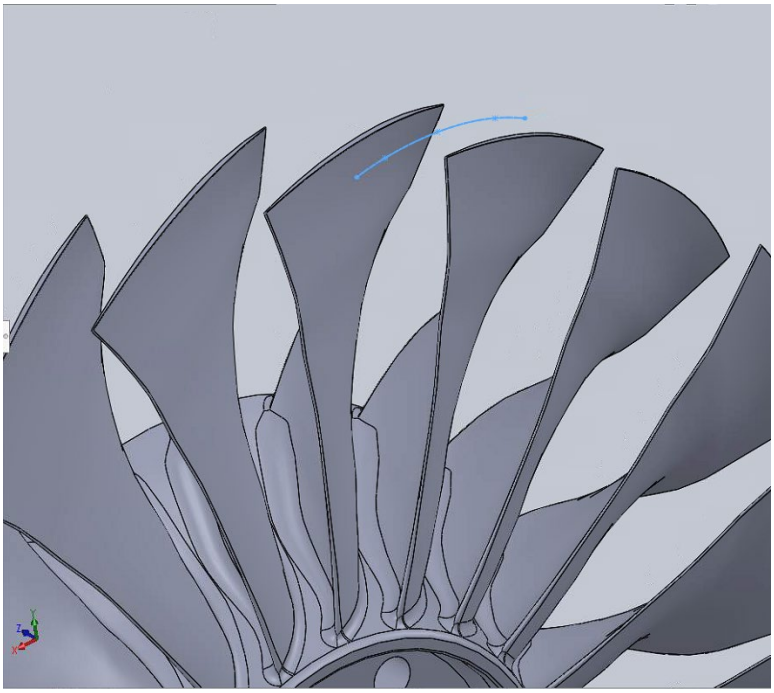

Figure 25. Completed blade tip spline.

e. Completed Blade-Conforming Spline

Using the techniques described in the previous sections, a single, closed-curve blade-conforming spline was constructed by connecting each spline. Some adjustment of spline points closest to the corners was necessary in order to prevent abnormal features which did not adequately represent the blade. Such adjustments were cosmetic in nature, and only improved the final product of this process. The complete blade-conforming spline is pictured in Figure 26.

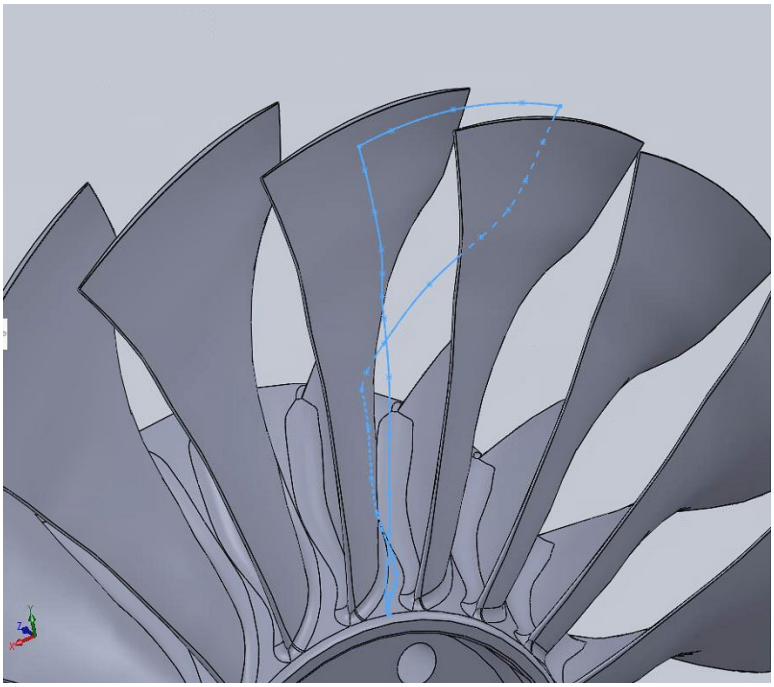

Figure 26. Completed blade-conforming spline.

3. Blade Passage Volume Construction

The present section describes the process by which the conformal splines described in the previous section were expanded upon in order to construct 3D geometry for a single blade passage fluid domain with zero, narrow, and wide tip-gaps.

The first step in the present process was to convert the closed curves described in the previous section into a surface, using the surface fill feature in SolidWorks. The filled surface resulting from this step is depicted in Figure 27.

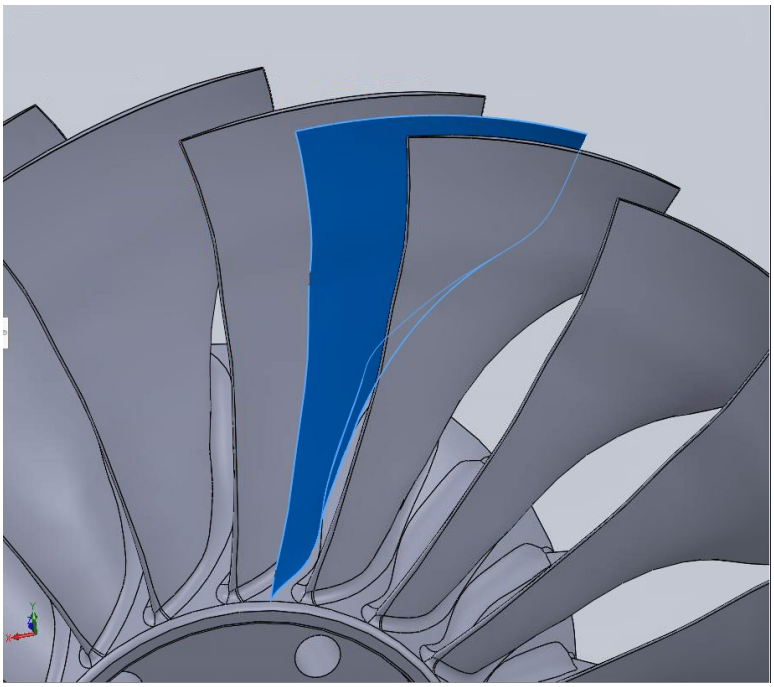

Figure 27. Blade-conforming surface filled from conformal splines.

The blade-conforming surface was then extended well above the blade tips (approximately 7.62mm, or 0.300 in) using the surface extend feature to allow for tip-gap construction. An additional surface was also constructed which extended the blade-conforming surface to the rotor centerline. The addition of these two surfaces is depicted in Figure 28.

With the full radius now spanned, the leading and trailing edges of the combined surface were projected upstream and downstream by a sufficient distance to capture the full length of the TCR assembly. A surface loft was then performed to connect the projected edges to their respective counterparts on the existing surface. The surface fill feature was considered for this step, but was found to severely distort the resulting surface. The surface loft feature was found to have no such issue. The result of this step is depicted in Figure 29.

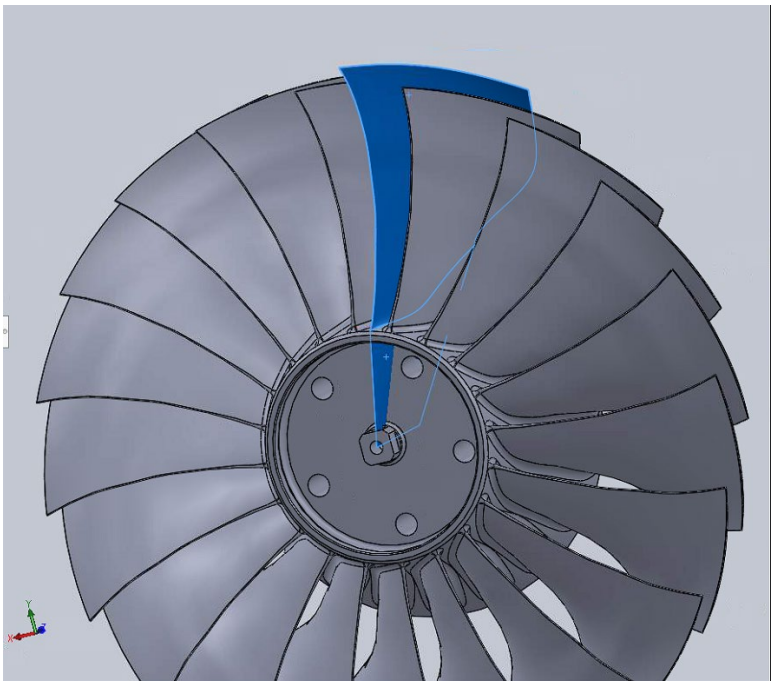

Figure 28. Surfaces extended above and filled below the blade-conforming surface.

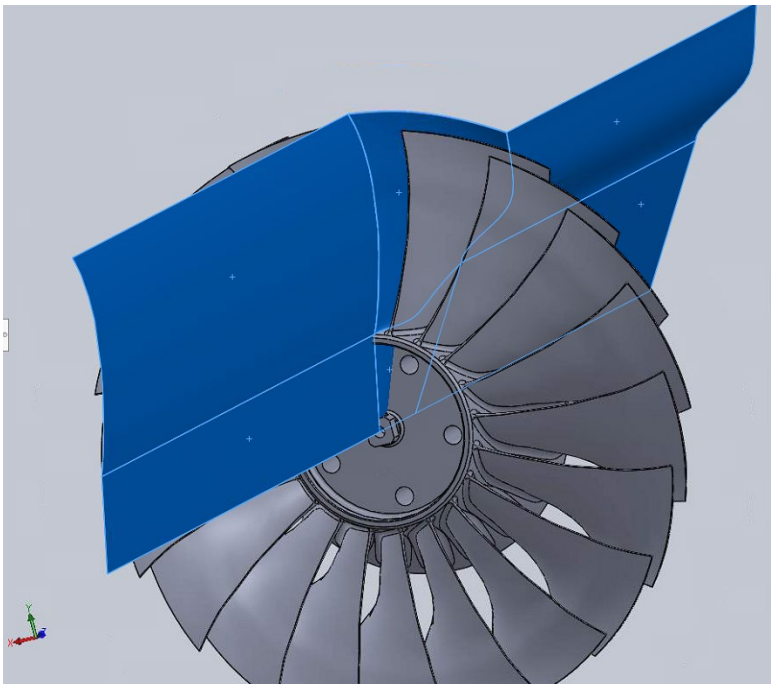

Figure 29. Surfaces lofted in the streamwise direction.

The resulting surface comprised a complete periodic boundary for the fluid domain. The corresponding periodic boundary for the neighboring blade passage was constructed by copying the first periodic and rotating the copy by 18 degrees to encapsulate one of the 20 blades. The original and copied surfaces are depicted in Figure 30.

It is at this point in the geometry construction process which the tangential objective of multiple blade passages is addressed. The steps which hereby follow all reference points on either periodic surface, and were all developed with the intention of being robust in regard to future changes. As a result, the copy operation which spawned the complementary periodic surface may interchange the 18 degree rotation with any integer multiple of 18 degrees in order to generate a geometry with multiple blade passages. Beyond this adjustment, no further action is required in order to generate geometry for multiple blade-passages.

Following the copy operation, it became essential to minimize the total number of operations performed to construct the final fluid domain body, as the differential in surface area between the periodic boundaries increased with every operation performed. In order to satisfy the requirements for match control use, the difference in surface area between the two boundaries was kept as small as possible. By minimizing the number of operations between this step and generation of the final volume, the difference in area between the two surfaces was kept below 10^{-6} mm^2, which satisfied the requirements of match control. The finite difference which did exist is believed to be the product of round-off error, error introduced during quadrature calculations for surface area, and other machine-level phenomena beyond the scope of this study.

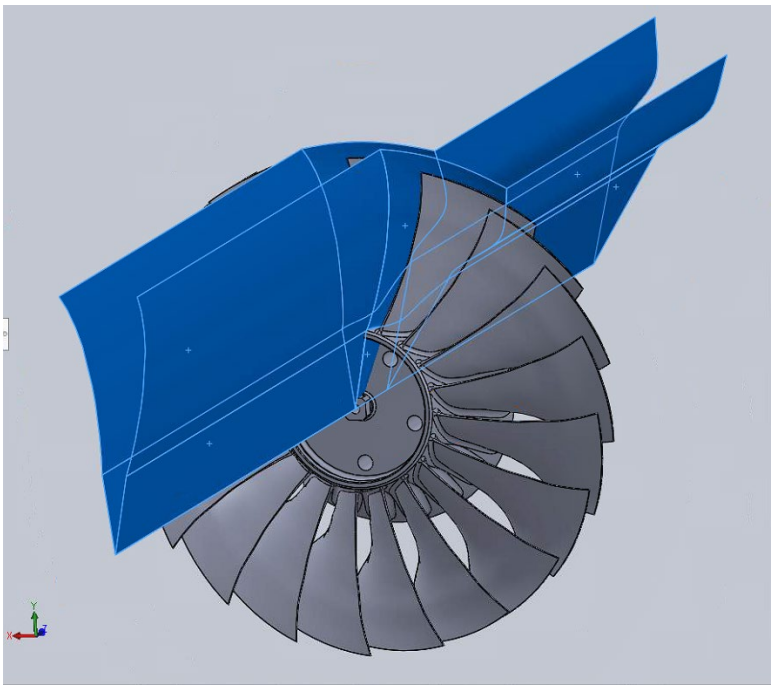

Figure 30. Original and copied periodic boundary surfaces.

Generation of a volume from the surfaces depicted in Figure 30 was accomplished by first drawing 3D sketch arcs connecting the tops of the two surfaces at the inlet and outlet of the passage, as well as the inlet and outlet of the section of the passage immediately adjacent to the blade. A surface was then lofted along the top of the passage through these arcs. The inlet and outlet surfaces were then created by utilizing the surface fill feature on the closed curves encompassing these two regions. With the outer surface, inlet surface, and outlet surface constructed, the fluid domain now consisted of a set of closed surfaces. The surface knit feature was then used to stitch together the closed surfaces and fill the resulting volume to create a solid body. The result of these steps, with the inlet surface, outer surface, and outlet surface highlighted is depicted in Figure 31.

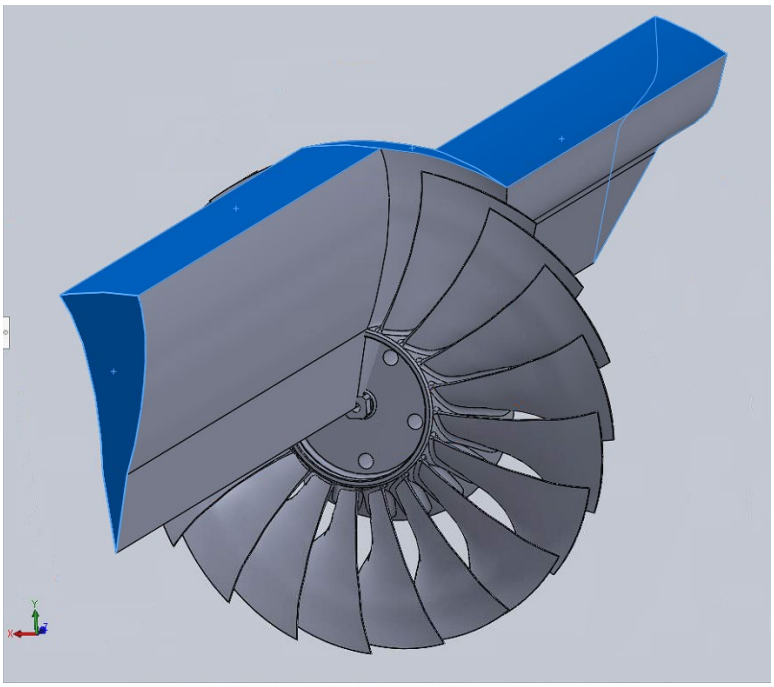

Figure 31. Outer surface, inlet surface, and outlet surface fills.

The components of the TCR assembly were incorporated into the fluid domain geometry by first inserting the geometry depicted in Figure 31 into the existing TCR SolidWorks assembly, and then by subtracting away the TCR components from the fluid domain using the cavity feature. The mating of the fluid domain with the TCR assembly is depicted in Figure 32, and the fluid domain following subtraction of the TCR components is depicted in Figure 33.

The present step, within the context of the overall CFD geometry generation process, is intended to streamline the implementation of future advance casing treatments for the NPSMF. Future casing treatments could be implemented by replacing the existing casing (colored teal in Figure 32) in the TCR assembly with a test article casing, then by repeating the present step using the updated assembly. No further modification to the CFD geometry construction process should be necessary.

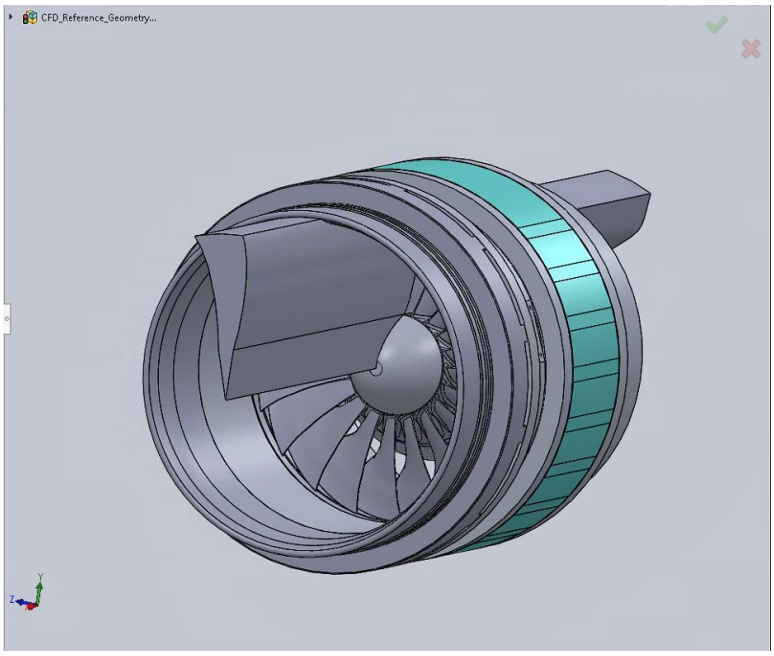

Figure 32. Fluid domain wedge mated with the TCR assembly geometry.

The subtraction operation used to account for the TCR assembly leaves many dangling pieces of geometry surrounding the fluid domain wedge, as well as several notches and extraneous features which make computation more difficult, but do not add value to the flow simulation. These features are visible in Figure 33.

Figure 34 depicts the fluid domain after cleaning up several of the extraneous features and after subtracting the blade from the domain. Subtraction of the blade was performed using the combine feature, with the subtraction option selected.

The fluid domain as depicted in Figure 34 would be ready for sending to ANSYS for meshing and CFD simulation if study of the circumferential groove casing treatment pictured therein were under study. However, the present study addresses the cases of a smooth-wall casing with zero, narrow, and wide tip-gaps. Therefore, additional steps were necessary to construct the desired tip-gaps.

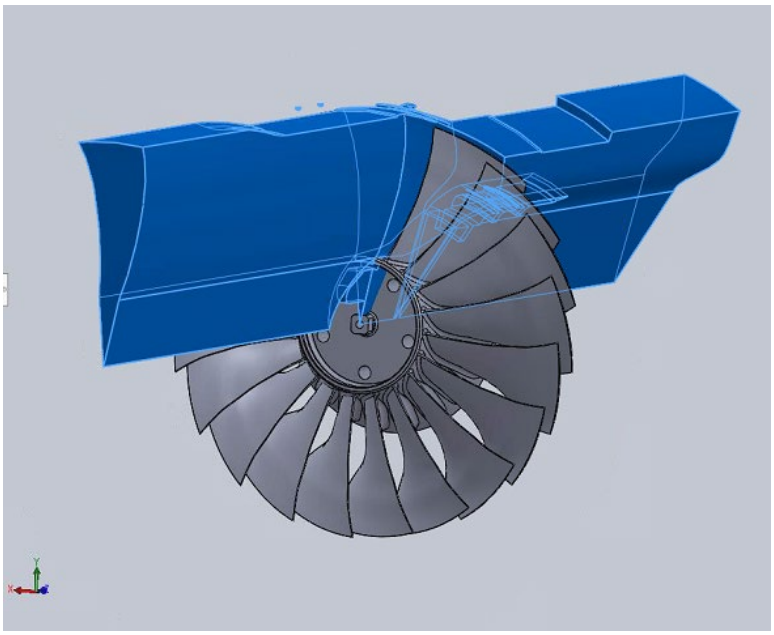

Figure 33. Fluid domain following TCR component subtraction.

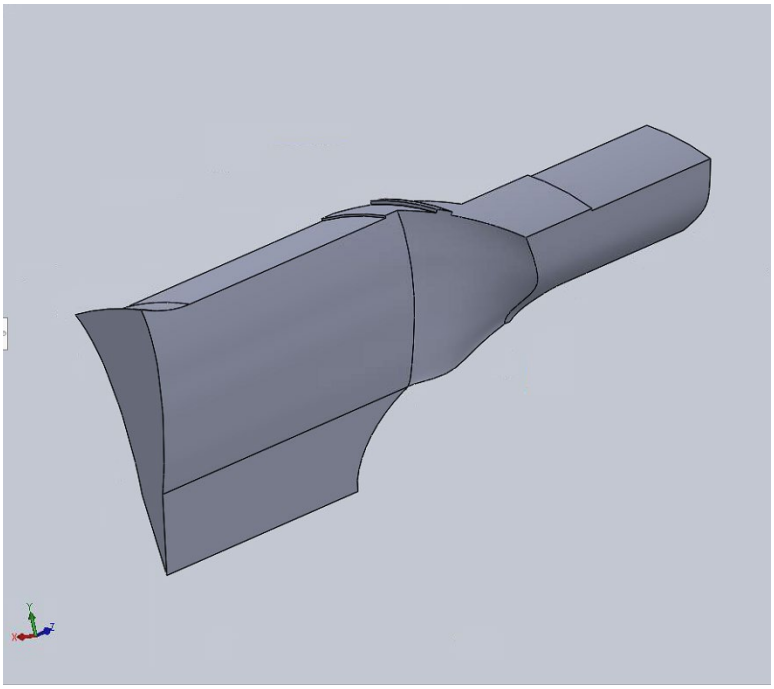

Figure 34. Fluid domain after cleaning up extraneous features and subtracting the rotor.

The final step in construction of the fluid domain was to shave down the upper surface of the body to obtain tip-gaps of the desired dimensions. The desired tip-gap dimensions were zero (0 mm, 0 in), narrow (0.381 mm, 0.015 in) and wide (1.27 mm, 0.050 in). These dimensions represent an ideal case, in which no losses exist due to tip-leakage vortices, a physical TCR casing with the specified narrow tip-gap, and a TCR casing the specified wide tip-gap.

The desired tip-gaps were obtained by first defining a reference plane parallel to the front plane and invoking a section view cut through that plane. A sketch was then placed on the reference plane, and the blade surfaces projected onto the sketch. A line with length equal to the desired tip-gap was then drawn upwards from the blade tip, perpendicular to the blade tip surface. The end of this line was then used to define the radius of a circle which was used as the profile for an extrude cut starting at the sketch plane and extending through the entire geometry in both directions. The section view, projected blade surfaces, and circumscribed circle are depicted in Figure 35.

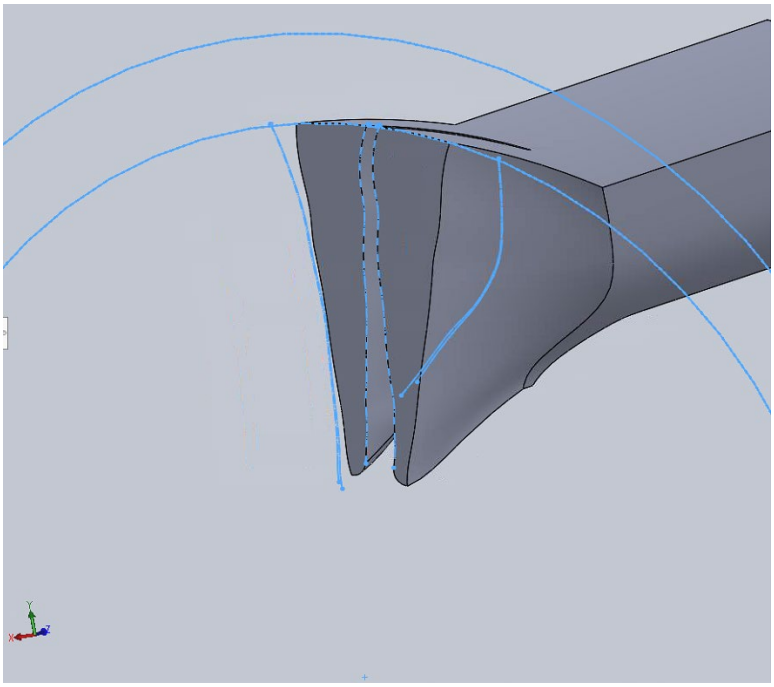

Figure 35. Technique used to construct tip-gaps of desired dimensions.

With the fluid domain now incorporating the desired tip-gap dimensions, the geometry construction was complete and ready for export to ANSYS Workbench for meshing and CFD Simulation.

C. RESULTS

A comparison of the existing geometry (left) and the improved geometry (right) is provided in Figure 36. The improved geometry achieved all of the desired objectives, including the conformal surface capable of match control, the capability to implement advanced casing treatments, and the capability to generate geometries for multiple blade passages.

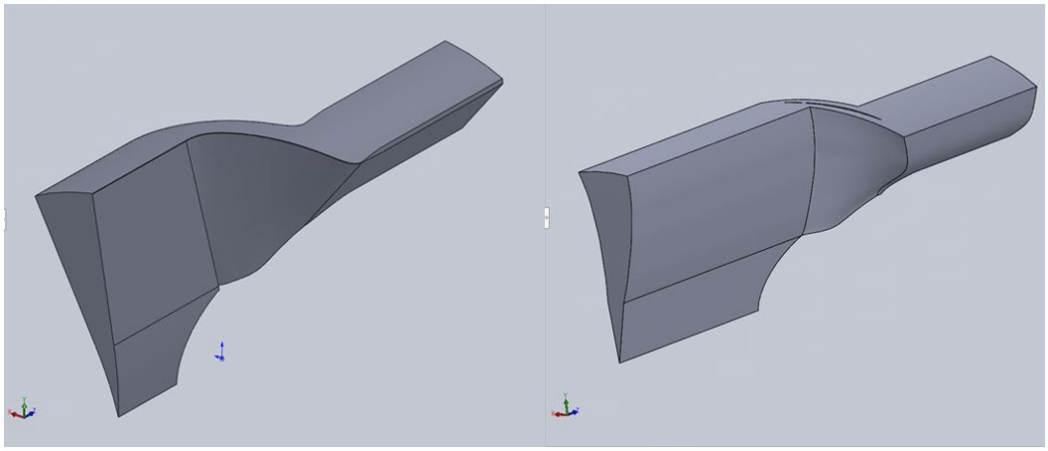

Figure 36. Comparison of existing single-passage geometry (left) to improved single-passage geometry (right).

Figures 37, 38, and 39 depict the completed CFD fluid domain geometry for the zero, narrow, and wide tip-gaps. Figure 40 demonstrates the capability of the aforementioned process to generate a three blade-passage geometry.

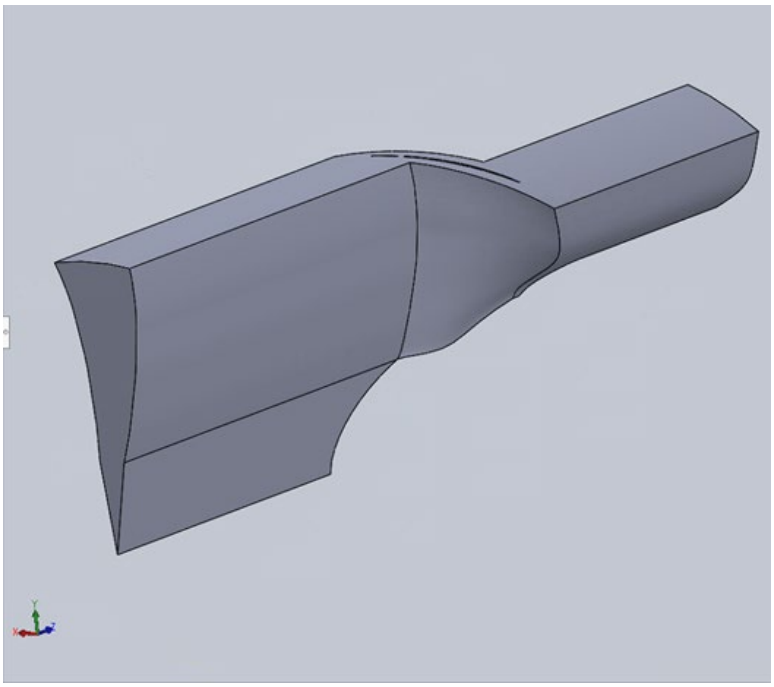

Figure 37. Zero tip-gap single-passage geometry.

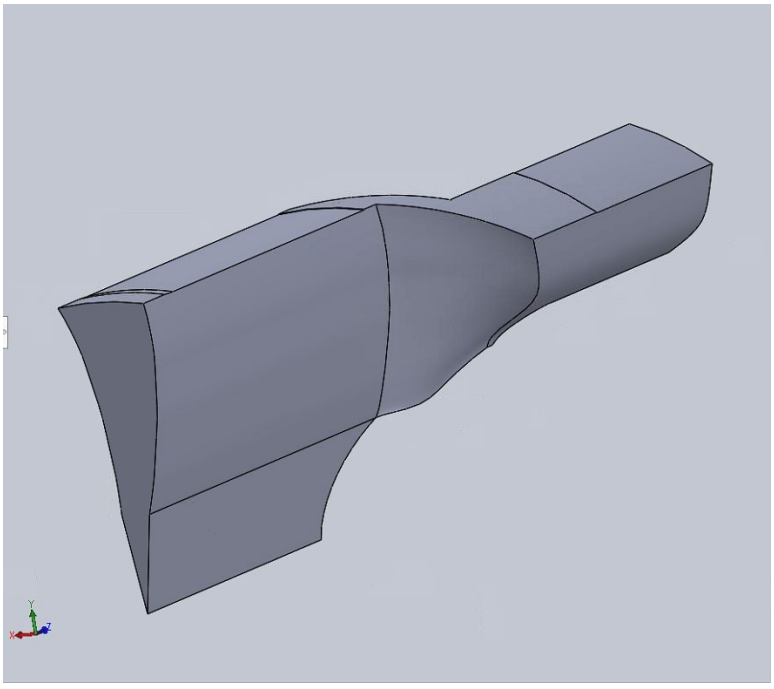

Figure 38. Narrow tip-gap single-passage geometry.

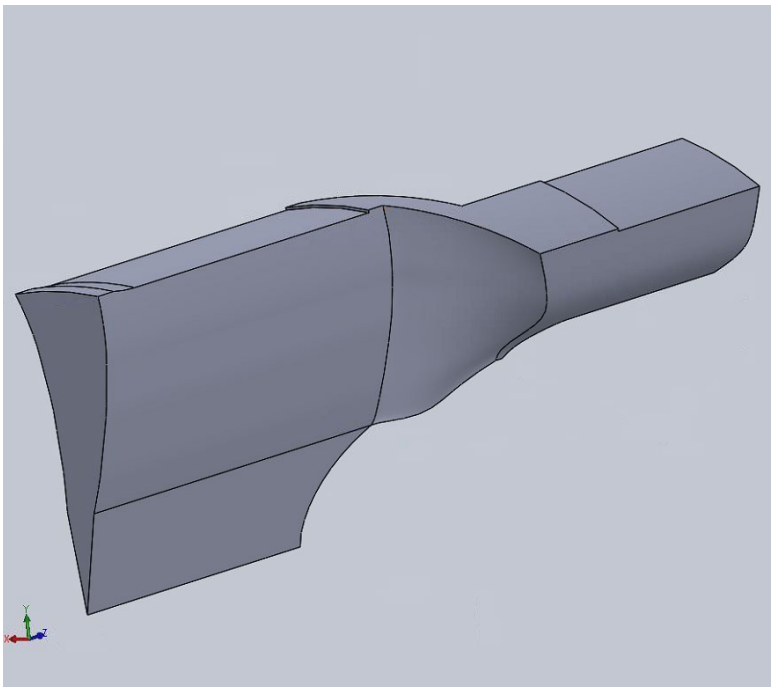

Figure 39. Wide tip-gap single-passage geometry.

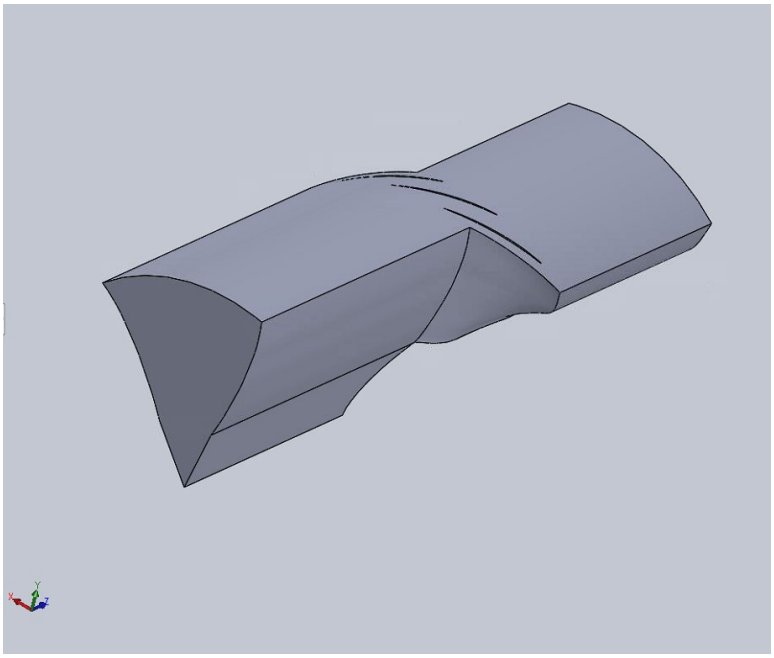

Figure 40. Three blade-passage geometry with zero tip-gap.

THIS PAGE INTENTIONALLY LEFT BLANK

VI. SIMULATIONS USING UPDATED MESH AND GEOMETRY

A. OBJECTIVES

The culmination of the present study was a series of CFD simulations using the improved fluid domain geometries and the improved mesh which simulated flow through the NPSMF along the 90% speed line for the zero, narrow, and wide tip-gap configurations. The experimental data against which the CFD results are compared was introduced in a previous chapter of the present study.

B. SETUP

1. Fluid Domain Geometry

The geometry used for the CFD simulations described in the present section was developed using the process described in the previous chapter. Improvements to the previous geometry incorporated into the new geometry include a true periodic boundary along the axial length of the rotor blade, as well as a framework through which this study may be easily modified and repeated in future work. The fluid domain geometries used in the present set of CFD simulations were depicted in Figures 37, 38, and 39.

2. Mesh

Mesh settings used in the present study were informed by the mesh sensitivity study described in a previous chapter. However, some additional mesh changes were implemented in the present section which constitute further improvement from the mesh sensitivity study. Namely, further refinement of face sizing settings around the leading edge, blade surface, blade fillet surface, and hub surface resulted in inflation layers which uniformly wrapped around the blade leading edge, trailing edge, tip, and hub to a degree which has yet to be obtained by any Turbopropulsion Lab study. Additionally, the bulk mesh size for meshes in the present section was decreased from that which concluded the mesh sensitivity study, in order to better resolve features in the flow field surrounding the blade. A perspective view of the final narrow tip-gap mesh is provided in Figure 41. A top-down cross-sectional view of this mesh is provided in Figure 42, and head-on cross-

sectional views near the blade tip and hub for the narrow tip-gap are provided in Figures 43 through 46.

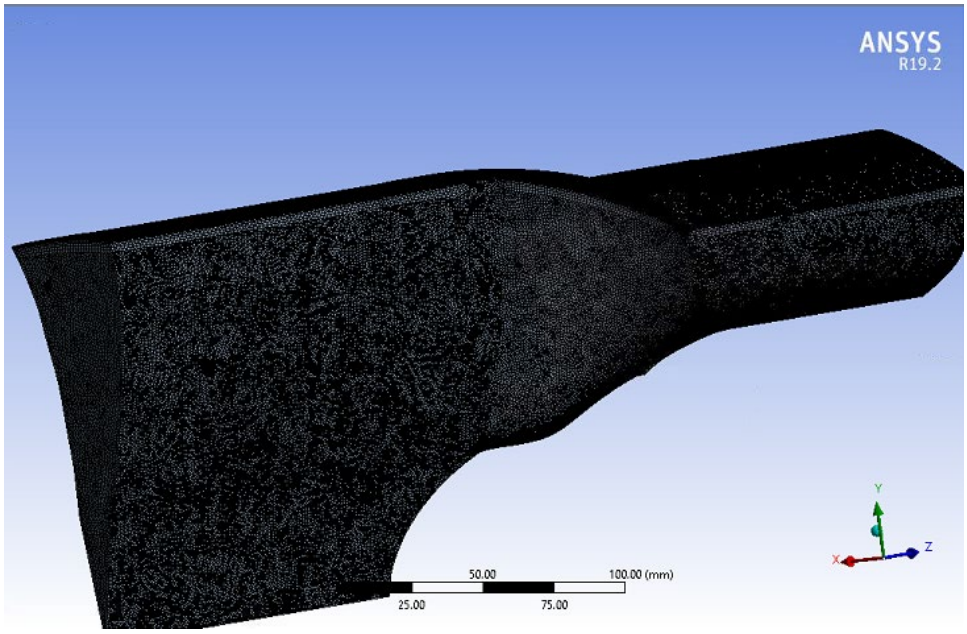

Figure 41. Final narrow tip-gap mesh.

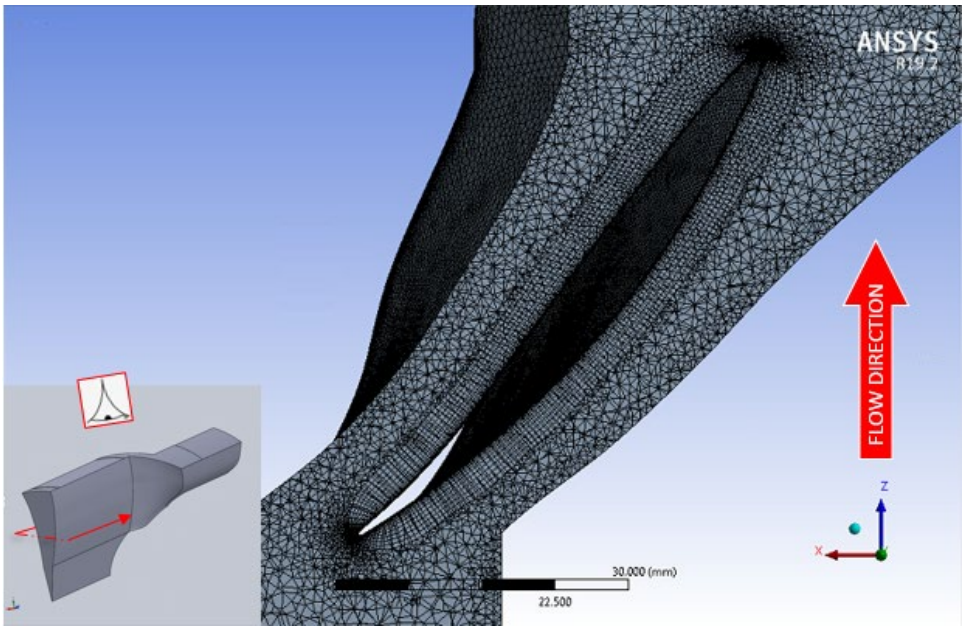

Figure 42. Top-down section view of the narrow tip-gap mesh

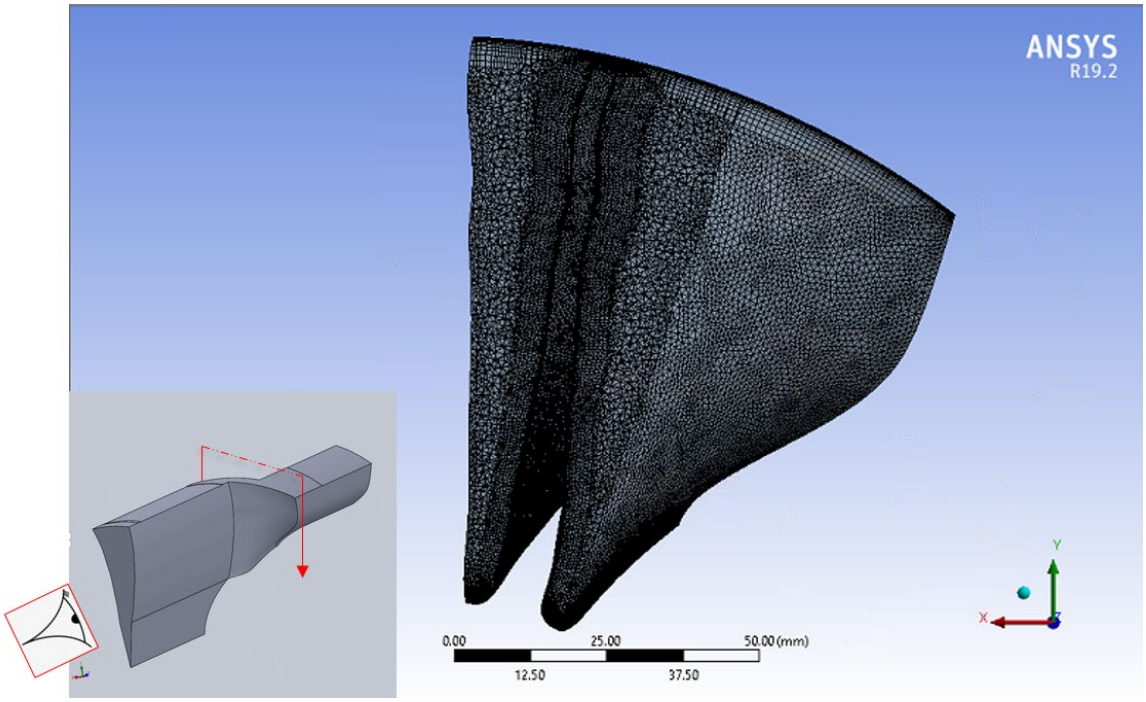

Figure 43. Head-on section view of the narrow tip-gap mesh.

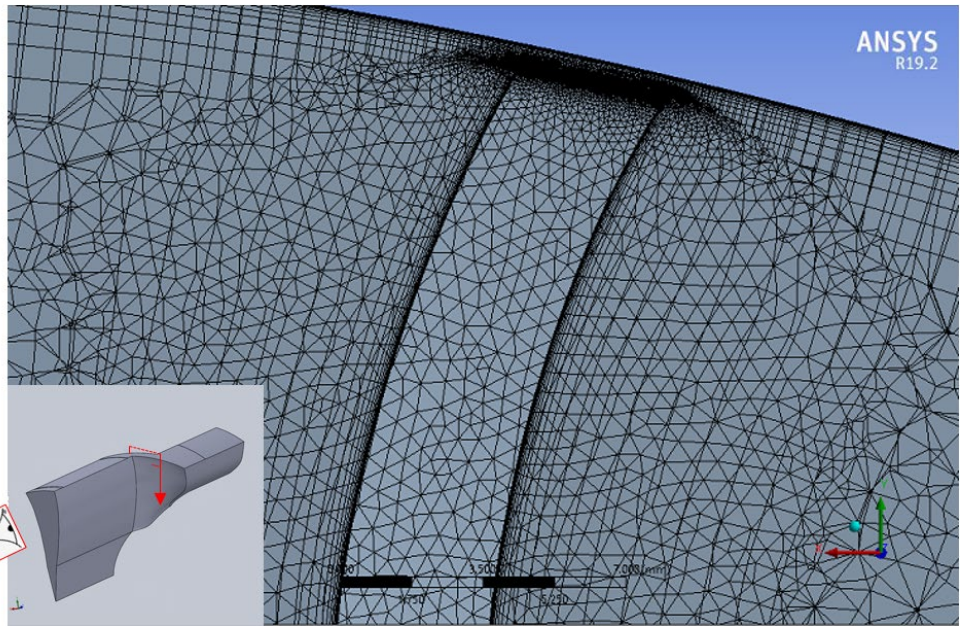

Figure 44. Head-on section view of the narrow tip-gap mesh (blade tip).

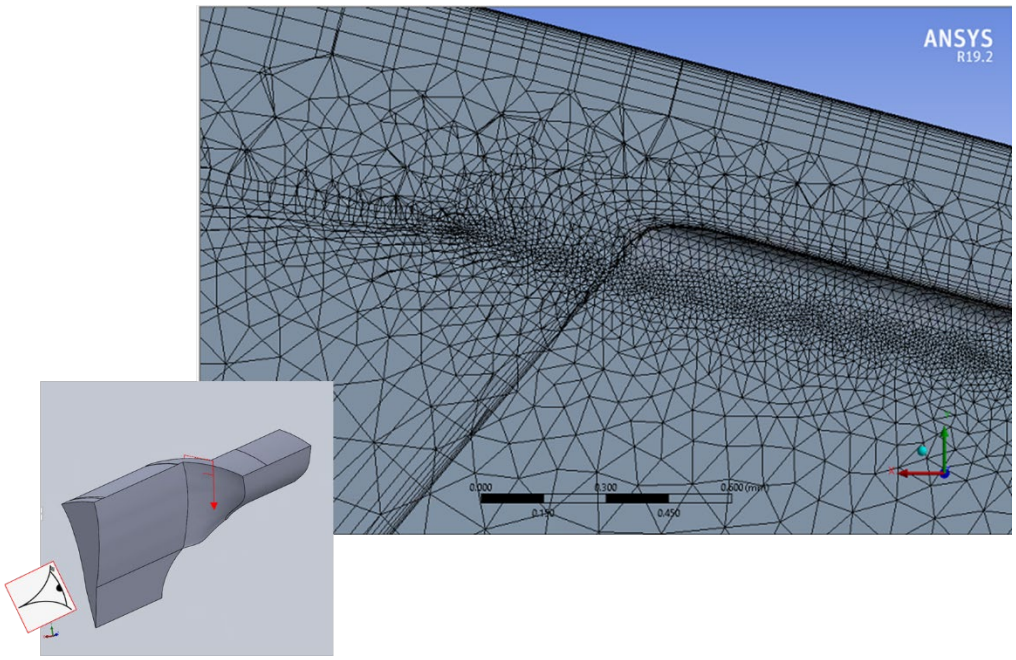

Figure 45. Head-on section view of the narrow tip-gap mesh (blade tip) highlighting the inflation layers wrapping around the blade tip.

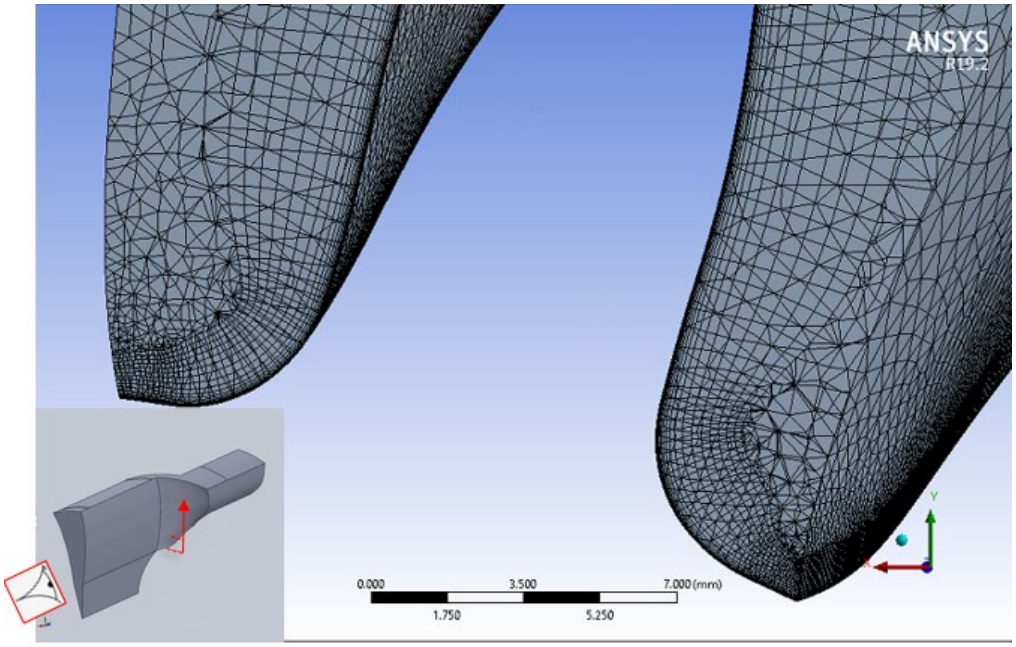

Figure 46. Head-on section view of the narrow tip-gap mesh (blade hub).

Mesh settings for the zero tip-gap and wide tip-gap geometries were identical to those used for the narrow tip-gap, and the qualitative features of those meshes are identical to the features observed in Figures 43 through 46. A summary of the mesh statistics for the zero, narrow, and wide tip-gap meshes is provided in Table 4. The meshes used in the present section are significantly larger than previous meshes used to model the NPSMF. This additional size constitutes a level of refinement which has yet to be applied to the NPSMF. Such refinement only became necessary at the outset of the present study, as the topic of near-stall region simulation in the NPSMF had not been approached in previous work.

Table 4. Summary of mesh statistics for the final improved meshes.

Case	Nodes	Elements	Blade average y^+
Zero tip-gap	4,378,612	11,119,154	0.425584
Narrow tip-gap	10,079,681	23,079,899	0.572413
Wide tip-gap	9,704,525	21,934,163	1.08083

3. CFX-Pre Setup

Inputs passed to the CFX Solver were nearly identical to those passed in the mesh sensitivity study. An example of the CFX-Pre settings used for narrow tip-gap simulations performed for the present section is included as an appendix. The Shear-Stress Transport turbulence model was used, with gamma-theta turbulence transition model. Because the improved fluid domain geometry incorporated match control, the domain interface mesh connection was changed from GGI to 1:1 for the present set of CFX Solver runs. Solver runs were set to conclude if RMS momentum and mass imbalance residuals dipped below $10–^6$, or if the solver reached 1000 outer loop iterations. Most solver runs did not converge beyond $10–^6$. For these cases, the solver was either allowed to complete 1000 iterations or stopped when inspection of the residual monitors and/or performance monitors indicated that steady-state had likely been reached inside the device. However, many of the solutions

obtained displayed oscillating residual behavior after reaching steady-state, which indicates that transient simulations may be necessary to observe some flow features. For this reason, recommendations for future work include investigation of transient simulations for operating points in the near-stall region.

Deterministic selection of boundary conditions is another topic which was left unresolved by the present study. At present, placement of points along each speed line is possible only by iteratively simulating the flow, with adjustments to the boundary conditions between each simulation (a guess-and-check method). Boundary conditions for the present set of CFX Solver runs included depressed relative inlet stagnation pressure (inlet throttling), as in the mesh sensitivity study. The final CFD model was found to be insensitive to small changes in throttle setting away from the near-stall region, and exceptionally sensitive in the near-stall region.

The zero-zero boundary condition (atmospheric inlet stagnation pressure and static back pressure) was again used as a starting point for each speed line, chosen for its flow stability. A first-pass design point sweep was then performed on each speed line (zero, narrow, and wide tip-gap geometries) beginning with inlet throttle increments of 5 kPa (0.725 psi). This initial pass was intended to build the speed line outside of the near-stall region with sufficient detail, while also running as few stalled points as possible. A second pass was then completed using a uniform spread of boundary conditions ranging from the last stable operating point to the first stalled operating point. The first of these runs to stall was then used to inform a third design point sweep using the same approach. While this process was designed for maximum efficiency of design point selection, implementation was complicated by order-of-magnitude changes to the model's sensitivity to boundary conditions approaching stall. As a result of this sensitivity, some clustering appears in the CFD prediction data presented in the following section, at locations where order-of-magnitude changes to the boundary condition stepping increments were not optimally applied.

C. RESULTS

The present section introduces the results gathered during simulations of the NPSMF using the updated CFD model. Important results obtained during this study include:

- Predicted rotor performance for the zero, narrow, and wide tip-gap cases
- Visualizations of the flow field at various locations in the fluid domain for all three cases using contour surfaces and streamlines,
- Identification of flow phenomena with strong explanative power for stall in the NPSMF,
- A case-by-case comparison which succinctly illustrates the effect of tip-gap size on the flow field, and
- A pseudo-transient case which provides some insight into the progression of stall in the NPSMF.

The results presented in this section are novel insofar as previous work has not illustrated the flow field inside the NPSMF during stall. However, it should be remembered that the present study utilized steady-state simulations of a single blade passage to represent near-stall flow through the NPSMF, which is inherently transient and multi-bladed. Nevertheless, results from the present study should provide a useful starting point for future work to address higher-fidelity transient and multi-blade simulations near stall, and inform design of advanced casing treatments for stall margin improvements in the interim.

An important feature used to clarify flow features in the present section is the ANSYS post-processing tool "multiple instancing." Multiple instancing is a copy-and-paste type feature which allows the user to make copies of periodic flows such as the NPSMF single-blade geometry and place them in sequence as they exist in reality. This tool is used to enhance visualization of flow features which cross the periodic boundaries, but does *not* constitute flow simulation of multiple passages.

1. Rotor Performance and Efficiency

Table 5 summarizes the performance and efficiency results for the updated CFD and for the experimental data. Figures 47 and 48 compare the present study's CFD performance and efficiency maps to those gathered during experimental runs of the TCR. The data comparisons pictured in Figures 47 and 48 indicate that the improved CFD model predicts rotor performance and efficiency with a higher fidelity than that obtained in previous studies. However, the CFD-predicted stall point still occurs well before the experimental stall point in all three cases. The source of this discrepancy was not conclusively determined during the course of this study, but further research using transient simulations would be the next logical step from this point.

More generally, the experimental rotor performance falls squarely between the performance predictions of the narrow tip-gap CFD and the zero tip-gap CFD. This discrepancy stems from the deformation of the rotor due to rotational and fluid loading. In the experimental rig, the rotor grows due to rotational loading, causing the tip-gap to decrease from approximately 0.381mm (0.015 in) to 0.178mm (0.007 in) while spinning. This reduction in tip-gap accounts for at least some of the narrow tip-gap CFD's underperformance, and suggests that implementation of a hot-shape geometry into the present CFD model could more closely predict the experimental stall point.

Some additional observations from Figures 46 and 47 are the over-prediction of rotor performance for mass flow rates above 8.75 kg/s, the acute spike in rotor efficiency of the zero tip-gap CFD just after choke, and the extremely early stall point seen in the wide tip-gap CFD. The over-prediction of rotor performance above 8.75 kg/s is a product of the experimental conditions used to operate the TCR, namely that the experimental rig cannot operate at 90% speed in this region due to power limitations, which accounts for the depressed experimental performance compared to the CFD. The acute spike in zero tip-gap efficiency near choke was not investigated as part of this study, but corresponds to a similar spike which has been previously observed in experimental runs of the TCR. Finally, the wide tip-gap geometry operates across a speed line nearly one-fourth the length of the narrow tip-gap speed line, and nearly one-fifth the length of the

zero tip-gap speed line. The results presented later in the present section partially account for this difference, though the exact cause is not conclusively determined.

Table 5. Performance summary for the updated CFD

Case	Mass Flow Rate	Pressure Ratio	Isentropic Efficiency
Zero Tip-Gap CFD	7.626 - 10.043 kg/s	1.443 – 1.691	0.827 – 0.907
Narrow Tip-Gap CFD	8.450 – 10.117 kg/s	1.409 – 1.647	0.856 – 0.899
Narrow Tip-Gap Experiment	7.533 – 9.738 kg/s	1.478 – 1.706	0.811 – 0.896
Wide Tip-Gap CFD	9.548 – 9.866 kg/s	1.439 – 1.505	0.867 – 0.876

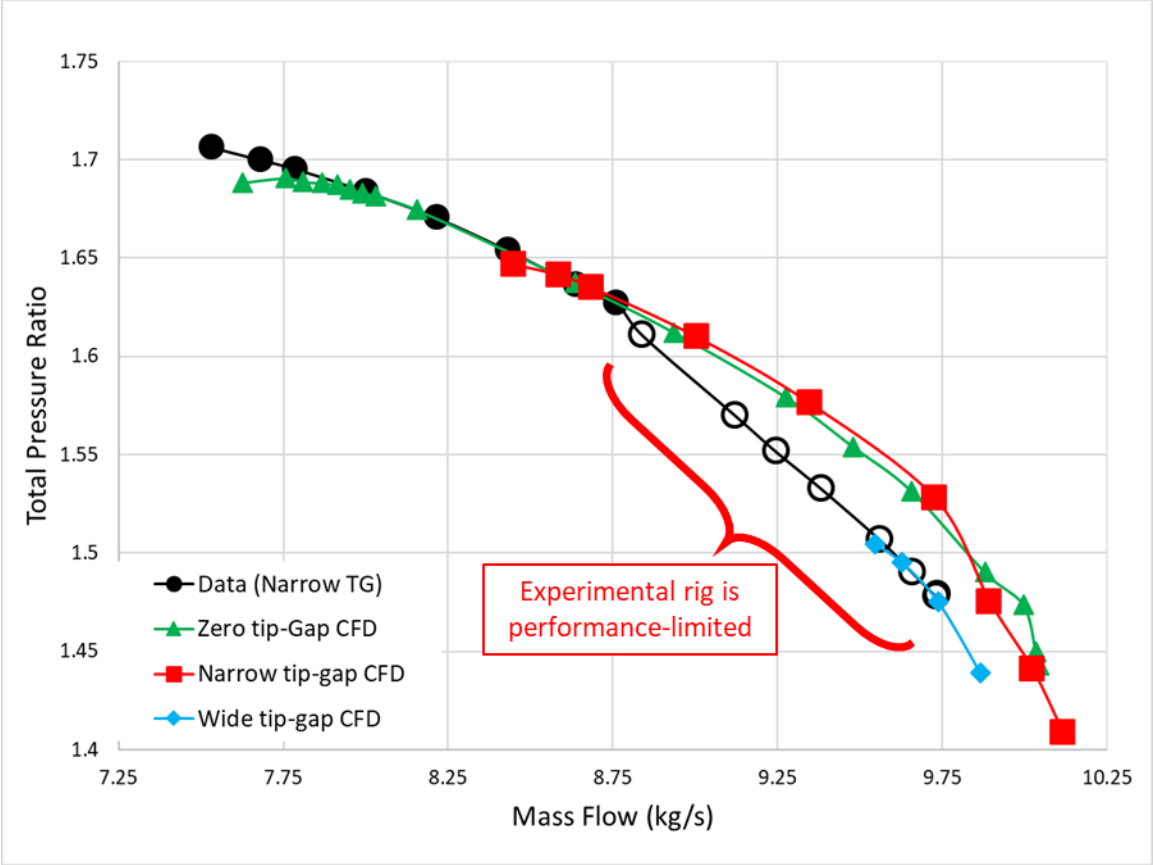

Figure 47. Total pressure ratio map for the updated CFD model.

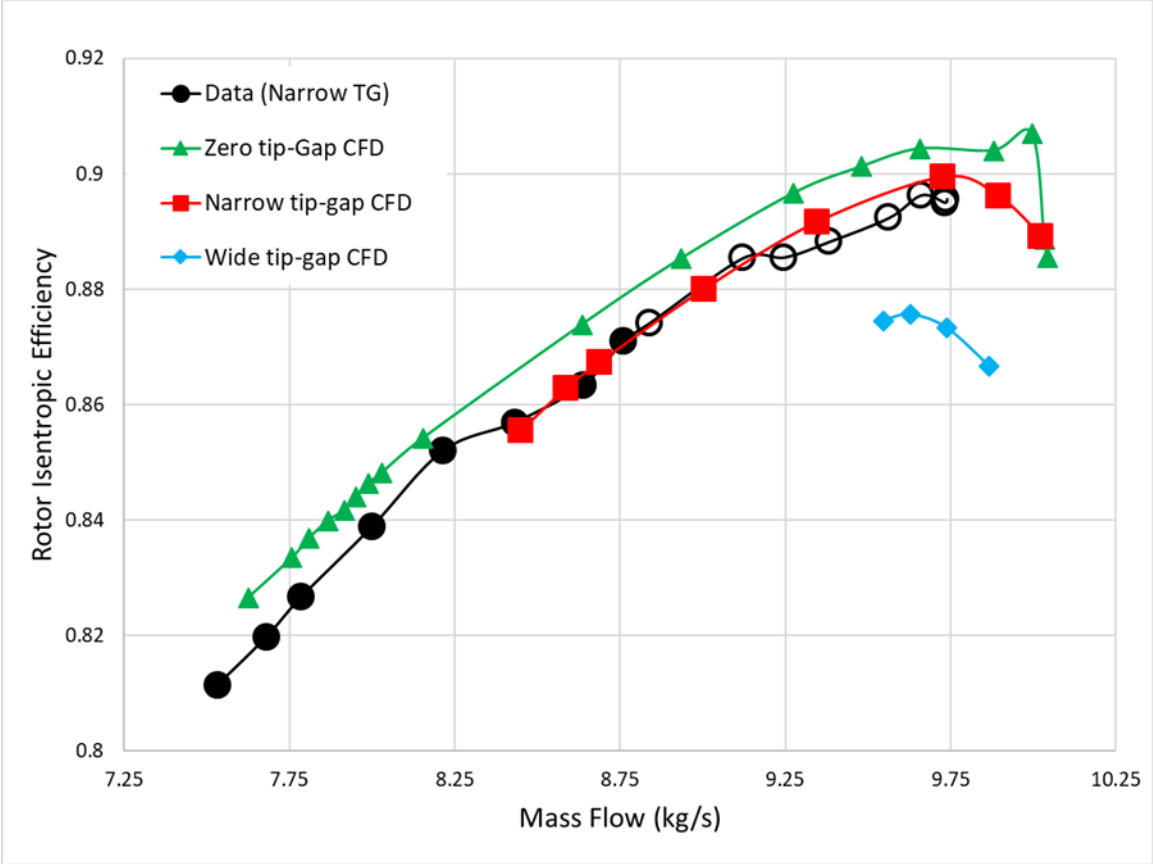

Figure 48. Isentropic efficiency map for the updated CFD model.

2. Narrow Tip-Gap Results

The results obtained from simulations using the narrow tip-gap geometry most closely model the flow through the real rotor, and as such are presented first. These results are presented in Figures 49 through 52 as series of flow field visualizations at either a constant-radius surface at 95% blade span (Figures 49 and 51), on the casing surface (Figure 50), or through the blade passages (Figure 52). The parameters selected for visualization include pressure, Mach number, and streamlines in the relative frame, all of which serve as indicators of flow features such as shocks, expansion fans, and vortices. The dominant flow features observed in the narrow tip-gap flow field include oblique shocks originating from the leading edge, normal shocks in the blade passage, interaction between the oblique and normal shocks, a stand-off bow shock before the leading edge, expansion fans at the trailing edge, vortices originating from the tip of the leading edge,

interaction between these vortices and the standing normal shock at the blade passage entrance, and a large separation bubble just downstream of the leading edge which grows larger as the flow field progresses towards stall. The separation bubble on the leading edge is likely induced by the interaction of the leading edge tip vortex interaction with the leading edge normal shock, and results in effective constriction of the available passage for passing flow through the device. As the passage becomes more restricted, the high-pressure flow from lower in the passage (nearer to the hub) begins circulating upwards into this low pressure region, which marks the onset of stall.

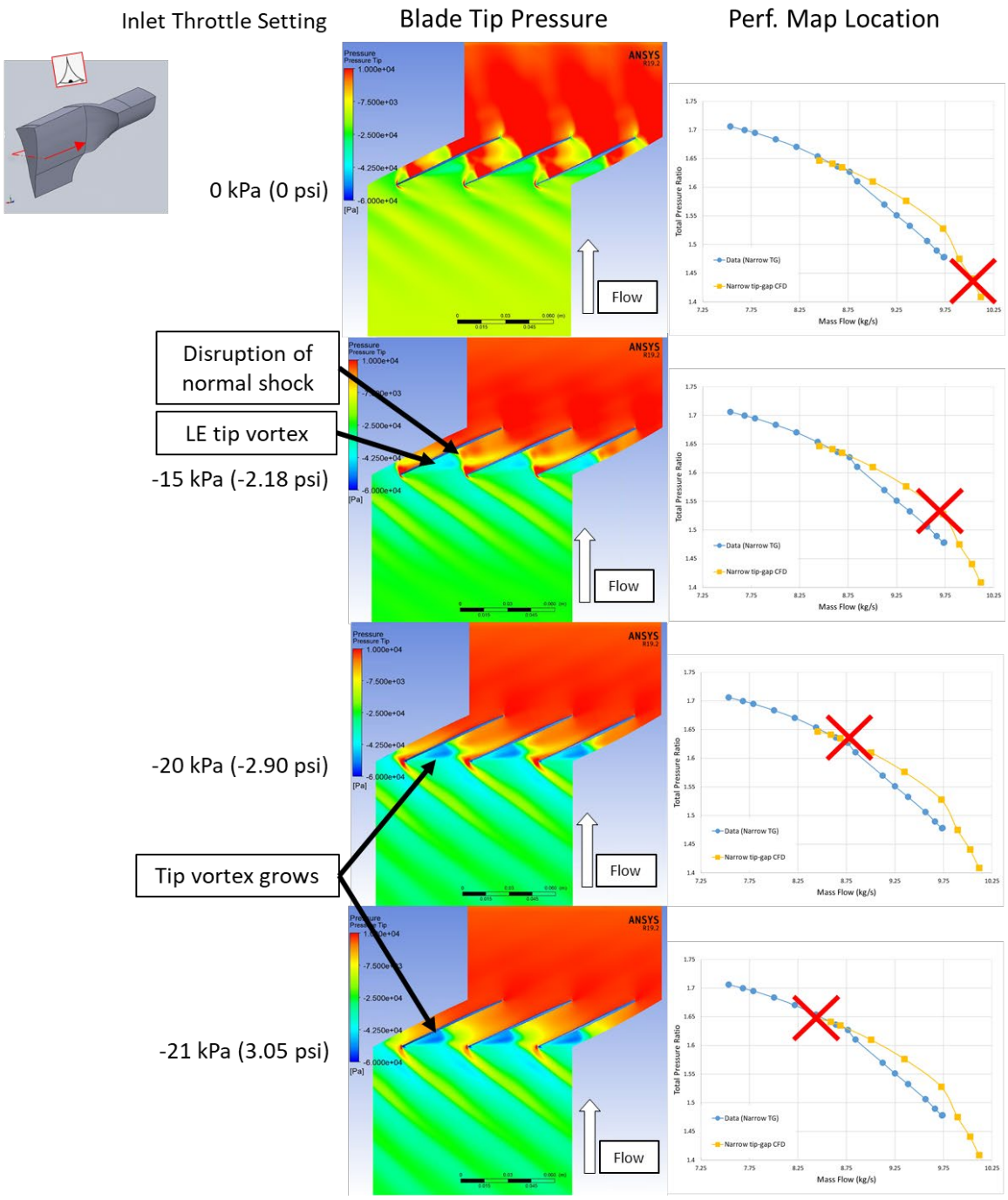

Figure 49. Pressure at 95% blade span progression for the narrow tip-gap case.

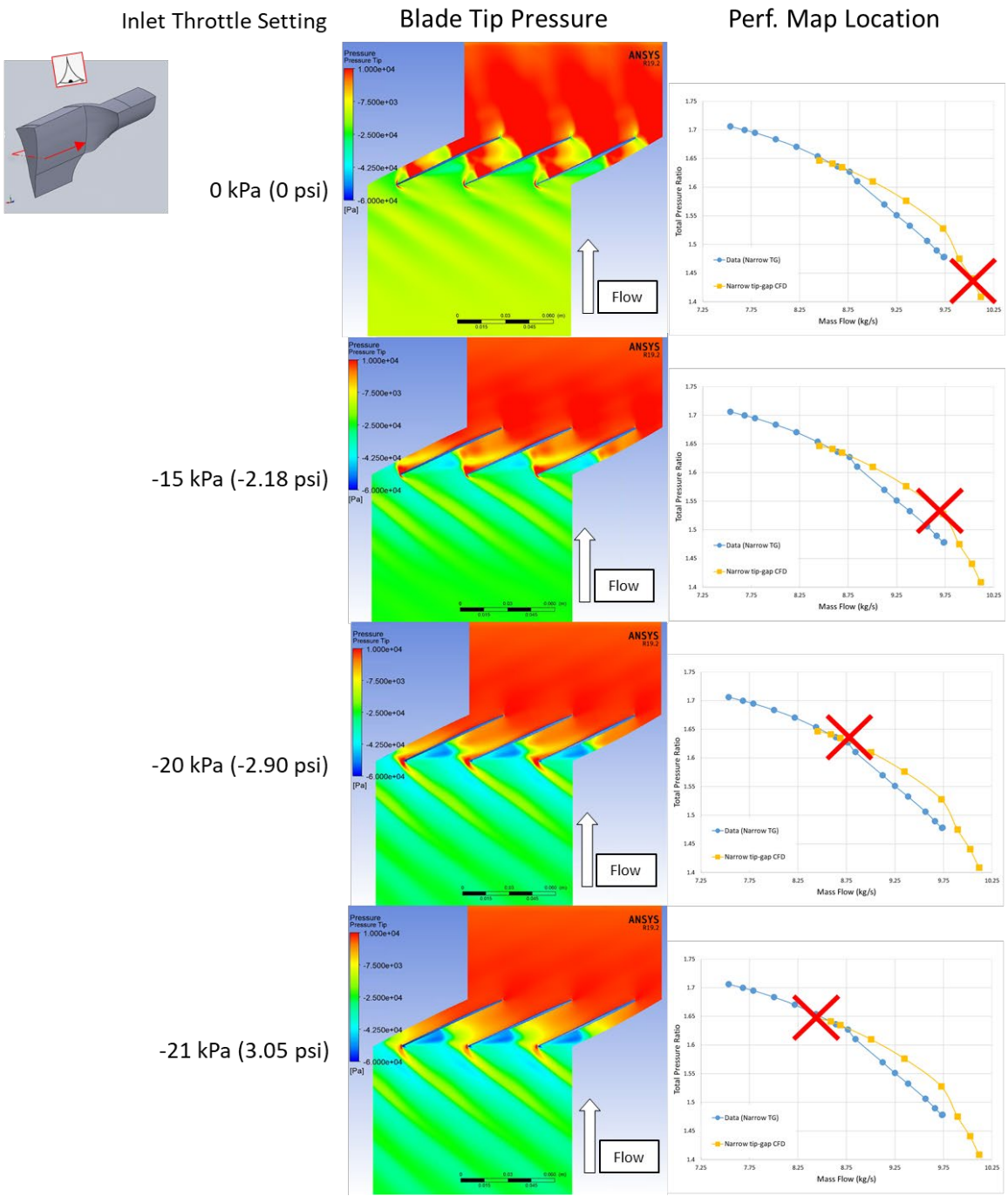

Figure 50. Casing pressure for the narrow tip-gap case.

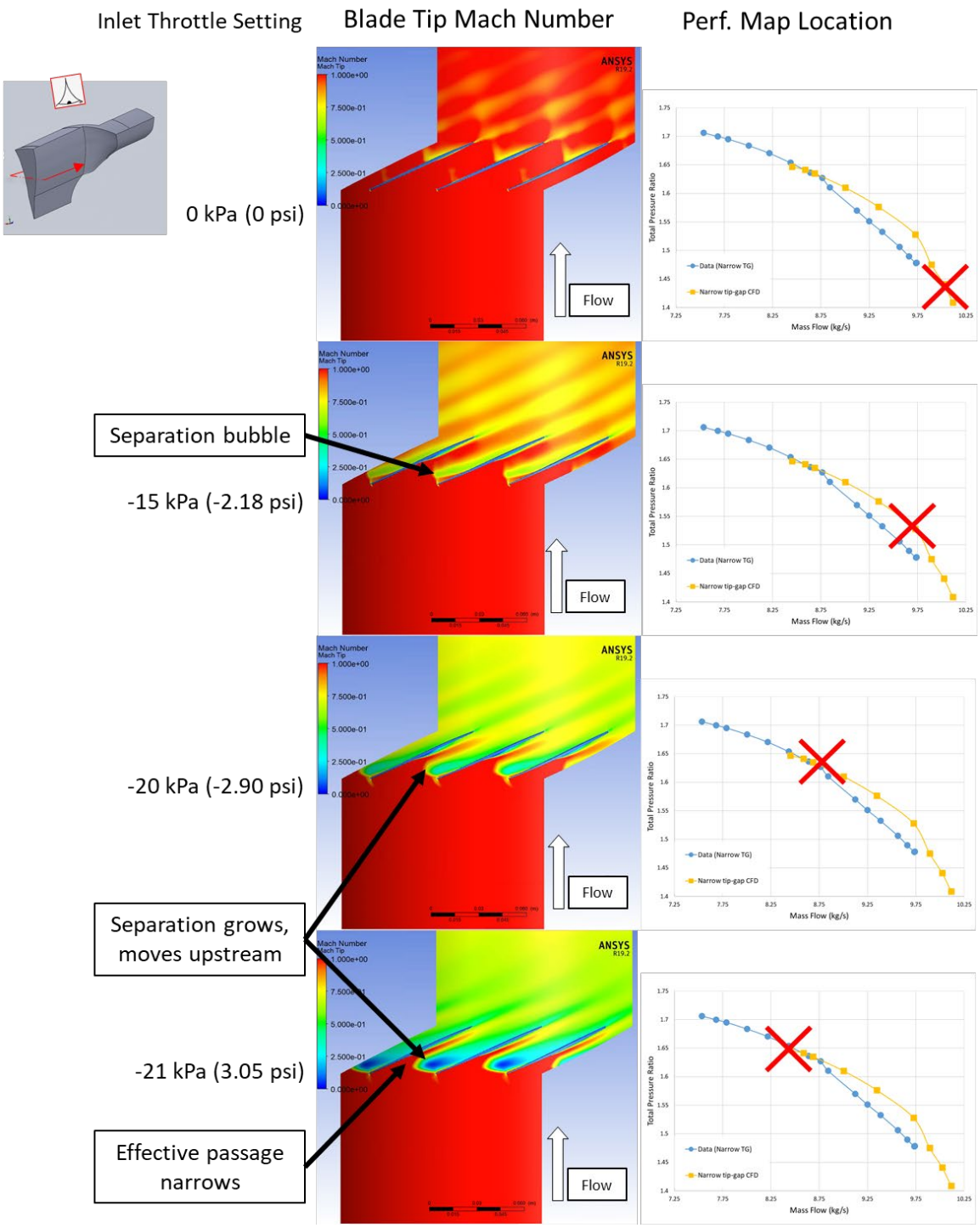

Figure 51. Mach number at 95% blade span progression for the narrow tip-gap case.

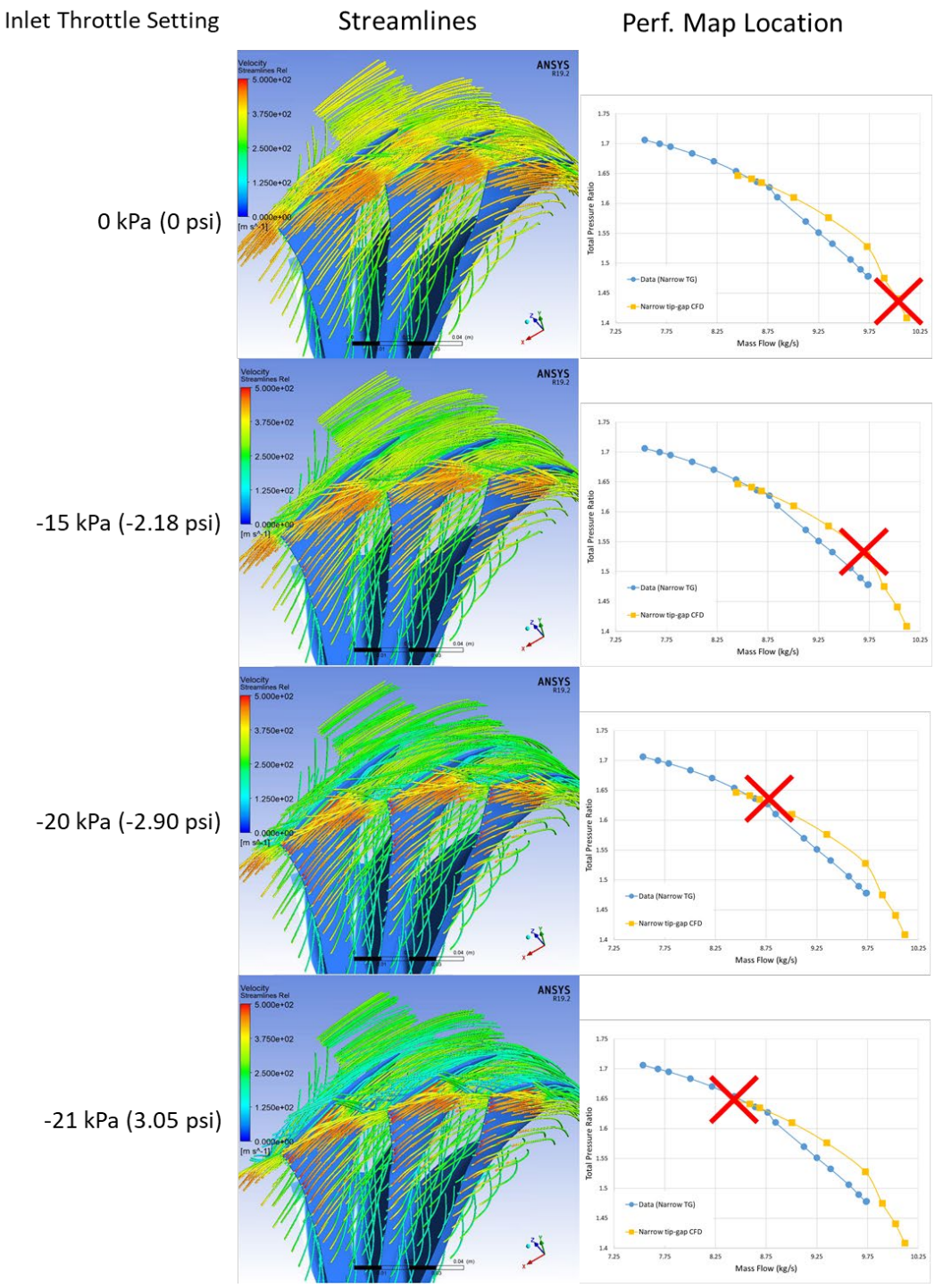

Figure 52. Streamline progression for the narrow tip-gap case.

3. Exit Profiles

An additional performance metric included in the present study is a comparison of pressure and temperature profiles along a radial line downstream of the NPSMF. Such profiles are useful in determining where performance is gained or lost in axial turbomachines such as the NPSMF. CFD evaluation of the pressure and temperature profiles, each normalized to inlet stagnation conditions, was conducted in a similar manner to the experimental determination of exit profiles. A radial probe line was constructed at an axial location in the passage identical to that used in the experimental rig (as shown in the left three images of Figure 54), and the normalized pressure and temperature were sampled and plotted for a finite number of points along the line. This process was conducted for the narrow tip-gap stall point case (orange X in Figure 53). The resulting exit temperature and pressure profiles (Figures 54 and 55, respectively) are then compared to profiles from an experimental point with equivalent mass flow rate (green X) in Figures 54 and 55. A similar comparison is made in Figures 56 and 57, between the zero tip-gap CFD stall point (red X) and the experimental stall point (blue X).

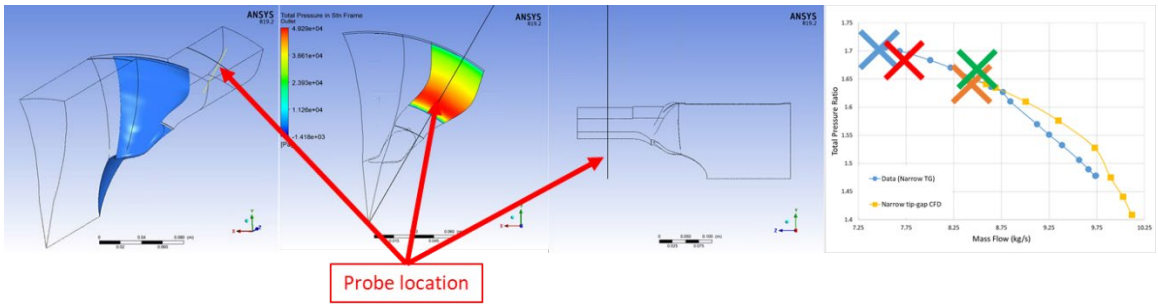

Figure 53. CFD exit profile evaluation setup (left to right: isometric, head-on axial, and circumferential views), and performance map locations of exit profile cases (far right).

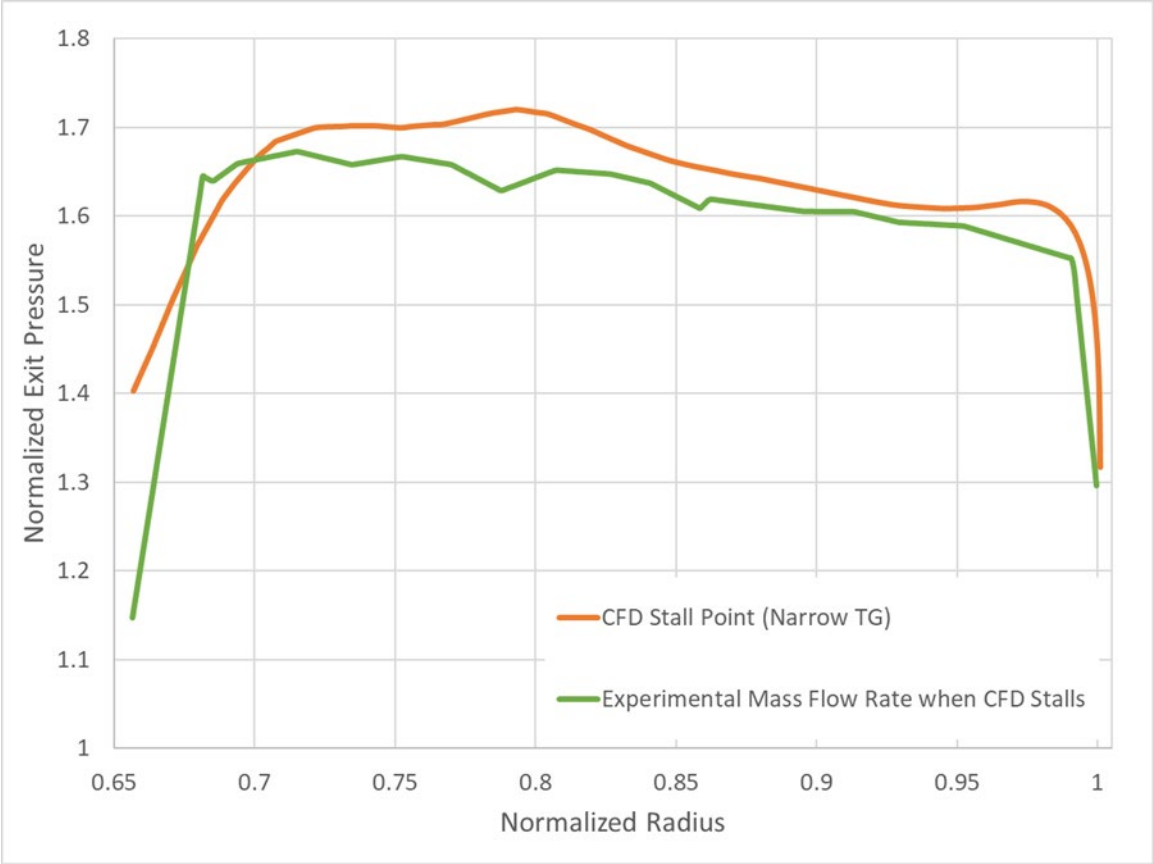

Figure 54. Radial profile of normalized pressure for narrow tip-gap CFD stall and experiment at CFD stall mass flow rate.

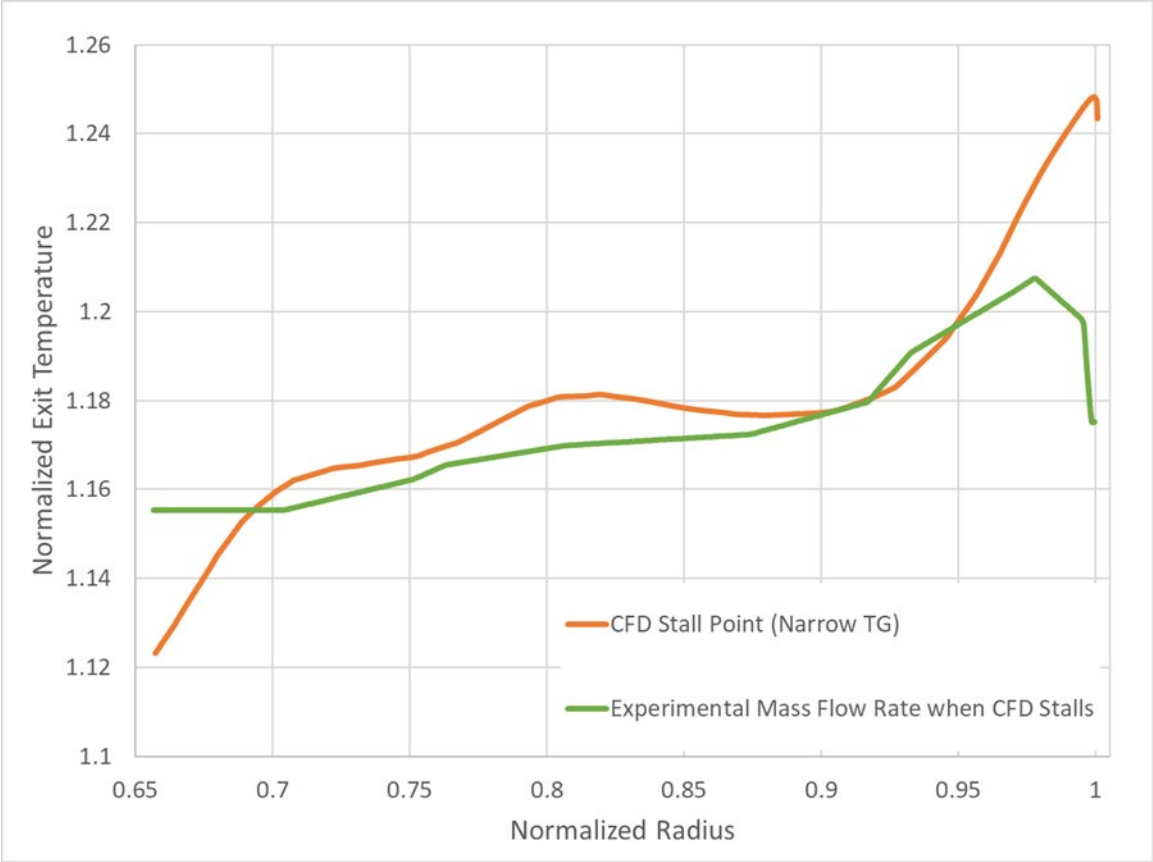

Figure 55. Radial profile of normalized temperature for narrow tip-gap CFD stall, experimental stall, and experiment at CFD stall mass flow rate.

The CFD-predicted exit profile roughly models the behavior of the experimental profile, but does not constitute a faithful representation of the entire flow field. The CFD-prediction of normalized pressure and temperature both profile slightly over-predicts the data from the hub through 95% span, at which point the CFD rises sharply past the data. This difference likely stems from the treatment of the casing as an adiabatic wall. In the exit ducting of the experimental rig, significant heat transfer takes place from the fluid to the casing, as shown by Turner et al. [4], which accounts for the lower experimental exit temperature near the tip shown in Figure 55.

An additional mechanism to account for the difference in exit temperature profiles is the difference in actual tip clearance between the narrow tip-gap CFD model and the experimental rig, whereby the experimental tip-gap decreases from 0.381 mm (0.015 in) to

0.178 mm (0.007 in) while spinning. The smaller experimental tip-gap likely reduces the impact of tip-leakage vortices, which reduces the pressure and temperature near the tip of the experimental rig. No such deformation is represented in the narrow tip-gap CFD model, thus accounting for the over-prediction relative to the experimental data.

The importance of this tip-gap change is supported by Figure 56, in which the exit profile for zero tip-gap CFD stall point closely tracks the experimental stall point exit profile near the blade tip.

An additional observation from Figures 54, 55, and 56 is the difference between CFD prediction and experimental data for exit temperature and pressure near the blade hub. Figures 54 and 56 show that the CFD over-predicts normalized exit pressure near the hub, and Figure 55 shows that the CFD under-predicts the normalized exit temperature near the hub. This difference is likely due to the lack of rotor-rig cavity simulation in the CFD model. The effects of modelling the rotor-rig cavity have previously been shown by Denton [16].

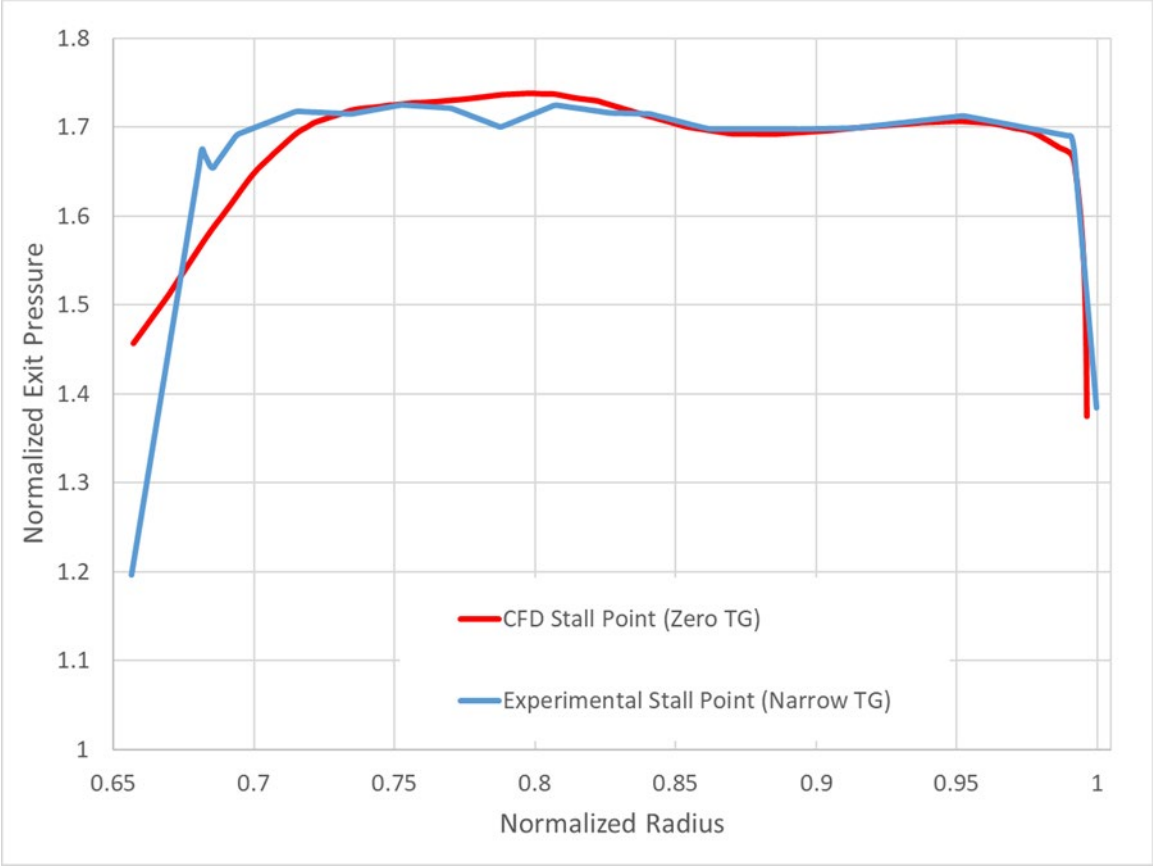

Figure 56. Radial profile of normalized pressure for zero tip-gap CFD stall and experiment at stall.

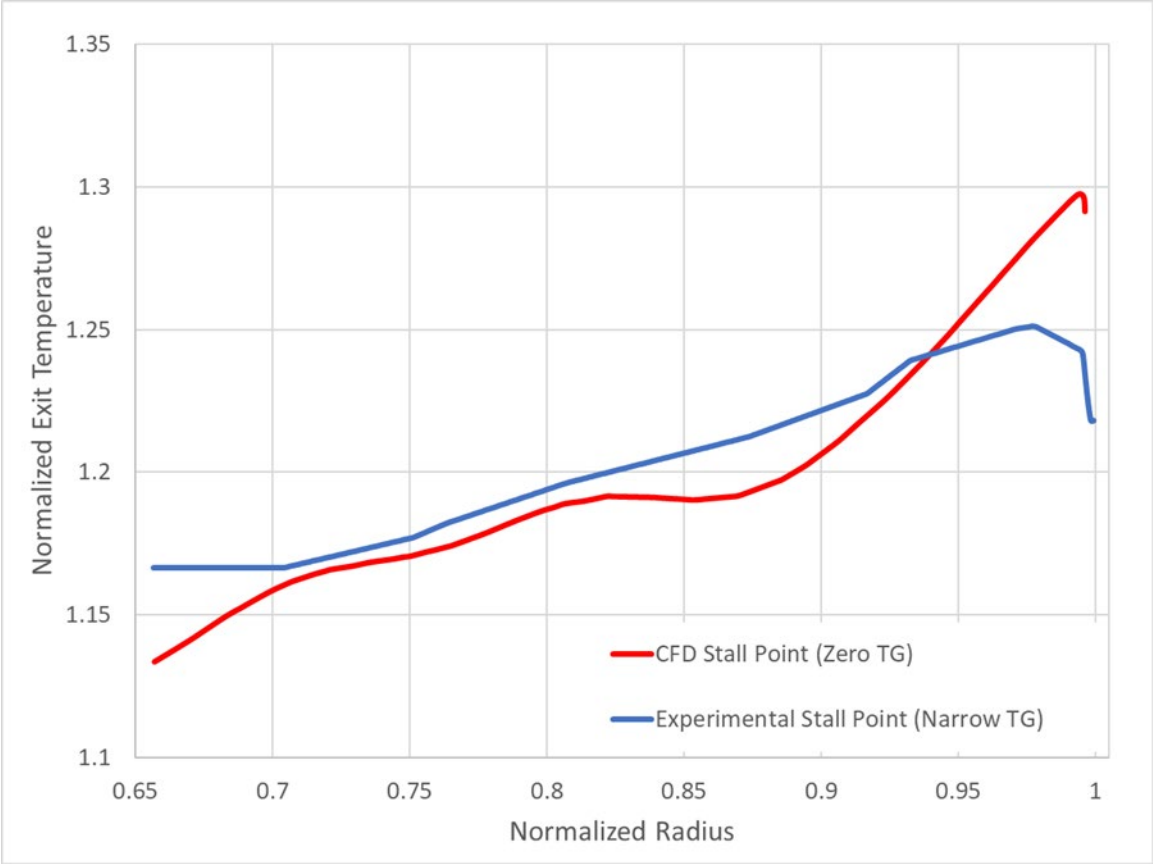

Figure 57. Radial profile of normalized temperature for zero tip-gap CFD stall and experiment at stall.

4. Zero Tip-Gap Results

The results obtained during flow simulations using the zero tip-gap geometry do not represent flow through any real device, and are thus provided as support for conclusions drawn from the narrow tip-gap CFD predictions. These results are provided in Figures 58 through 61. The results are presented as series of flow field visualizations, using the same techniques used to visualize the narrow tip-gap flow field. The dominant flow features depicted in Figures 58 through 61 include oblique shocks originating from the blade leading edge, a stand-off bow shock before the leading edge, normal shocks inside the blade passage which move upstream as the flow progresses, interactions between the oblique shock and normal shock inside the passage, and a separated flow region which starts near the trailing edge and gradually moves forward. A comparison of the zero tip-

gap flow field to the narrow and wide tip-gap flow fields is provided in a later section of the present chapter.

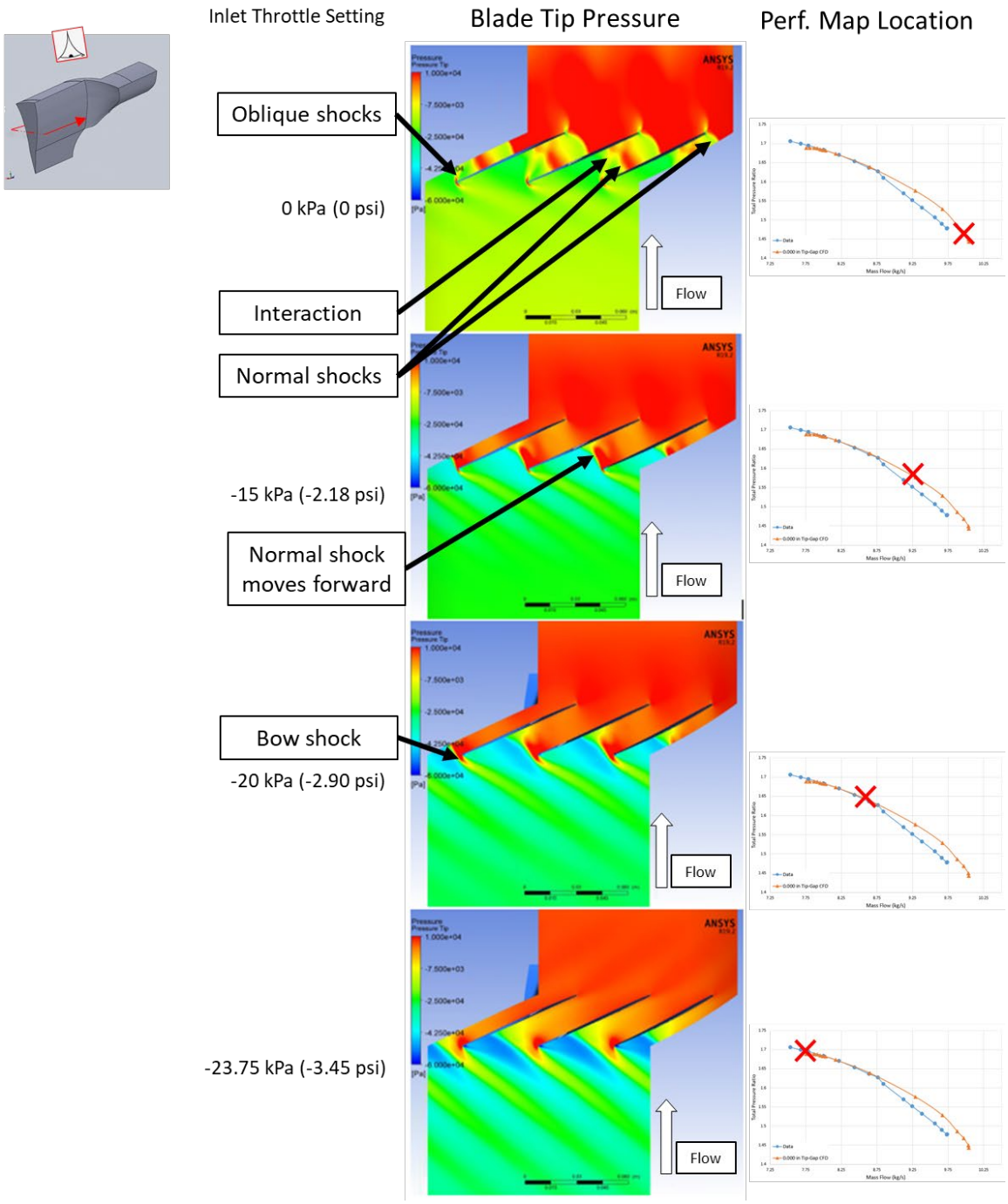

Figure 58. Pressure at 95% blade span progression for the zero tip-gap case.

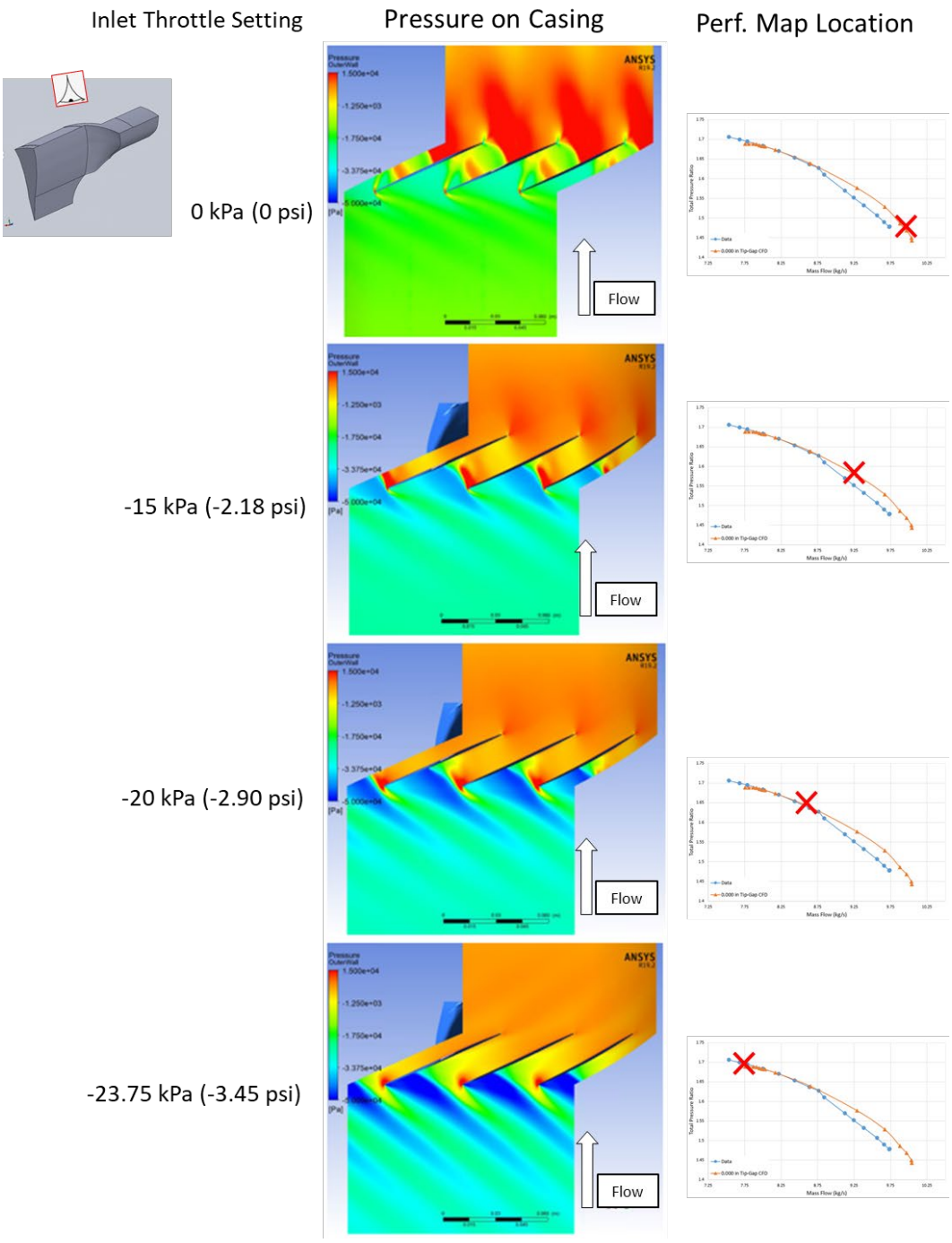

Figure 59. Casing pressure development for the zero tip-gap geometry.

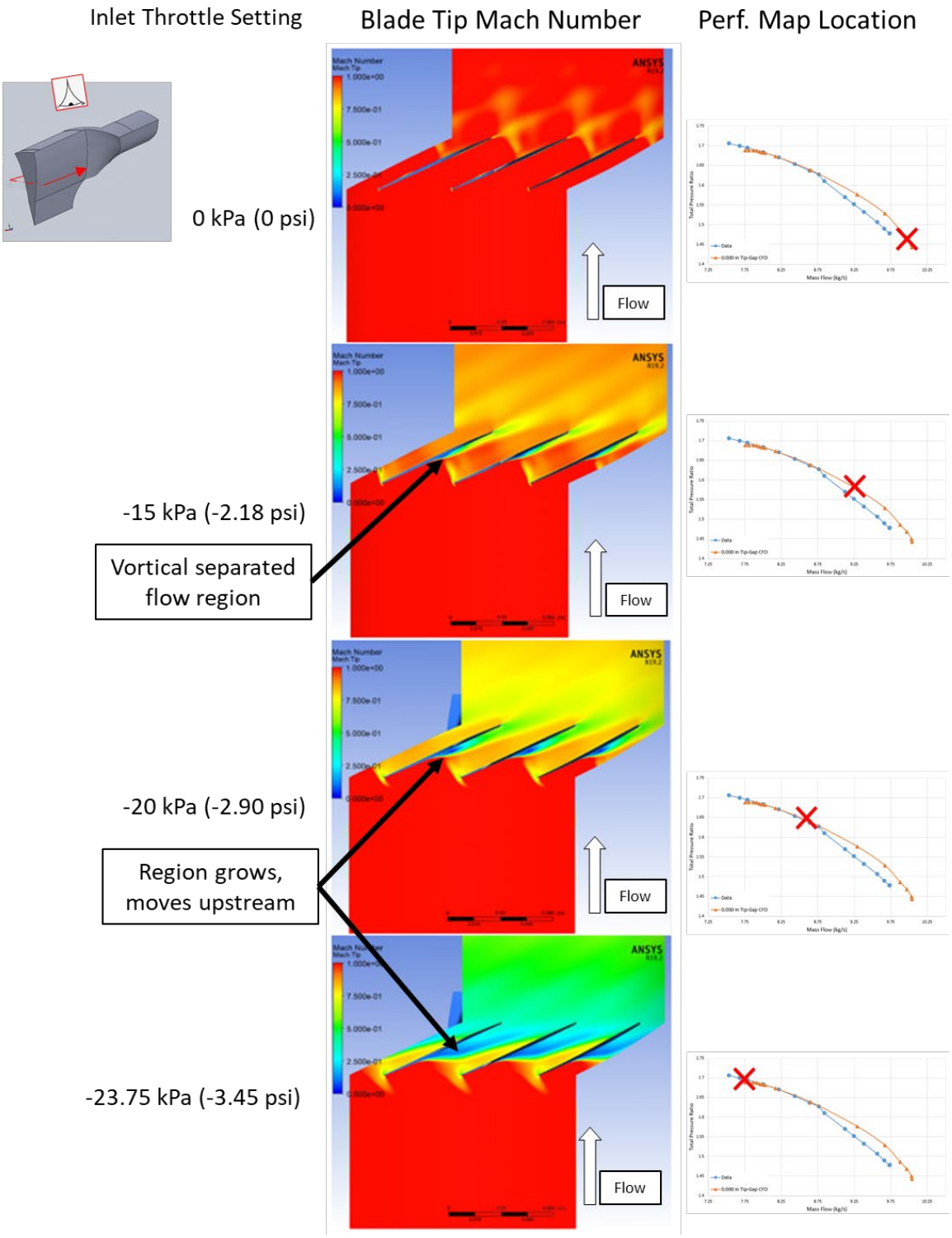

Figure 60. Mach number at 95% blade span progression for the zero tip-gap case.

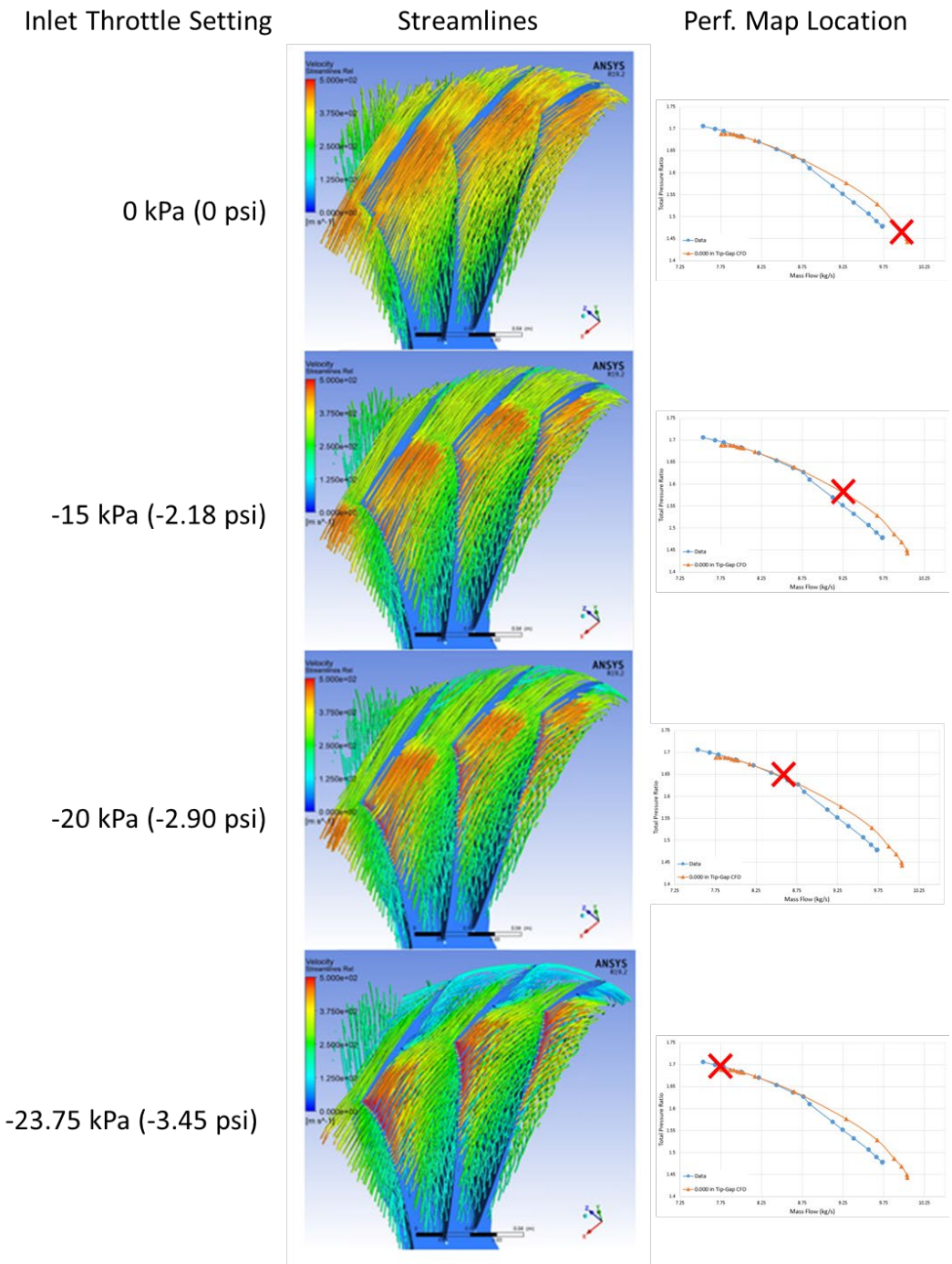

Figure 61. Streamlines progression for the zero tip-gap case

5. Wide Tip-Gap Results

The results for the wide tip-gap case simulations represent the flow through a real device (the wide tip-gap TCR casing). However, flow through this casing grossly underperforms flow through the narrow tip-gap casing, and as such the wide tip-gap case does not represent a practical flow such as that through the narrow tip-gap casing. The wide tip-gap results are thus useful for comparison against the narrow tip-gap results in order to illustrate in an exaggerated fashion the tip-gap's effects on the flow field. These results are provided in Figures 62 through 65. Only four operating points were run with the wide tip-gap geometry, as this case was found to be substantially more sensitive to boundary condition changes than the zero and narrow tip-gap cases. This difference stems from the wide tip-gap geometry's inherent inefficiency, whose mechanism is large leading edge vortices and tip leakage vortices. These large vortices are pictured in Figures 62 through 65, and result in remarkably complex flow fields. The leading edge tip vortex dominates the flow field across the entire operating line, causing drastic changes to the flow field when compared to the narrow tip-gap case. These changes begin with the leading edge tip vortex interaction with the standing normal shock at the passage entrance, and propagate downstream as indicated in the figures. The end product is a pressure gradient parallel to the flow direction, which in turn causes the strong vortex structure which impinges on the suction side of the blade and does not dissipate in the downstream direction as vortices in the narrow and zero tip-gap cases do.

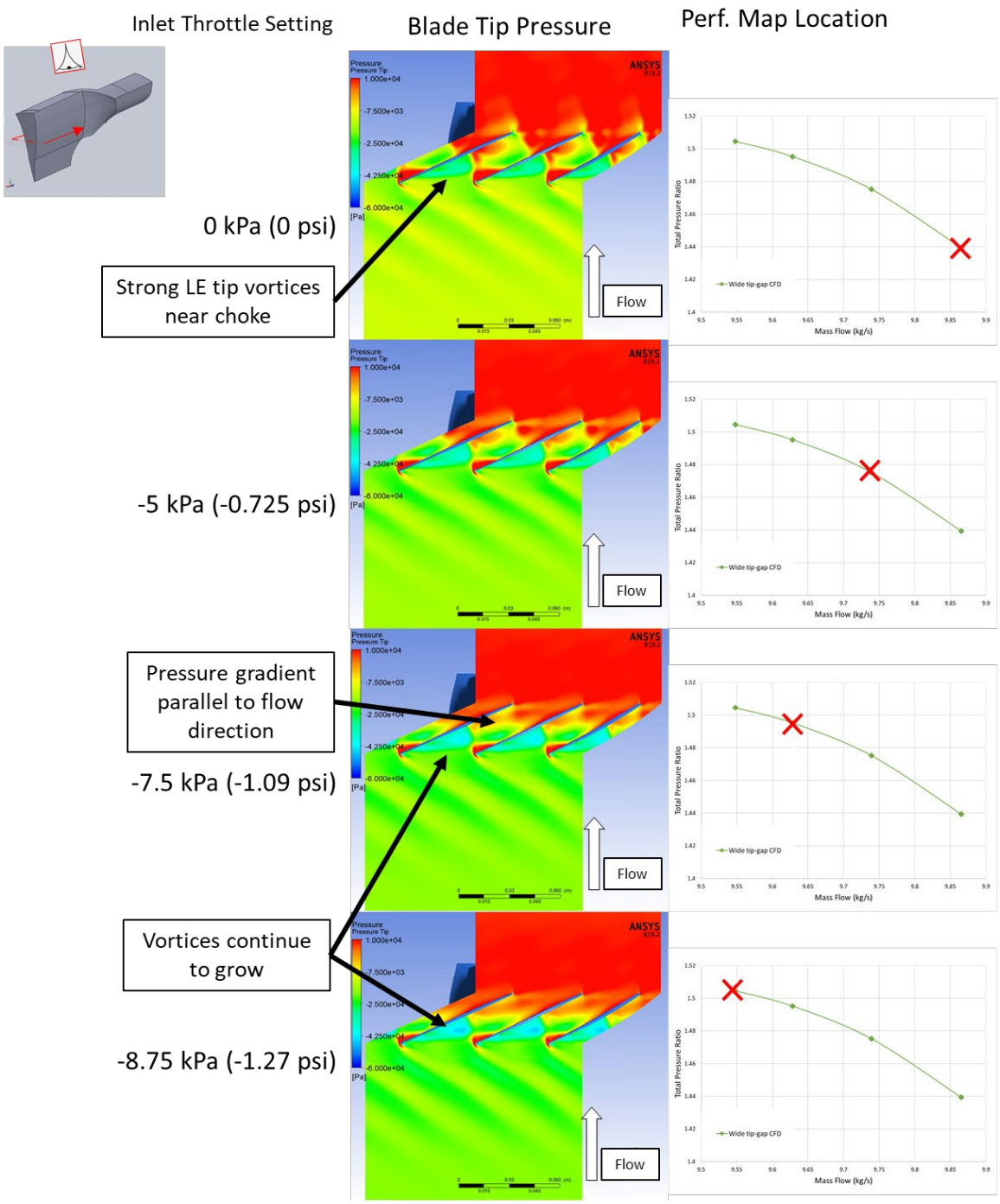

Figure 62. Pressure at 95% blade span progression for the wide tip-gap case.

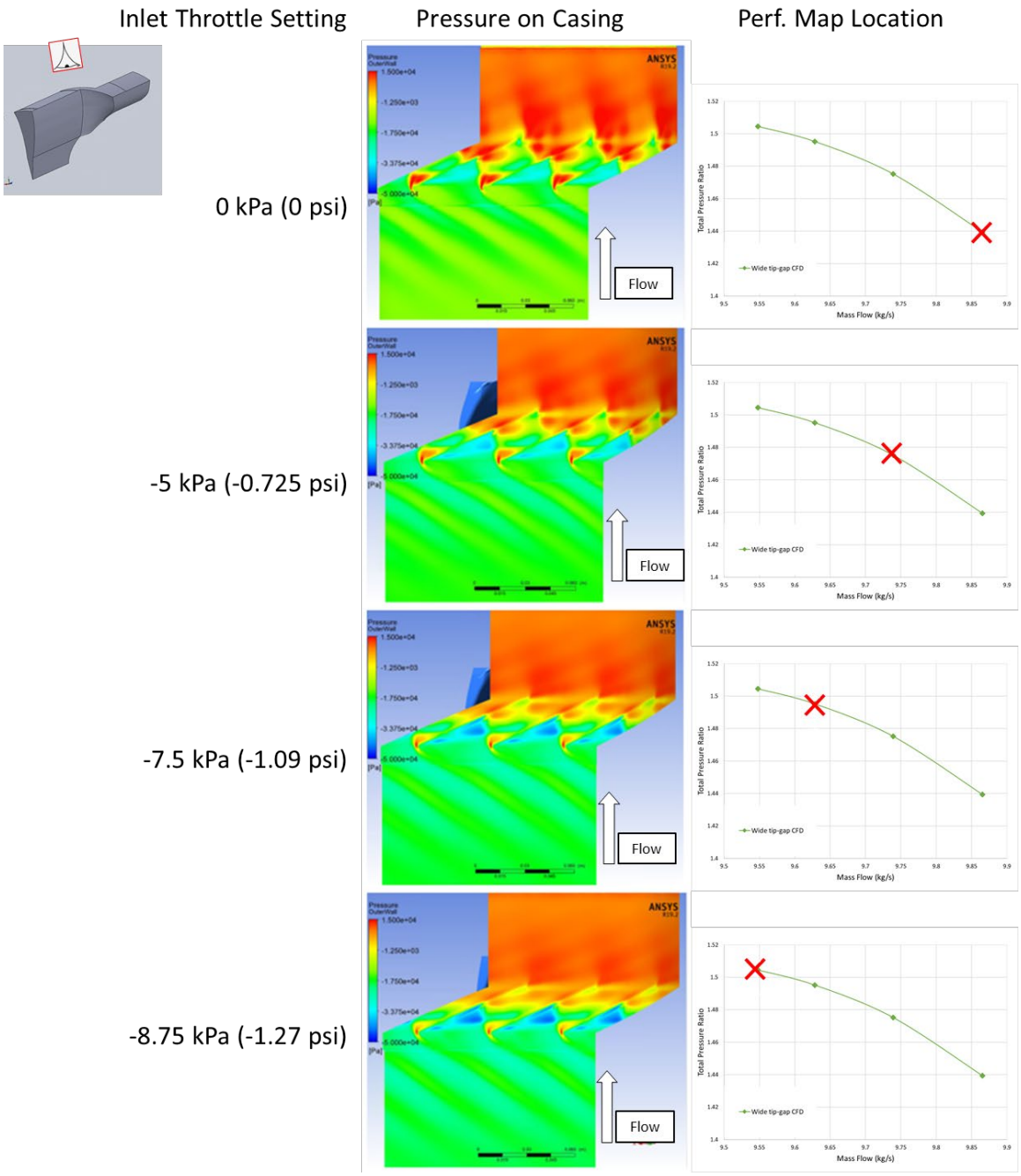

Figure 63. Casing pressure progression for the wide tip-gap case.

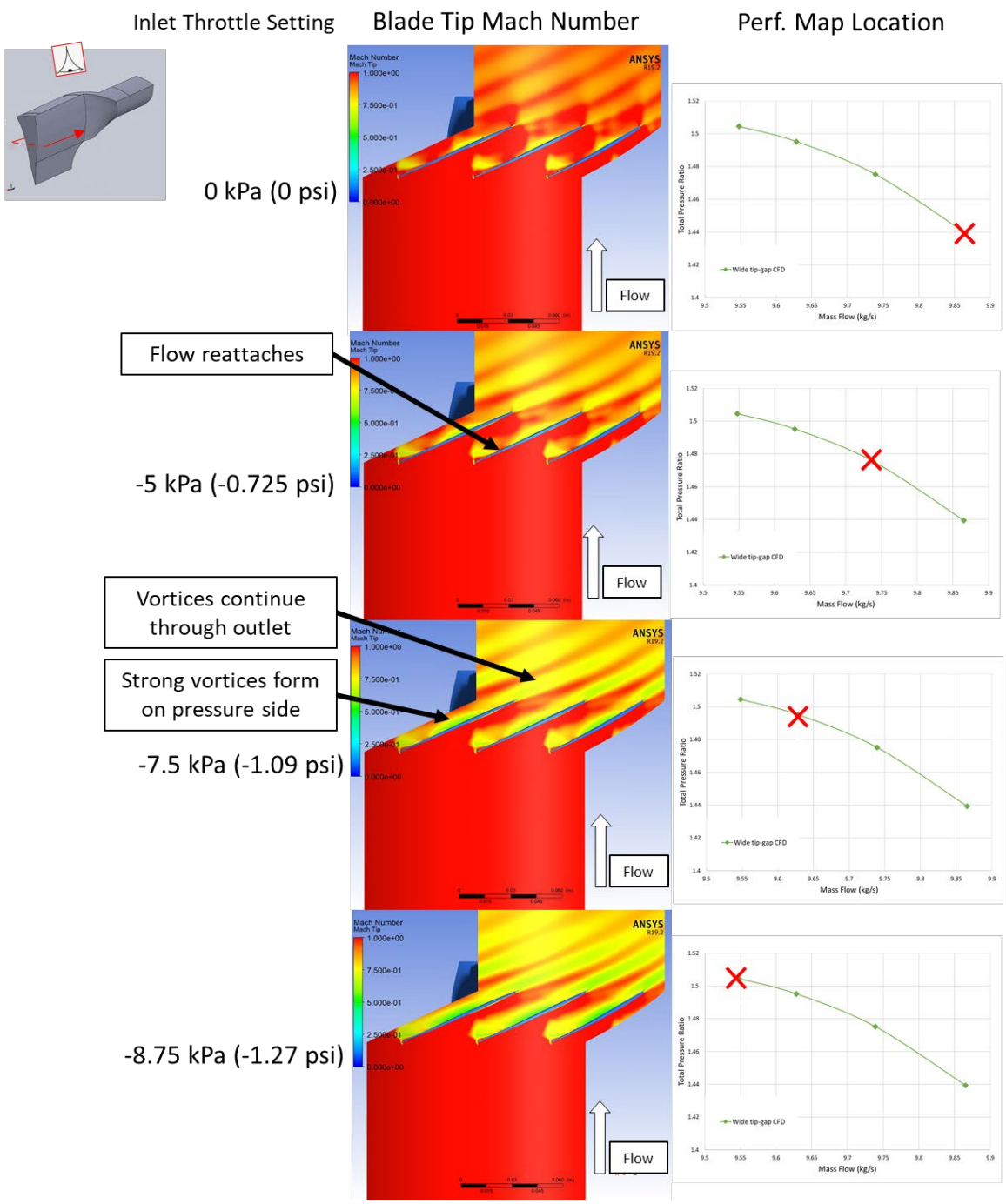

Figure 64. Mach number at 95% blade span progression for the wide tip-gap case.

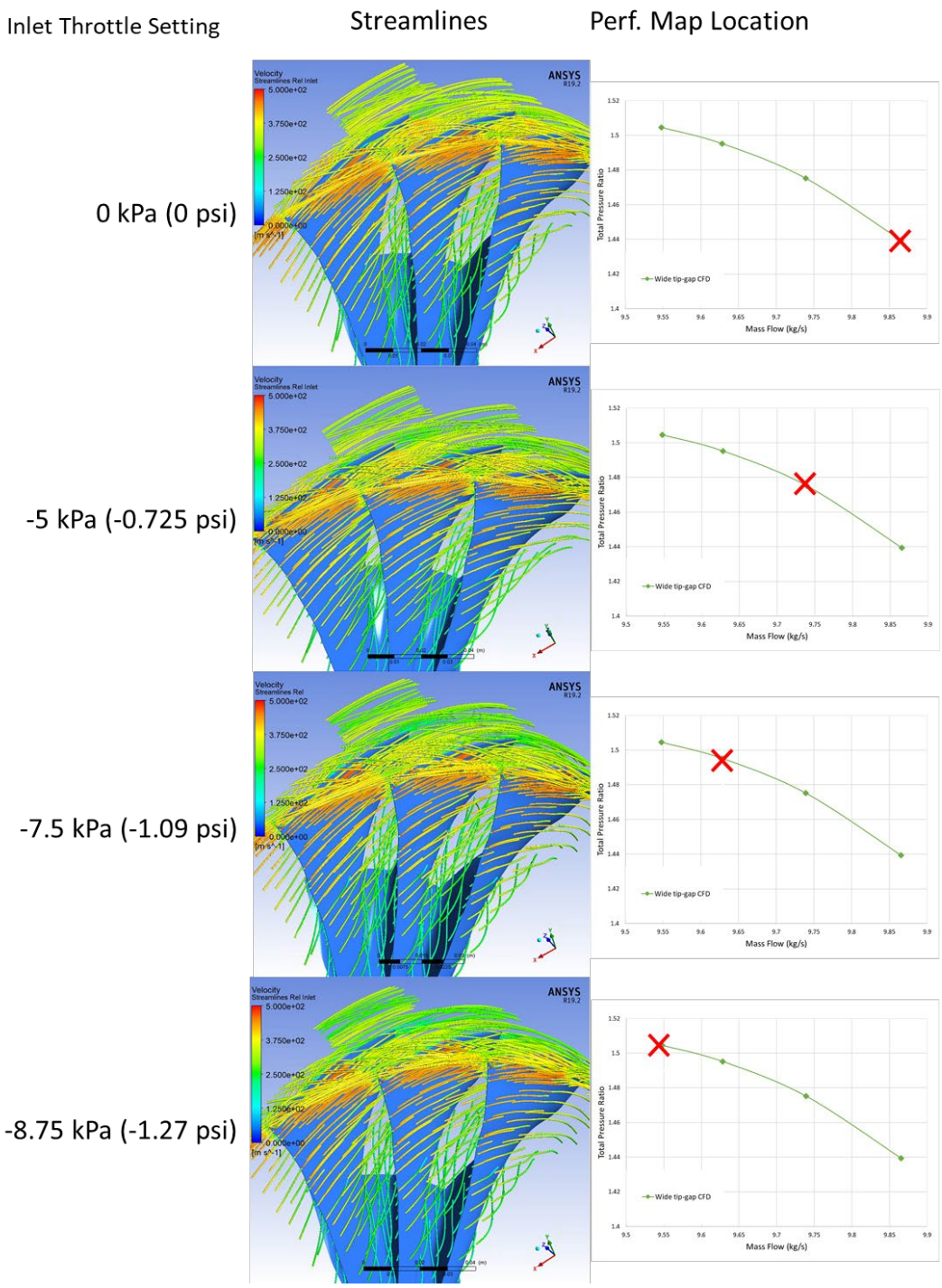

Figure 65. Streamline progression for the wide tip-gap case.

6. Tip-Gap Effects

As a means for illustrating the tip-gap effects identified in the previous sections, the present section provides a direct comparison of the pressure fields for the zero, narrow, and wide tip-gap cases at a 95% span surface as each case progresses towards stall. This comparison is provided in Figure 66. Each row compares the three tip-gap configurations at comparable points within each case's respective speed line. The differences in flow features identified primarily occur at the interface of the leading-edge tip vortex with the first standing normal shock in the blade passage. The flow field progression for the narrow tip-gap geometry shows that this vortex does not exist at first, then develops and strengthens as the flow progresses towards stall. Conversely, the zero and wide tip-gap flow fields show how the flow would appear in the absence of this vortex and how the flow would appear if the vortex strength was significantly increased, respectively.

Having observed the effects which the tip-gap vortices have on the flow, as pictured in Figure 66, the mechanism for stall in the NPSMF thus appears to be excessive growth of the tip vortices. A possible mechanism by which these vortices induce compressor stall is proposed in the following section.

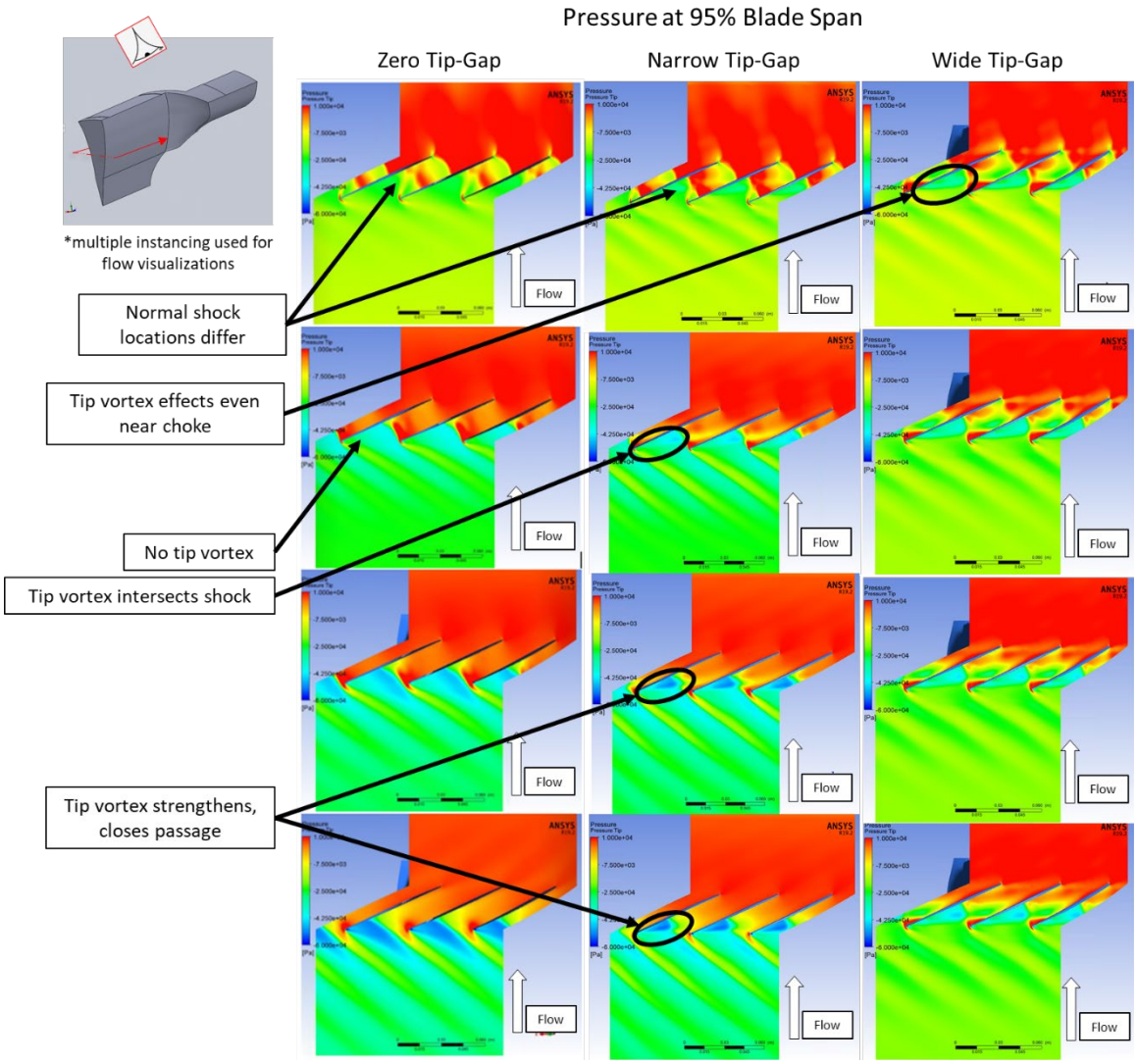

Figure 66. CFD case comparison to illustrate tip-gap effects on the NPSMF flow field.

7. Stall Mechanism Identification

Having identified the global importance of leading edge tip vortices to the flow field inside the NPSMF in the near-stall region, the present section introduces a possible mechanism by which these vortices induce stall. A step-by-step depiction of the proposed mechanism is provided in Figure 67.

The process depicted in Figure 67 shows that as the leading edge tip vortices grows to a critical strength, they begin to dominate flow near the tip of the blade, resulting in a

region of low pressure which gradually builds to occupy the entire width of the blade passage, at which point the fan is stalled. This low pressure region eventually begins to receive recirculated flow from the high-pressure flow closer to the hub. This recirculation process then becomes a positive feedback loop, whereby the recirculation region draws more flow from lower in the passage, and the fan settles into a state of deep stall.

At the onset of this process, the passage is still primarily open for flow, which results in the maximum performance point depicted in the first row of Figure 67. However, the growth of tip vortices gradually close the passage to flow, resulting in the gradual decay in performance until the tip vortices dominate and begin recirculation, at which point the performance and mass flow rate quickly drop off until the fan settles into the deep stall condition, where recirculation dominates.

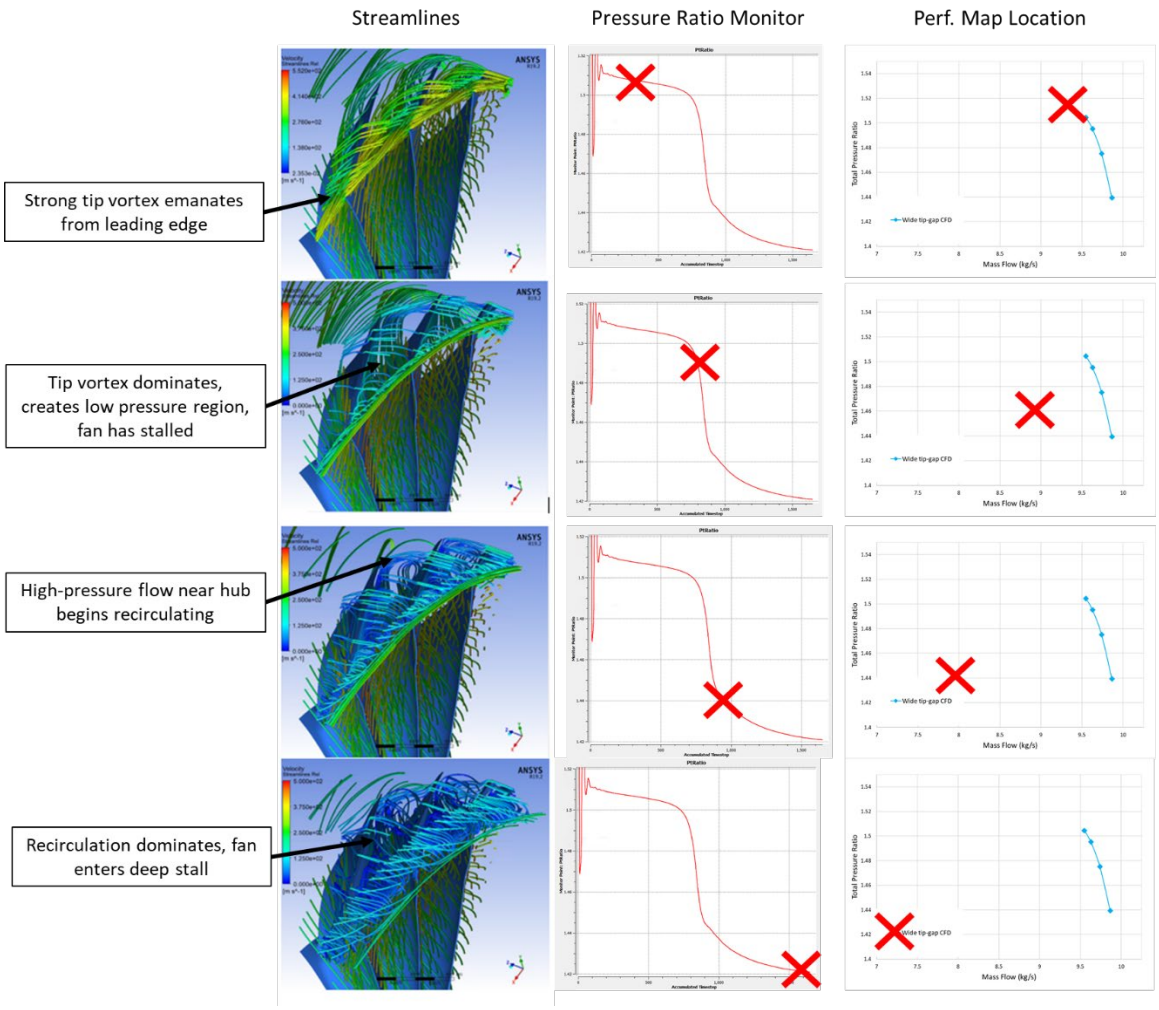

Figure 67. Streamline progression for a wide tip-gap stall case (streamline colors indicate velocity in the relative frame).

8. Limitations applied to the Present Study

This section qualifies the results presented in the preceding sections by accounting for several important limitations applied to the present study. Some of these limitations have been expounded elsewhere in this work, but are included again here for more thorough accounting and convenience to the reader.

The first and foremost limitation is that the analysis presented in this study was conducted using steady-state simulations of an inherently transient phenomenon. Thus, the mechanism proposed in the previous section is meant only as a first peek into the NPSMF flow field development during stall. Future work should examine flow through the NPSMF

in the near-stall region using transient simulations in order to either validate the results presented in this study or to uncover new flow phenomena which have yet to be observed in a CFD model of the NPSMF.

Similarly to the steady-state limitation, the present work conducted simulations of compressor stall inside the NPSMF using a single blade passage geometry with periodic boundaries, whereas compressor stall has consistently been observed to occur as an inherently multi-passage phenomenon. In particular, future work to model stall inside the NPSMF should consider simulations of multi-blade passages in order to observe the interactions between passages beyond that offered by a periodic boundary.

Thirdly, the turbulence model and laminar-to-turbulent transition model used during the present study would be well-suited to validation by conducting large eddy simulations of the NPSMF flow field near stall. As this study has shown, the effects of turbulence and turbulence transition are felt globally through the flow field in the near-stall region, especially considering the important roles which vortices and interactions between shocks and vortices play to the flow field development.

Finally, the present study has shown that the influence of tip-gap changes due to rotational and fluid loads should not be ignored in order to achieve the highest-possible fidelity model of flow through the NPSMF. While the un-deformed cold-shape geometry sufficiently modeled flow through the rotor at stable operating points, the exit profiles near stall presented in this study show that the effects of blade deformation cannot be ignored if the entire flow field is to be correctly modeled. Future work could begin by simulating the deformation caused by rotational loading in ANSYS or SolidWorks, save this “hot shape” geometry and build the fluid domain around it, and simulate it in similar fashion to this study. Additionally, the two-way FSI model proposed by Thornton [15] could be merged with the model proposed in this study.

THIS PAGE INTENTIONALLY LEFT BLANK

VII. CONCLUSIONS

This study improved upon previous CFD models of the NPS Military Fan with a particular focus on resolving flow through the rotor in the near stall region. Improvement was accomplished by rebuilding the fluid domain geometry used to represent the experimental rig inside of which the NPSMF is mounted, and by refining the mesh used to conduct simulations of flow through the rotor. The improved model was then used to simulate flow through the rotor along the 90% speed line, and compared to experimental data.

The reconstructed geometry was designed in SolidWorks and successfully implemented several desirable features, both for flow modeling and for integration with other NPSMF research projects. These features included:

- A conformal periodic boundary surface offset from the blade which constitutes a true periodic boundary;
- Matching high and low periodic boundary surface areas, which enabled a 1:1 mesh connection between the two surfaces;
- A framework for quickly implementing new casing treatments for CFD validation, and;
- A framework for generating multi-blade passage geometries to study the inter-passage phenomena which occur during stall.

A mesh sensitivity study was also conducted which resulted in a set of meshing guidelines for the NPSMF geometry that significantly improves on the quality of previous meshes. The mesh refinement process utilized face sizing settings, inflation settings, global mesh settings, and other ANSYS meshing features in order to achieve the following desired improvements:

- Uniformly wrapping inflation layers around the advanced-geometry blade surface;

- Inflating the casing inner surface without interfering with the blade tip inflation layers;
- Achieving a suitable blade average y^+ for gamma-theta laminar-to-turbulent boundary layer transition;
- Resolving shocks, expansion fans, and vortices, and the flow regions in which these features interact within the blade passage, and;
- Maintaining a reasonable computational cost.

The improved geometry and meshing process were then combined into an updated CFD model to simulate flow through the NPSMF. Flow simulations were conducted along the 90% speed line for the zero, narrow, and wide tip-gap cases. Simulations of the narrow and wide tip-gaps were chosen to represent flows using real casings used during experimental runs of the TCR. The zero tip-gap case was chosen as a tool for examining the effects incurred by the finite tip-gaps of the narrow and wide tip-gap casings. Due to the inherent inefficiency of flow using the wide tip-gap casing, only narrow tip-gap experimental data was used for comparison to the CFD simulations. The performance and flow fields for the narrow tip-gap case were then compared to available experimental data, and the zero and wide tip-gap cases were compared to the narrow tip-gap case. It was observed that in the near stall region, the effects of tip vortices shed from the blade leading edge dominate the flow field, which creates a strong link between their strength and an impending stall. These findings were then applied to propose a possible mechanism by which the NPSMF stalls, whereby the tip vortices shed from the leading edge lead to recirculation of flow through the blade passage.

The study concluded by recounting some important limitations which qualify the results, and recommended several modifications which would either validate or improve upon the results presented here. The recommended avenues for future work were:

- Conducting transient simulations in the near-stall region of the 90% speed line using the model presented in this study to identify transient flow phenomena not identified in this study;

- Conducting multi-passage simulations in the near-stall region of the 90% speed line to identify inter-passage flow phenomena near stall and during stall;
- Performing large eddy simulations for comparison to results obtained in this study using Shear Stress Transport and gamma-theta turbulence and boundary layer transition models, and;
- Implementing a fixed-geometry hot-shape rotor or re-implementing a fluid-structure interaction model to review the effects of blade deformation, especially around the tip in the near-stall region.

THIS PAGE INTENTIONALLY LEFT BLANK

APPENDIX: CFX-PRE REPORT FOR UPDATED CFD MODEL

CFX-Pre report for a narrow tip-gap geometry solver run.

Domain	Boundaries	
Default Domain	**Boundary - Inlet**	
	Type	INLET
	Location	Inlet
	Settings	
	Flow Direction	Normal to Boundary Condition
	Flow Regime	Subsonic
	Heat Transfer	Stationary Frame Total Temperature
	Stationary Frame Total Temperature	2.8815e+02 [K]
	Mass And Momentum	Stationary Frame Total Pressure
	Relative Pressure	RelPStagIn
	Turbulence	Medium Intensity and Eddy Viscosity Ratio
	Boundary - Rotor_Periodic Side 1	
	Type	INTERFACE
	Location	Periodic_high
	Settings	
	Heat Transfer	Conservative Interface Flux
	Mass And Momentum	Conservative Interface Flux
	Turbulence	Conservative Interface Flux
	Boundary - Rotor_Periodic Side 2	
	Type	INTERFACE
	Location	Periodic_Low
	Settings	
	Heat Transfer	Conservative Interface Flux
	Mass And Momentum	Conservative Interface Flux
	Turbulence	Conservative Interface Flux
	Boundary - Outlet	
	Type	OUTLET
	Location	Outlet
	Settings	
	Flow Regime	Subsonic
	Mass And Momentum	Average Static Pressure
	Pressure Profile Blend	1.0000e-01
	Relative Pressure	RelPBack
	Pressure Averaging	Average Over Whole Outlet
	Boundary - Blade	
	Type	WALL
	Location	Blade
	Settings	
	Heat Transfer	Adiabatic
	Mass And Momentum	No Slip Wall
	Wall Roughness	Smooth Wall
	Boundary - Blisk_minus_Blade	
	Type	WALL
	Location	Blisk_minus_Blade
	Settings	

	Heat Transfer	Adiabatic
	Mass And Momentum	No Slip Wall
	Wall Roughness	Smooth Wall
	Boundary - Default Domain Default	
	Type	WALL
	Location	F2536.2656, F2606.2656, F2607.2656, F2608.2656, F2609.2656
	Settings	
	Heat Transfer	Adiabatic
	Mass And Momentum	No Slip Wall
	Wall Roughness	Smooth Wall
	Boundary - InnerWall	
	Type	WALL
	Location	InnerWall
	Settings	
	Heat Transfer	Adiabatic
	Mass And Momentum	No Slip Wall
	Wall Velocity	Counter Rotating Wall
	Wall Roughness	Smooth Wall
	Boundary - OuterWall	
	Type	WALL
	Location	OuterWall
	Settings	
	Heat Transfer	Adiabatic
	Mass And Momentum	No Slip Wall
	Wall Velocity	Counter Rotating Wall
	Wall Roughness	Smooth Wall

LIST OF REFERENCES

[1] R. Moore and L. Reid, "Performance of Single-Stage Axial-Flow Transonic Compressor with Rotor and Stator Aspect Ratios of 1.19 and 1.26, Respectively, and With Design Pressure Ratio of 1.82," NASA Lewis Research Center, Cleveland, OH, 1982.

[2] W. Hofmann and J. Ballmann, "Tip clearance vortex development and shock-vortex-interaction in a transonic axial compressor rotor," *40th AIAA Aerosp. Sci. Meet. Exhib.* 2002.

[3] C. Hah, D. C. Rabe, and A. R. Wadia, "Role of tip-leakage vortices and passage shock in stall inception in a swept transonic compressor rotor," *Proc. ASME Turbo Expo 2004*, vol. 5 A, pp. 545–555, 2004.

[4] M. G. Turner, A. Nemnem, A. J. Gannon, G. V. Hobson, and W. Sanz, "Measured heat transfer in a transonic fan rig at casing with implications on performance," *Proc. ASME Turbo Expo,* vol. 2A, 2015.

[5] A. A. Ameri, "NASA Rotor 37 CFD Code validation," *47th AIAA Aerosp. Sci. Meet.* 2009.

[6] R. Kelly, A. Hickman, K. Shi, S. C. Morris, and A. Jemcov, "Very large eddy simulation of a transonic axial compressor stage," *52nd AIAA/SAE/ASEE Joint Propulsion Conf*. 2016.

[7] P. Nel, "Computational Fluid Dynamics-Modelling of a Multi-Stage Transonic Axial-Flow Compressor," M.S. Thesis, Department of Mechanical and Mechatronic Engineering, University of Stellenbosch, Matieland, South Africa. 2019.

[8] H. Kuang, S. W. Chu, H. Zhang, and S. Ma, "Flow mechanism for stall margin improvement via axial slot casing treatment on a transonic axial compressor," *J. Appl. Fluid Mech.,* vol. 10, no. 2, pp. 703–712. 2017.

[9] A. F. Mustaffa and V. Kanjirakkad, "Single and Multiple Circumferential Casing Groove for Stall Margin Improvement in a Transonic Axial Compressor," *Journal of Turbomachinery*, vol. 143, no. 7, pp. 1–8. 2021.

[10] G. Zhu and B. Yang, "Optimization of Slots-Groove Coupled Casing Treatment for an Axial Transonic Compressor," *Journal of Turbomachinery*, vol. 142, no. 8, pp. 1–10. 2020.

[11] D. J. McNab, “Experimental Testing and CFD Modeling of an Advanced Transonic Compressor for Military Applications,” M.S. Thesis, Department of Mechanical and Aerospace Engineering, Naval Postgraduate School, Monterey, CA, 2011.

[12] E. V. DeSousa, “Development of Advanced Casing Treatments for Transonic Compressors,” M.S. Thesis, Department of Mechanical and Aerospace Engineering, Naval Postgraduate School, Monterey, CA, 2018.

[13] A. Londono, “Near-stall modal disturbances within a transonic compressor rotor,” M.S. Thesis, Department of Mechanical and Aerospace Engineering, Naval Postgraduate School, Monterey, CA, 2011.

[14] G. Descovich, “Experimental and Computational Investigation of Steam-Induced Stall in a Transonic Compressor Rotor for a Military Fan,” M.S. Thesis, Department of Mechanical and Aerospace Engineering, Naval Postgraduate School, Monterey, CA, 2011.

[15] G. Thornton, “Fluid-Structure Analysis of a Transonic Rotor,” M.S. Thesis, Department of Mechanical and Aerospace Engineering, Naval Postgraduate School, Monterey, CA, 2019.

[16] J. D. Denton, “Lessons from rotor 37,” *J. Therm. Sci.*, vol. 6, pp. 1–13, 1997.

INITIAL DISTRIBUTION LIST

1. Defense Technical Information Center
   Ft. Belvoir, Virginia

2. Dudley Knox Library
   Naval Postgraduate School
   Monterey, California